Unraveling the Reconfiguration Dynamics of Silver Nanowire Networks under Electrothermal Stress

by

Adam Morris Willner Trebach

Submitted to the Department of Physics
in partial fulfillment of the requirements for the degree of
Doctor of Philosophy in Physics
at the
MASSACHUSETTS INSTITUTE OF TECHNOLOGY
February 2024

Author .....
Department of Physics
January 15, 2024

Certified by .....
Jeffrey C. Grossman
Morton and Claire Goulder and Family Professor in Environmental Systems
Thesis Supervisor

Certified by .....
Joseph Checkelsky
Mitsui Career Development Associate Professor of Physics
Thesis Co-Supervisor

Accepted by .....
Lindley Winslow
Associate Department Head of Physics

Unraveling the Reconfiguration Dynamics of Silver Nanowire Networks under Electrothermal Stress

by

Adam Morris Willner Trebach

Submitted to the Department of Physics
on January 15, 2024, in partial fulfillment of the
requirements for the degree of
Doctor of Philosophy in Physics

Abstract

Transparent conducting electrodes (TCEs) are vital to many optoelectronic devices including solar panels and touch-screens. Indium Tin Oxide, the dominant TCE, comes with myriad problems including a shaky supply chain and brittleness. Networks of silver nanowires show many advantages over ITO, but they suffer from problems with durability. In this work, we focus on electrothermal instability and provide new insights into the electrothermal drivers of silver nanowire network failure. First, we borrow the notion of betweenness centrality from graph theory and test its applicability to simulated nanowire network systems. We also test several other centrality measures, some introduced here and designed specifically to describe nanowire networks. We find that betweenness centrality performs as well as or better than the other tested measures in terms of ability to identify network elements least important to conduction. We then execute a combined computational and experimental analysis of several small, computationally tractable silver nanowire networks. We create high fidelity computational models of these specific systems and calculate electrical and graph theoretic properties to test whether we can predict failure. We find that standard circuit analysis outperforms graph theoretic measures, although neither prove predictive. We find strong evidence that electromigration is the primary driver of failure at contacts between silver nanowires, either by causing failure directly or by providing the kinetic perturbations required to initiate spheroidization. In the process of building our computational models of real nanowire networks, we develop several new image processing techniques that show great promise when applied to the challenging task of automatically extracting non-planar graphs from images.

Thesis Supervisor: Jeffrey C. Grossman
Title: Morton and Claire Goulder and Family Professor in Environmental Systems

Thesis Co-Supervisor: Joseph Checkelsky
Title: Mitsui Career Development Associate Professor of Physics

Acknowledgments

This thesis would not have been possible without the support from an army of mentors, collaborators, friends, and family. First and foremost, I am surpassingly grateful for the guidance of my research advisor Professor Jeffrey C. Grossman. Getting a PhD is a hard thing during the best of times, and the interval from 2017-2023 has certainly not been the best of times. Through a veritable parade of unexpected challenges, Jeff has offered his unwavering support. He has given me time when I needed to take care of myself or my family, and he has encouraged me whenever I doubted the value of our work. He is a brilliant scientist of boundless and infectious optimism. I always leave our meetings reinvigorated, usually with several new ideas in tow. Thank you, Jeff, for opening your lab to this recovering astrophysicist.

I also wish to thank the members of my thesis committee. Professor Joe Checkelsky has served as both my academic advisor and my research co-supervisor within the physics department. I'm deeply grateful for his help navigating the requirements of a physics PhD while my research straddles several disciplines. Professor Riccardo Comin always asks interesting questions about my work and I have found our conversations to be great fun. I am especially thankful to Professor Isaac Chuang whose general knowledge of computation and materials has proven invaluable time and again and whose hard questioning has made my research considerably stronger.

Among my academic mentors, few loom as large as Professor Jim Buckley, my undergraduate research advisor at Washington University in St. Louis. Jim gave me my first taste of the life of a scientist and working with him was a true delight. His belief that I could succeed buoyed my spirits as I applied to graduate school after four years in the private sector.

Max Elias, one of my first science teachers, cultivated a love of discovery in all of his students, myself included. Bill George, my high school evolutionary biology teacher, taught me that the work scientists do is not insulated from politics. The salience of this lesson has only increased in recent years. Rhona Gordon, more than anyone else, taught me to use my strengths to compensate for my weaknesses. If I

have written prose that is intelligible, I owe it to her influence. Finally, I'm grateful to Professor Thomas Bernatowicz from Washington University in St. Louis, who first made me fall in love with physics.

I have collaborated with many scientists during my time at MIT. I want to send special thanks to Dr. Thomas Sannicolo and Dr. Jatin Patil. Thomas guided me through the process of writing my first paper and his wisdom on project design still serves me today. Jatin, quite simply, has made the experimental part of my work possible. There would be no experiments without him. I'm also grateful to Dr. Gabriel Loewinger for his help with various statistical methods. Thanks as well to Dr. Nicola Ferralis, for working with me to find new applications for the techniques I will discuss in this thesis. I am also grateful to the many other graduate students and post docs with whom I have worked during my PhD, especially to Dr. Yun Liu, Dr. Taishan Zhu, Dr. David Chae, Dr. Asmita Jana, Dr. Ki-Jana Carter, Evan Toth, Dr. Dillon Yost, Dr. Abishek Agarwal, and Dr. Shuo Wang.

I'm deeply grateful to all my friends in the MITGSU for your support and camaraderie. It has been an honor to struggle alongside you to make MIT a better place for all who work here. I also want to thank the many administrators who make succeeding at MIT possible including Cathy Modica, Shannon Larkin, Laura von Bosau, and Sydney Miller. All of these special people have helped me navigate logistical nightmares on at least one occasion, and Cathy and Sydney have supported me through challenging personal issues as well. Sydney, in particular, has become a dear friend and confidant and I am profoundly thankful for her wisdom and her company.

My girlfriend, Adrienne Dunlap, has been vital to my success both through her constant support and by making sure I perform important tasks like eating and sleeping. She never complained even as I temporarily vanished from our shared life to complete my thesis. I don't know what I would have done do without her. I'm incredibly thankful as well to our canine companion, Lulu, whose perfect indifference to the demands of my work has paradoxically soothed me through this incredibly stressful time. She is a creature of pure self-interest and I could not love her more.

I would be remiss if I did not also mention my childhood nanny and second mother Carmen Guevara. Carmen taught me spanish and arithmetic long before I entered school, giving me a head start on skills that have served me profoundly well in my career and in my life.

Finally, I am forever indebted to my mother, Marjorie Alison Rosner, and my late father, Professor Arnold Shepard Trebach. My mother taught me to be kind. She told me that I could do anything I wanted in my life - there was no way I could disappoint her as long as I wasn't hurting anybody. She told me that other people should have this freedom too. It is a simple moral lesson, but one that shapes my thinking still. My father taught me the value of luck. He was born a year before the beginning of the Great Depression to a poor family in Lowell, Massachusetts. He worked his way through high school, community college, law school, and then his PhD at Princeton. There are many who, given this background, would believe that they had pulled themselves up by their own bootstraps. My father would have none of it. He was proud that he worked hard, make no mistake, but he was also profoundly grateful for the tremendous luck he had along the way. He felt himself lucky to have avoided the draft, lucky to have been able to go to college at all, lucky to get the chance for an academic job, lucky to be noticed and invited to serve on the commission for civil rights, lucky to have met my mother, and lucky to have his three wonderful children.

I pride myself on the time and hard work that I put into this thesis, but I am keenly aware of the role of luck in this success. I have been lucky to have clean food and water, lucky to have a head for numbers, lucky to receive a fabulous education, lucky to have parents with the resources to get me essentially anything I might need. Much of this luck boils down to choices my parents made and/or the good fortune that was bestowed upon them. Perhaps the greatest luck, though, is the benign influence of their two souls on mine. Grit, empathy, good humor - all these things I learned from my folks. In my eyes, this work belongs to the three of us, so I dedicate it to them.

For my parents, who have given me everything

Contents

List of Figures

List of Tables

Chapter 1

Introduction to Transparent Conducting Electrodes

1.1 The Current TCE Landscape

As the name suggests, Transparent Conducting Electrodes (TCEs) are a class of materials that transmit both light and electrical current with little impedance. Although they are relatively little known, TCEs are ubiquitous. The best known use of TCEs is likely in the capacitive touch screens on modern phones and tablets [49], but TCEs are also used in transparent film heaters [86] which are found on airplane windshields, electromagnetic shielding [98], and in organic electronics [18] such as OLED displays or organic photovoltaics. The optimal mix of properties for a TCE depends on the application as shown in Figure 1.1.

Figure of merit (FOM), chemical stability, thermal stability, and flexibility are assets in all cases but there are some cases in which they are not necessary. Displays, for example, tend to be used indoors and are sheltered from the elements, so chemical stability is comparatively less important than it is for solar panels which must endure rain and temperature fluctuations. Low optical haze, defined as the ratio of scattered transmission to total transmission, is unlike the other attributes in Figure 1.1 because there are some applications in which low optical haze can actually hamper

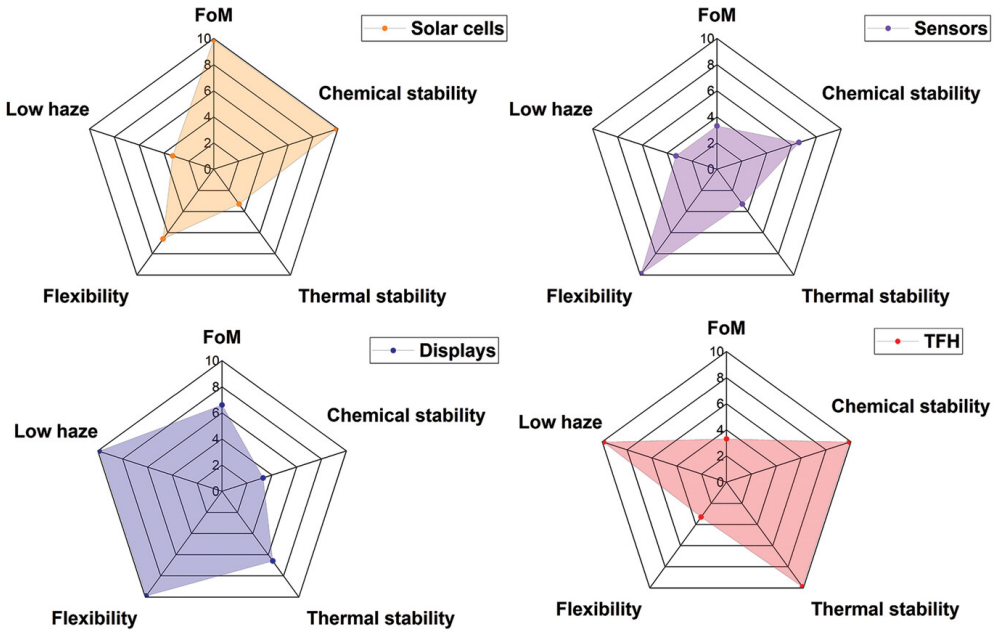

Figure 1.1: Radar plot showing the relative importance of performance metrics for Transparent Film Heaters (TFH), solar cells, displays, and sensors. Marks are only general qualitative indications, where a higher score indicates greater importance of the given attribute. FoM denotes that transparent electrode figure of merit. Taken from [88]

device performance. In solar panels, a high degree of haze can increase path length through the photovoltaic material and thereby enhance photon absorption probability.

The transparent conductor figure of merit (FoM) in Figure 1.1 merits special discussion. A figure of merit for TCEs is an attempt to capture in a single scalar quantity the ability of the material to both transmit light and conduct electricity. A common choice for this quantity is the ratio of DC conductivity to optical conductivity [106] shown in Equation

$$\text{FoM} = \frac{\sigma_{\text{DC}}}{\sigma_{\text{optical}}} = \frac{Z_0}{2R_{\text{sh}}\left(\frac{1}{\sqrt{T}} - 1\right)} \tag{1.1}$$

where $Z_0 = 377\,\Omega$ is the impedance of free space, R_{sh} is the material sheet resistance in units of $\Omega/\square$, and T is the material transmission coefficient (transparency) which ranges from 0 to 1. This figure of merit has several nice properties: first, the value

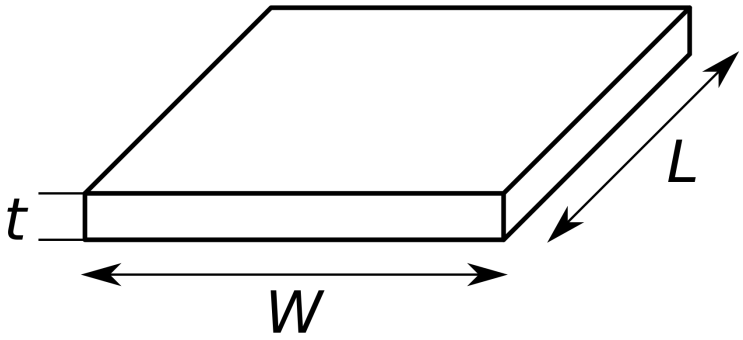

Figure 1.2: Diagram of conductive slab geometry. Taken from [4]

approaches zero as either R_{sh} or T approach zero; this is sensible because, for a transparent conductor, there is no amount of electrical conductivity that can compensate for zero optical transmission (and vice versa). In addition, the FoM approaches infinity as $R_{\text{sh}} \to 0$ (infinite conductivity) or as $T \to 1$ (complete transparency). Getting R_{sh} near 0 and T near 1, however, is often challenging because of the mutually parasitic relationship that exists between conductivity and transparency in most TCEs.

To understand this, consider the slab of material shown in Figure 1.2. If the material has electrical resistivity ρ, the sheet resistance can be expressed as

$$R_{\text{sh}} = \frac{\rho}{t} \tag{1.2}$$

Therefore increasing the thickness t will decrease the sheet resistance. But increasing the thickness will also decrease the transparency as $T \propto \exp(-t/\tau)$ for optical depth τ (note that, in general, τ may depend on wavelength as well as material).

Currently, the industry standard material that manages to achieve a high degree of both transparency and conductivity is Indium Tin Oxide, also known as ITO [87]. ITO is a semiconductor with a high carrier concentration of 10^{20}–$10^{21}\,\text{cm}^{-3}$ and a

wide bandgap of 3.5–4.3 eV that, respectively, give the material a low sheet resistance of approximately 20 Ω/□ and a high transparency of approximately 85 % average visible transmittance [63]. ITO is also resistanct to moisture and bonds strongly to glass. This cocktail of characteristics explains ITO's commercial preeminence in applications requiring a TCE.

One of the great drawbacks of ITO is that it comprises roughly 75 % indium by mass [3], and indium faces some challenging economics. Indium is almost exclusively found in the zinc-rich mineral sphalerite which is typically less than 0.1 % indium by mass [103]. This means that indium is generally only found in significant quantities in the byproducts of other industrial processes which, in turn, means that indium production cannot respond elastically to changes in demand. We can see the effects of this in indium prices: from 1999-2020 the cost of 1 kg of indium increased by 28 % even though indium production quadrupled during the same period [112, 113]. Indium is considered critical to renewable energy by the United States Geological Survey [14] owing to its use in copper-indium-gallium-diselenide thin film solar cells. Furthermore, the geographical distribution of indium deposits renders them vulnerable to supply disruptions [114].

The obstacles to a reliable indium supply are not the only problem with our dependence on ITO as a TCE. The manufacture of Indium Tin Oxide at industrial scale relies on complex and often costly techniques such as E-beam evaporation, pulsed laser deposition, spray pyrolisis, radio frequency magnetron sputtering, or most commonly direct current magnetron sputtering [118]. These processes require high temperatures, specialized equipment such as lasers of high vacuum chambers, or sometimes a combination thereof. The resulting ITO films are also brittle which limits their use in flexible electronics [87]. In addition, ITO has very poor infrared transparency [12, 21] which limits its use as a TCE in photovoltaics because a majority of solar radiation incident on the earth's surface comprises IR photons [115].

In summary, there is a great need for alternative transparent electrodes for two primary reasons. First, we are not well positioned to reliably satisfy current demand for indium, to say nothing of future demand. As most indium is used in the production of ITO, alternative TCEs can obviate many of our present indium supply problems by replacing ITO in some applications (e.g. charge collection in thin film organic photovoltaics) and in so doing increase the availability of indium for those applications in which is truly irreplaceable. Second, ITO is not suitable for all applications that call for TCEs. Developing alternative transparent conducting materials will enhance the ability to manufacture important devices such as flexible electronics and solar cells.

1.2 Silver Nanowire Networks as TCEs

Networks of interconnected silver nanowires have the potential to serve as one of these replacement TCEs and, due to these networks' mechanical flexibility, they can also be used in ways that ITO cannot. The components of these materials, silver nanowires, earn their name from their minuscule size: typical diameters range from 10–100 nm and typical lengths range from 10–100 µm. They are shaped much like human hairs with diameter and length scaled down by a factor of 1000. This characteristic size renders these wires quite invisible to the naked eye, both because our eyes cannot resolve details this small and because silver wires are almost entirely optically transparent when they are this thin. These silver wires, much like bulk silver, are also excellent conductors of electricity.

Fabricating a functional TCE made of silver requires synthesizing the nanowires themselves and depositing them onto some suitable substrate, often glass or PEDOT:PSS. At the this point in fabrication, the electrical contacts between different nanowires are usually of poor quality due to a combination of an insulating PVP layer on the nanowire surfaces left over from synthesis [33], extremely small contact areas

between wires, and boundaries between crystal planes. To ameliorate these problems and give the network a low enough sheet resistance to be useful, it is essentially required to perform some form of junction optimization.

One such method is electroplating the network with gold, which has been shown to decrease junction resistance from 1 GΩ to 450 Ω [52]. Studies examining the effects of network optimization on individual junctions are unfortunately rare due to the difficulty of taking single junction measurements. Instead, it is much more common to report the improvement in the entire network's sheet resistance. Thermal annealing is likely the most common technique to remove the PVP coating and optimize the nanowire junctions but this is unacceptable in applications requiring mechanical flexibility because the high temperatures required destroy the flexible polymer substrate to which the nanowires are attached [41]. Methods that preserve the flexible nanowire substrate include chemical welding [58], solvent evaporation [131], laser nano-welding [73], encapsulation with other materials such as graphene oxide [19, 101], mechanical pressing [41], plasmonic welding [41], and electrically induced welding [105].

In spite of the interconnectedness among transparency, conductivity, and haze, there are some ways to circumvent inherent tradeoffs and improve the FOM. It has been shown computationally that, by preferentially aligning nanowires in a given direction, it is possible to increase conductivity along the axis of alignment at the cost of a greater decrease in conductivity perpendicular to the direction of alignment [54]. At a fixed areal mass density, networks of longer wires have lower resistances than networks of shorter wires [110]. Bi-disperse networks with 90% shorter wires and 10% longer wires show a near order of magnitude reduction in resistance compared to networks at the same areal density with 100% shorter wires [84]. Networks of longer nanowires also have higher transparency than networks of shorter wires at all visible wavelengths [72]. Conductivity has been found to scale linearly with nanowire length and the figure of merit scales approximately linearly with the nanowire aspect ratio [110]. Thus the nanowire dimensions are vitally important to device perfor-

mance. While it would be ideal to modify synthesis such that longer nanowires are produced, achieving this is not trivial. Changes to synthesis tend to increase/decrease both nanowire length and diameter at the same time [130], and increased nanowire diameter leads to decreased transparency and increased haze. That said, there has been considerable success growing very long nanowires with fixed diameters using a multi-stage synthesis process [72].

Typical sheet resistances for silver nanowire networks range from 10s-100s of $\Omega/\square$ and transparencies range from 80–95 % yielding a figure of merit that ranges from roughly 16–725. As shown in Figure 1.3, this optoelectronic performance matches that of ITO and exceeds that of many other TCEs in terms of sheet resistance. Furthermore, silver nanowire networks are mechanically flexible and solution processible [87], all significant advantages over ITO. As an added bonus, silver nanowire networks have very small mass loading compared to ITO making their costs (in absolute terms) less sensitive to price fluctations in raw materials. As a result of these desirable properties, silver nanowire based materials have been integrated into organic solar cells [109, 85], transparent film heaters [55, 48], flexible health sensors attached to the skin [127, 122], transparent shielding from electromagnetic interference [95], high performance supercapacitors [74], and myriad components relevant to photonics and quantum information [128].

1.3 Instabilities in Silver Nanowire Network TCEs

The list of successes in the preceeding discussion would lead any red-blooded nanowire enthusiast to wonder: if silver nanowire meshes are so great, why have they not completely displaced ITO in the market for TCEs? The answer is stability: meshes of silver nanowires, although robust enough for some applications, generally do not last as long as ITO. The failure mechanisms of silver nanowire generally fall into four categories: mechanical effects, chemical effects, electrical effects, and thermal effects,

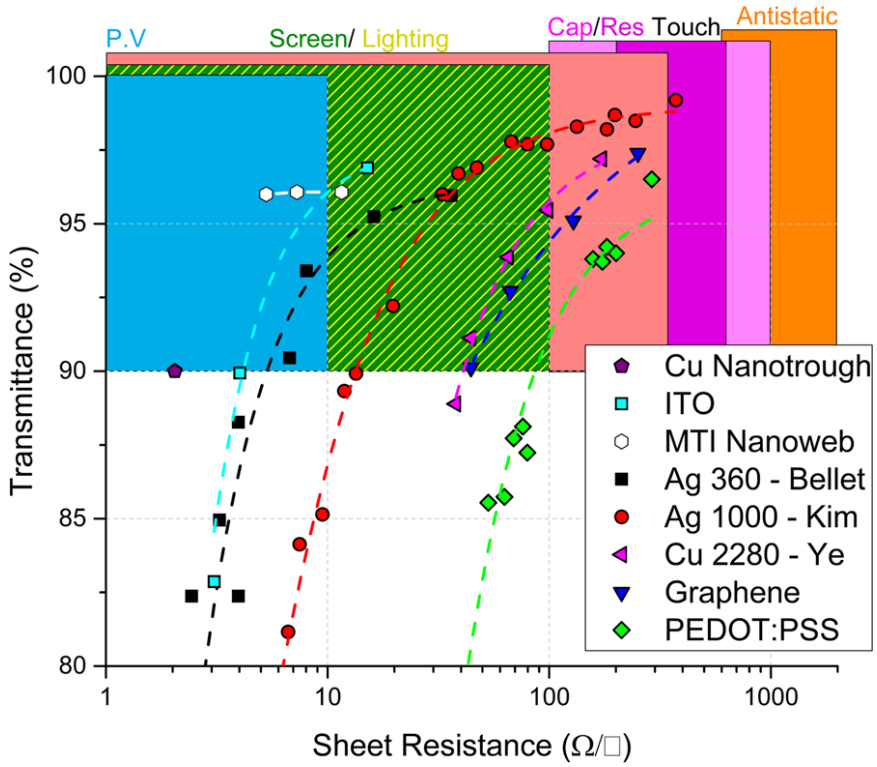

Figure 1.3: Shaded regions show transmittance and sheet resistance requirements for various flexible TCE applications including photovoltaic (PV), screen and lighting, capacitive and resistive touch screens and antistatic coatings. Points and lines compare the best performing TCE technologies currently available. Data sources are: Cu Nanotrough and ITO [47], MTI Nanoweb [8], Ag nanowires (NWs) with an aspect ratio (AR) of 360 [9], 1000 [64], Cu NWs with an AR of 2280 [129], PEDOT:PSS TCE [30], calculated and experimental graphene TCEs [64, 83]. Figure taken from [81].

although there can be significant interplay between any of these.

Mechanical failures typically occur as a result of flexion. Althought the nanowires have random orientations, and therefore strains are scaled by a factor of $\cos\theta$ where θ is the angle between the nanowire axis and the strain direction, it is still quite possible for nanowires to undergo brittle failure [87]. In general, networks deposited on thicker substrates will break more easily from flexion than will networks on thinner substrates because the strain is equal to $t/2R_c$ where t is the substrate thickness and R_c is the radius of curvature [87]. Chemical failure of silver nanowire networks arises most commonly from the degradation of silver into Ag_2S as a result of contact with atmospheric sulfur [87]. Ag_2S, also known as acanthite, forms nanoparticles on the surface of silver nanowires thus consuming silver and eventually severing connections between different segments of the same nanowire. There is evidence that this process takes about 6 months [29], but the precise rate is dependent on temperature, humidity, and initial defect concentration in the nanowires themselves [88]. In addition, Ag has poor stability in acidic conditions, a particular problem given that PEDOT:PSS, a transparent conductive polymer and one of the more common choices of susbtrate for silver nanowire networks, is acidic [87]. These chemical instabilities are exacerbated by the high surface area to volume ratio of nanowires: these systems offer a large area for hostile chemistry with little internal material in reserve to preserve the desirable properties of the wire. The high surface area to volume ratio of silver nanowires, in fact, plays an important role electrical and thermal failures as well and it is to these electrothermal failure dynamics that we now restrict our attention. This choice is motivated by the fact that every application of silver nanowires as TCEs involves carrying current and therefore every application of silver nanowires as TCEs will also involve some degree of joule heating. We begin with a discussion of electrothermal failure mechanics at small scales and then move to a discussion of larger scales.

The primary means of microscale electrical failure in silver nanowires is electromigration [89], which is shown schematically in Figure 1.4. When current is flowing

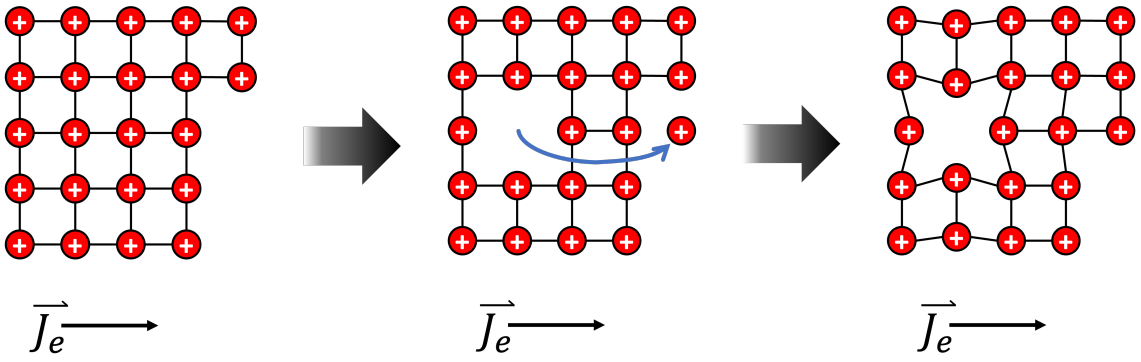

Figure 1.4: Schematic representation of electromigration of positive ions in a crystal due to momentum transfer from the rightward moving electrons (represented by the current density vector $\vec{\mathbf{J}}_e$). Note that $\vec{\mathbf{J}}_e$ points in the direction of electron flow rather than the direction of conventional current. Figure adapted from [2].

through a conductor, some momentum is transferred from the traveling electrons to the ions in the crystal lattice. In most circumstances, this momentum transfer is insufficient to permanently dislocate the positively charged ions from their site in the crystal lattice, instead simply leading to phononic oscillations (known at the macro scale as joule heating). However, at sites where the ionic diffusivity is greater, such as grain boundaries or surfaces, the momentum transfer can induce ions to dislocate permanently and occupy a new site in the lattice. This is represented by the second frame of Figure 1.4. This dislocation leaves a void in the original lattice thus causing a volume relaxation (tensile strain), as shown in the third frame of Figure 1.4. Although it is not shown in the figure, the ion's presence at its new site can also cause a compressive strain. As these strains accumulate, the nanowire can disconnect completely. As mentioned before, the importance of electromigration in silver nanowire based systems is largely a result of high surface area to volume ratios which lead to a far greater proportion of lattice sites with high ionic diffusivities. Further, silver nanowires are not truly cylinders but instead a collection of five wedges joined at five twin boundaries (known as a pentatwinned structure), shown in Figure 1.5. While twin boundaries do not show the same high atomic diffusivities as true grain boundaries, they nonetheless enhance the mobility of silver ions in the lattice [87] and thereby enhance their susceptibility to electrimigration induced failure.

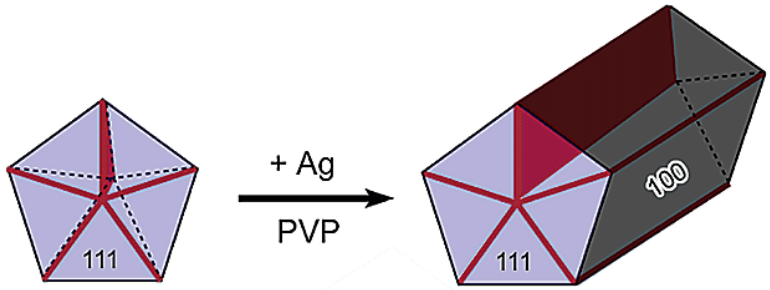

Figure 1.5: Diagram of the penta-twinned structure of silver nanowires synthesized in the polyol process. Numbers represent crystal facet miller indices. Red lines are the twin boundaries, coated with PVP, between silver wedges. Image taken from [111].

The second significant microscale failure mechanism of silver nanowire networks under electrothermal stress is spheroidization [87], a morphological evolution in which a cylinder-like object transitions into a set of disconnected spheres separated by a characteristic wavelength as shown in Figure 1.6. This transition results from the nanowire's minimization of surface energy - a set of spheres of radius R_0 have a lower surface area to volume ratio than a cylinder of length L and radius R_0 as long as $L > \frac{9}{2}R_0$. This transition, however, does not initiate without some perturbation that is usually provided by elevated temperatures. It is worth noting that this failure mechanism tends to occur at temperatures from 250–350 °C, considerably lower than the melting point of silver even after accounting for melting point depression resulting from the Gibbs-Thomson effect [87]. A given perturbation of size ε grows as

$$\frac{\partial \varepsilon}{\partial t} = \frac{\gamma \Omega^2 D c_s}{k_B T} \left(\frac{\partial^2 \kappa}{\partial S^2} \right) \tag{1.3}$$

where t is time, γ is surface energy, Ω is atomic volume, D is surface diffusivity, c_s is concentration of surface sites, k_B is the Boltzmann constant, T is temperature, and κ is curvature as a function of position S along the wire [66].

It is worth noting two common themes in electrical and thermal (also known as electrothermal) mechanisms. First, the high surface area to volume ratio of silver nanowires magnifies the importance of certain effects that would be negligible in a bulk material. Second, the electrical stress that is essentially inherent in use as a

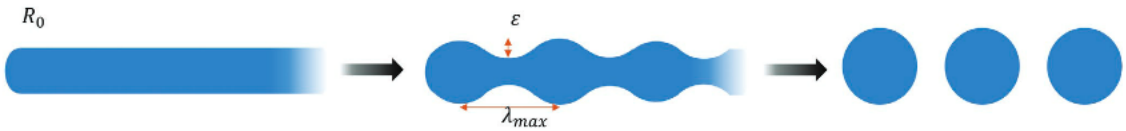

Figure 1.6: Depiction of spheroidization of a nanowire approximated here as a cylinder. Perturbation size is denoted by ε and characteristic wavelength denoted by $\lambda_{max} = 2\sqrt{2}\pi R_0$ where R_0 is the radius of the cylinder. Image taken from [87].

TCE can drive a feedback loop that turns local failures into global ones [102, 67]. When nanowire or junction fails, current gets redirected to adjacent components possibly causing them to fail as well. This can cause a crack to propagate cross the network roughly perpendicular to the direction of current flow that eventually entirely deletes electrical conductivity. An example of this process is shown in Figure 1.7 which depicts the time evolution of a nanowire network subjected to a voltage ramp of 0.5 V/min [102]. Note that in the diagrams, current flows on the left/right axis. Subfigure A0 shows the evolution of resistance with time during the voltage ramp. The Subfigures labeled A1-A5 are IR images of the network showing local temperature. Subfigures A1-A3 show the localization of a hotspot along the central axis of the network. Subfigure A4 shows the seeds of a crack forming at the bottom of the sample. Subfigure A5 shows how the crack has advanced perpendicular to current flow. The crack region in A5 is especially dark because, with no current flowing through it, the crack has cooled down considerably. 1.7. The dynamics of this system can change significantly depending on whether it is subjected to a constant voltage or a constant current: a current ramp for example would funnel increasing current through a constricted area thus creating considerably higher current density in the intact region of the network. We should therefore expect current ramps to damage a network more quickly than voltage ramps.

In summary, we have a relatively detailed understanding of silver nanowire network failure dynamics both at the scale of individual wires and at the scale of devices. But we have a much less developed understanding of the failure dynamics of nanowire networks at the scale where the interactions among wires are important but the indi-

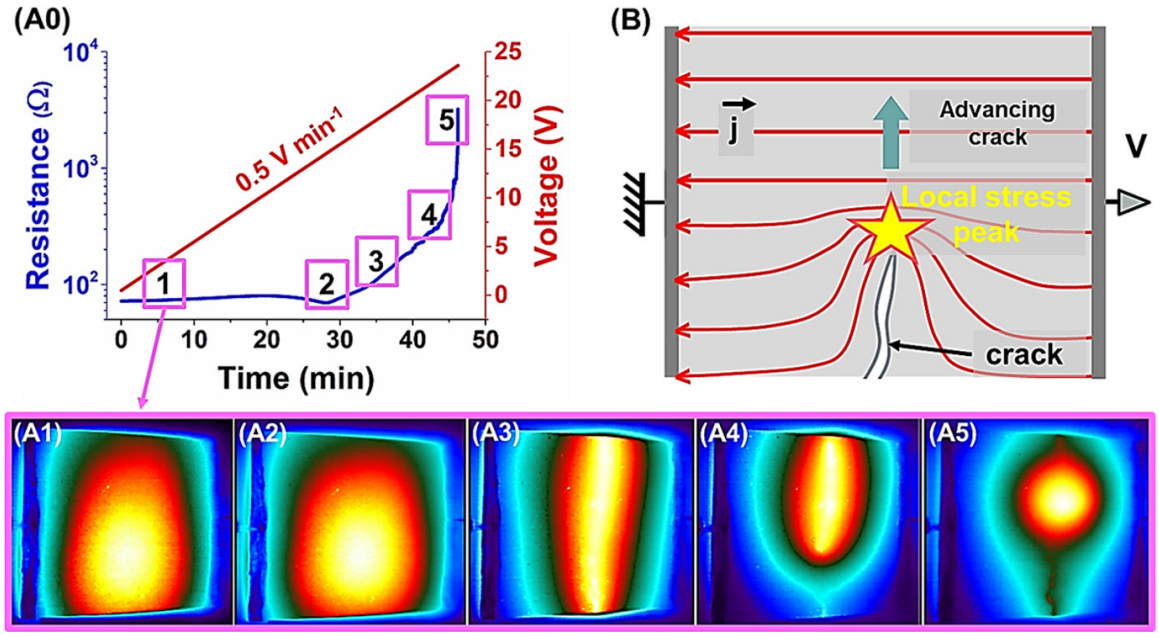

Figure 1.7: Time evolution of a physical nanowire sample subjected to a voltage ramp of 0.5 V/min. (A0) Evolution of resistance with time during voltage ramp. (A1-A5) IR images taken in chronological order of the crack advancing across the network perpendicular to the direction of current flow. Darker colors represent colder temperatures and brighter colors represent hotter temperatures. (B) Schematic diagram of crack propagation. Figure taken from [102].

vidual wires are very much distinguishable, known as the scale of percolating clusters [87]. One significant reason for this is that measurement is quite challenging. SEM and TEM are ideal for achieving the resolution necessary to analyze cluster failure in detail, but these microscopy techniques require high vacuum. This significantly alters surface diffusion which plays a key role in both spheroidization and electromigration. For example, Zhao et. al [132] have shown that, for single nanowires under electrical stress, electromigration is the primary cause of breakage. But there are reasons to be cautious when extrapolating from this experiment on single wires to systems of many interacting wires. First, because the measurements in [132] were taken under vacuum, but perhaps more importantly because networks of nanowires involve electrothermal fluxes flowing in many directions. It is not obvious that, given the myriad possibilities for interactions between wires, nanowire networks under ambient conditions will fail from the same causes as individual wires in vacuum.

All this said, if we can manage to predict exactly how silver nanowire networks will fail, we can obviate one of the main osbtacles to their ore widespread adoption. Furthermore, if we recast failure not as network destruction but rather as network transition into a less conductive state, we can turn this instability into an asset. As an example, recall that silver nanowires are extremely sensitive to sulfur. If we are able to predict exactly how and where a given network will fail, we could use small silver nanowire networks as chemical sensors. Just this year, an array of indium phosphide nanowires was used to create a self-powered NO_2 sensor with 84% sensing response to concentrations of 1 ppm NO_2 [124]. This brings us to the questions we seek to answer:

1. Can network topology and graph theoretic measures of importance predict how nanowire networks will reorganize under electrothermal stress?

2. Can a hybrid of experimental and computational techniques circumvent measurement problems and elucidate the reconfiguration dynamics of silver nanowire networks at cluster scale?

We will begin our discussion with a brief primer on graph theory as it undergirds a great deal of our analysis here. We will then discuss our procedure for created simulated nanowire networks and their corresponding graphs. Then we will apply some results of graph theory to these simulated networks thus demonstrating concretely the relevance of this branch of mathematics to silver nanowire networks. Motivated by these computational results, we proceed to creating high fidelity graph models of real nanowire networks with measurable properties and testing the predictive power of our graph theoretic approach. Finally, we will discuss some of the novel image processing techniques that we have developed in order to turn SEM images of nanowire networks into high fidelity in silico representations of these real nanowire samples. When all is said and done, we will have developed a new understanding of the cluster scale reconfiguration dynamics of silver nanowire networks and developed several new image processing routines that will be valuable to anyone seeking to extract non-planar graphs from images.

Chapter 2

Applying Graph Theory to Simulated Nanowire Networks

2.1 Graphs in General

Leonhard Euler initiated the field of graph theory, though he certainly would not have known it by that name, in his famous analysis of the seven bridges of Königsberg. The Pregel river runs through the city of Königsberg, which was then in the Kingdom of Prussia but is now known as the Russian city of Kaliningrad. In one part of town, as shown in Figures 2.1a-2.1b, there are two islands in the middle of the river. These islands are connected to each other and to either side of the river by a series of seven bridges. Euler wondered whether he could find some walking path through the city that would allow him to cross each of these bridges exactly once. He realized that

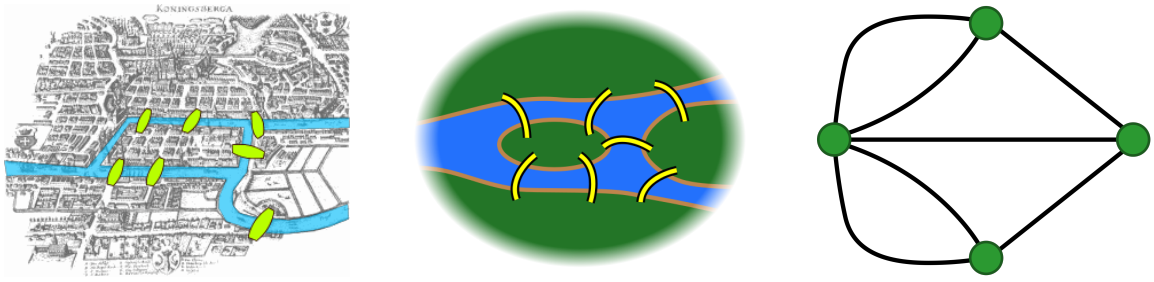

(a) Map (b) Diagram (c) Graph

Figure 2.1: The Seven Bridges of Königsberg, the origin of graph theory.

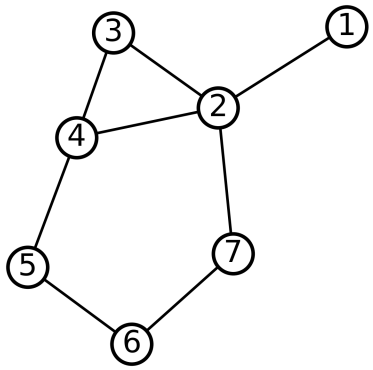

Figure 2.2: A graph with clearly labeled nodes represented by the numbered circles and edges represented by lines connecting the nodes. Image taken from [116].

the path he took on land was immaterial - it was only the bridges that mattered. He could therefore envision the system simply as a series of points with connections between some pairs of points, as shown in Figure 2.1c. The resolution of this problem is beyond the scope of the present discussion but the structure Euler developed, in which a system is represented by a series of objects and pairwise connections between the objects, is known as a graph.

Formally, a graph $G = (N, E)$ consists of a set N of objects called *nodes* (also known as *vertices*) and a set E of pairwise connections between these objects called *edges* [40]. An edge $e_{ij} = (n_i, n_j)$ is a two-set where $n_j, n_k \in N$. In the bridges of Konigsberg, the land masses are nodes (represented by green dots in Figure 2.1c) and the bridges are edges (represented by black lines connecting the green dots in Figure 2.1c). This structure is quite simple, but is so flexible that it can be used to represent nearly any kind of interaction in nature. In fact, in fundamental physics, it is only the strong nuclear interaction which cannot be represented by an interaction graph due to the presence of non-linear multibody interactions. Consider the graph shown in Figure 2.2 as another instructive example. Here we have the set of nodes N and

the set of edges E where

$$N = \{1, 2, 3, 4, 5, 6, 7\}$$

$$E = \{(1, 2), (2, 3), (2, 4), (2, 7), (3, 4), (4, 5), (5, 6), (6, 7)\}$$

Note that each edge here is a set and therefore the order of the two nodes within it does not matter. That is to say we could write the edges as

$$E = \{(2, 1), (3, 2), (2, 4), (2, 7), (3, 4), (5, 4), (5, 6), (6, 7)\}$$

and still be describing the exact same graph. This is because, unless stated otherwise, it is assumed that that the edge (n_i, n_j) allows one to travel $n_i \to n_j$ and $n_j \to n_i$. Graphs with this property are called *undirected* graphs. As anyone who has ever driven in Boston can tell you, however, there are some paths that can only be traversed in one direction. In a *directed* graph, each edge (n_i, n_j) only allows travel from n_i to n_j and not the other way around. It is however still possible to have two way travel between nodes n_i and n_j, it just requires two edges: (n_i, n_j) and (n_j, n_i).

It is also possible for edges to have some number (or numbers) assigned to them. Graphs for which the edges are assigned numbers are known as *weighted* graphs and the edge weight is usually regarded as analogous to edge length or distance. This might be relevant if you wanted to plan to get across the Pregel river and noticed that one of the bridges, evidently designed by an ancestor of both Escher and Mandelbrot, snakes up and down and left and right for quite some distance before reaching the other side. A *path* in a graph is an alternating sequence of nodes and edges in which neither nodes nor edges are repeated. For some graph we could write a path P as

$$P = n_1,\ e_{12},\ n_2,\ e_{23} \ldots n_{N-1},\ e_{N-1,N},\ n_N \tag{2.1}$$

where n_i are nodes in the graph and edge $e_i = (n_{i-1}, n_i)$ connects nodes n_{i-1} and n_i.

The length of such a path is simply the sum of the weights of the edges it contains (in a weighted graph) or the number of edges (in an unweighted graph). Equivalently, we can treat an unweighted graph as a weighted graph where all edges have unit weight.

2.2 Nanowire Networks as Graphs

In the graph representation of a nanowire network, each node represents a nanowire segment and each edge represents either a junction between distinct segments or an internal connection between different segments of the same wire. The edge weights are treated as resistances. An example of this process is shown in Figure 2.3. Creating a graph from a nanowire network begins by labeling each nanowire as shown in Figure 2.3a. Then we create an equivalent circuit, as shown in Figure 2.3b, including both the contact resistances between different nanowires and the internal resistances within a single wire. Note that this means wire y has been subdivided into two wire segments, y_1 and y_2. From the equivalent circuit, we can transition to a nanowire network graph as shown in Figure 2.3c. In the graph, nanowires/nanowire segments are nodes and resistors are edges. Each edge in this nanowire network graph also has a weight which is equal to the resistance of the corresponding resistor. These weights are usually treated as lengths so, in our case, short paths between nodes correspond to low resistance paths between nanowire segments. Note that the insertion of internal resistance edges in nanowires means that many segments may come from the same nanowire. There often arises some pictorial confusion here so this point bears repeating: nanowires, which appears as thin lines in an image, are represented by circles in a diagram of a nanowire network graph.

In graph theory, a node's importance is called its *centrality*. Importance, though, is highly contextual. What makes a node important will vary with the type of graph and with the behavior being examined [7]. There are, therefore, many types of centrality. Betweenness centrality, a measure introduced in [7, 34], is among the most influential [15] and is used to identify the nodes with the greatest control of flow in networks.

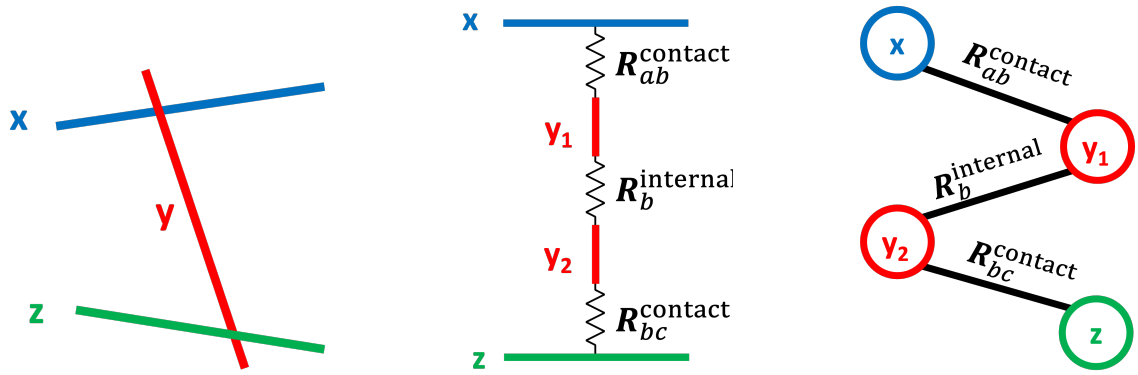

(a) Nanowire system (b) Nanowire circuit (c) Nanowire graph

Figure 2.3: (2.3a) Depiction of three nanowires labeled x,y,z and color coded. (2.3b) Circuit that is electrically equivalent to the configuration of nanowires in previous frame. (2.3c) Graph representation of nanowire system. Edges have weights equal to resistance values. Note that nanowires, which are originally represented as lines, become circles (nodes) in the final image and resistances become lines (edges).

As its name suggests, betweenness centrality measures a node's tendency to lie on shortest paths *between* other nodes. We proceed with a formal definition.

For some graph $G = (N, E)$, define σ_{st} to be the number of shortest paths from source node $s \in N$ to target node $t \in N$. We call such shortest paths $s - t$ paths. If t is unreachable from s, then $\sigma_{st} = 0$. If $s = t$ then σ_{st} is defined to be 1. A node v is *between* nodes s and t if v lies on one or more $s - t$ paths. In Fig. 2.4, for example, node 5 is between nodes 4 and 6. Define $\sigma_{st}(v)$ to be the number of $s - t$ paths that pass through v. We define $\sigma_{st}(v) = 0$ if $v \in \{s, t\}$. If v lies on the only $s - t$ path, then v has complete control over the flow from s to t and from t to s. If v lies on some but not all of the multiple $s - t$ paths, then v has only partial control over this flow. We define the *pair dependency* $\delta_{st}(v)$ as the fraction of $s - t$ paths that contain v.

$$\delta_{st}(v) = \frac{\sigma_{st}(v)}{\sigma_{st}} \tag{2.2}$$

The betweenness centrality of a node v, defined in Equation 2.3, is the sum of these pair dependencies over all possible source and target nodes in N. This measure captures the tendency of a node v to lie on shortest paths between all other nodes

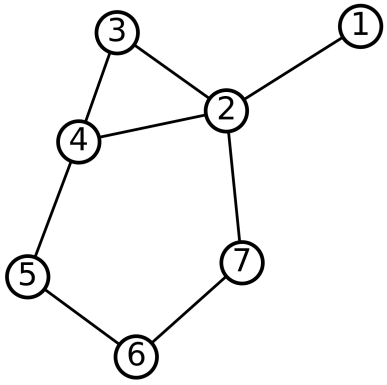

Node	Betweenness Centrality
1	0
2	7.5
3	0
4	3.5
5	1.5
6	1
7	1.5

Figure 2.4: An unweighted graph with nodes as numbered circles and edges as lines connecting the circles. Betweenness centralities shown in the table.

and therefore quantifies its degree of control of flow through the network.

$$C_B(v) = \sum_{s,t \in N} \delta_{st}(v) = \sum_{s,t \in N} \frac{\sigma_{st}(v)}{\sigma_{st}} \tag{2.3}$$

Note that we take $0/0 = 0$ by convention [16, 34].

Let us again consider node 5 from Fig. 2.4. Node 5 lies on the only shortest path between nodes 4 and 6; this pair dependency contributes 1 to the betweenness centrality of node 5. Node 5 lies on one out of two shortest paths between nodes 3 and 6; therefore this pair dependency contributes 1/2 to the betweenness centrality of node 5. Node 5 lies on no other shortest paths, so its total betweenness centrality is 1.5 as shown in Fig. 2.4.

For a more intuitive sense of betweenness centrality, consider the unweighted graphs shown in Figure 2.5. Note that we have shaded the nodes black and gray only to facilitate clearer discussion - the nodes are identical except for their connectivity. Every pair of distinct source and target nodes in 2.5a contains either two black nodes or one black node and one gray node. All shortest paths between black and gray nodes have length 1 and therefore include only the source and target nodes. Because $\sigma_{st}(s) = \sigma_{st}(t) = 0$, these paths will not contribute to betweenness centralities of nodes in the network. We therefore need only consider paths between two black

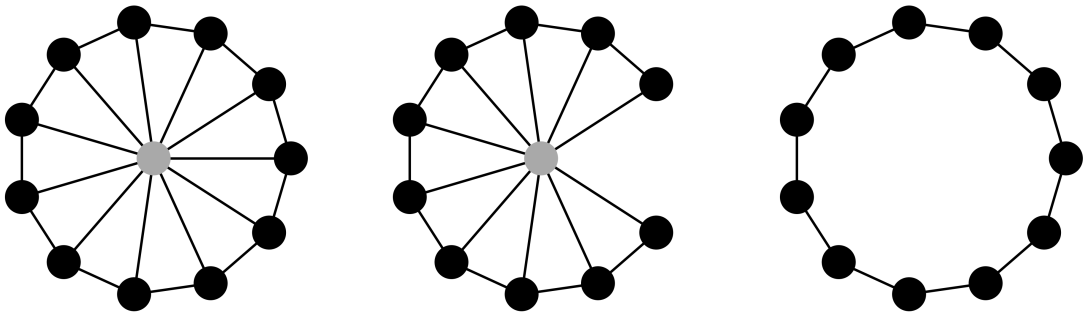

(a) Graph where the gray node clearly has the highest betweenness centrality. Average inter-node distance is 1.67

(b) Same graph but with a low betweenness centrality (black) node removed. Average inter-node distance is 1.65

(c) Same graph but with the high betweenness centrality (gray) node removed. Average inter-node distance is 3

Figure 2.5: Example graphs. Nodes are shaded only for clarity.

nodes to calculate betweenness centrality values. For every pair of black nodes, the shortest path between them either goes around the perimeter of the 11-gon or passes through the center. If the black nodes are directly connected by a single edge, then the path connecting them does not contribute to betweenness centralities of nodes in the network. If the black nodes have exactly one black node between them, they have two shortest paths: one path along the exterior black nodes of the 11-gon and one path passing through the center gray node. If the black nodes are separated by more than one black node, as is true for most pairs of black nodes, then the shortest path between them passes through the gray node. Given that most of the shortest paths between black nodes pass through the gray node, we should expect, correctly, that the gray node has a much greater betweenness centrality than the black nodes. We can see the effects of this by selectively removing nodes (and any adjacent edges) from the network. In Figure 2.5a, the average distance between nodes is 1.67. In Figure 2.5b, where one of the black nodes has been removed, the average distance between nodes actually decreases to 1.65. In Figure 2.5c, where the gray node has been removed, the average distance between nodes jumps to 3. Removing a low betweenness centrality (black) node had a very small impact on average inter-node distance while removing the high betweenness centrality (gray) node changed the average inter-node distance

by nearly a factor of 2. Thus we see that betweenness centrality offers a quantitative measure of a node's importance to transport through the network.

The motivation for this long discussion of betweenness centrality is its connection to one well motivated theory of nanowire network failure. It has been posited that nanowire networks fail at high resistance bottlenecks in otherwise low resistance paths [80]. Even for small networks, enumerating all possible paths is, in practice, impossible because number of possible paths grows so quickly with the number of nodes[1]. Betweenness centrality provides us with a calculable shortcut: high betweenness centrality nanowires are those nanowire that tend to lie on the highest conductivity (shortest) paths between other nanowires. Because of the highly unequal current sharing among wires in silver nanowire networks [82], these paths and the nodes they contain are a promising place to start applying our graph theoretic techniques to silver nanowire networks. Using the notion of centrality, we will optimize simulatd nanowire networks by strategically removing the least important wires, where importance is quantified in a variety of ways. An example of this procedure is shown in Figure 2.7. Selectively removing nodes from a network is generally called an *attack*, and the robustness of networks against attacks is frequently studied [53]. Previous scholarship, however, tends to focus on removing nodes in order from most important to least important [53, 51, 24] whereas we remove nodes in the reverse order: from least important to most important. This process will highlight the merits of different centralities and demonstrate that the semblant relevance of betweenness to nanowire networks is firmly grounded in reality.

2.3 De-densifying Silver Nanowire Networks using Betweenness-Based Centralities

To capture the properties of an MNW network, one must first create a virtual representation of a network. The discussion of how to do this is largely borrowed from

[1]Possible paths grow as $\mathcal{O}(|N|!)$ for the complete graph with $|N|$ being the number of nodes.

[87]. A simple method reported so far [70] for creating a virtual, square network of length L is described below, and illustrated in Figure 6:

1. Randomly generate a set of (x, y) pairs, which will serve as the nanowire midpoints, a set of angles, which will determine the nanowire orientations, and a set of nanowire lengths.

2. Create two wires of length L at the top and bottom (or left and right) of the sample. These will serve as the electrodes through which current is injected into or extracted out of the network.

3. Using the midpoints, angles, and nanowire lengths, calculate all points of intersection between line segments. This can be done by testing all pairs of line segments for intersection or, for more efficiency, using the Bentley-Ottmann Line Sweep algorithm [11]. The intersections between line segments are junctions between nanowires. Note that we use the terms *junction* and *contact* interchangeably.

4. Represent the network as a linear system of resistors. First add contact resistances at intersections between nanowires. Then, for each wire that has multiple contacts, subdivide it into multiple segments such that each division is equidistant from the nearest pair of contacts. The resistance of this internal resistor should be $R_{\text{internal}} = \rho\ell/A$ with ρ being the electrical resistivity of the nanowire, A being the cross-sectional area, and ℓ being the distance along the wire between the two nearest contacts. See the second panel of Figure 2.6 for a representation of this step.

5. Apply a voltage/current to the electrodes and solve the linear system for the potential of each wire and the current through each resistor. We have found it easiest to formulate this problem in terms of admittances and admittance matrices, but there are multiple ways to solve this system.

This approach presupposes several simplifications. First, the MNWs are assumed to interpenetrate and to lie in the same plane. This approximation is less rough than it

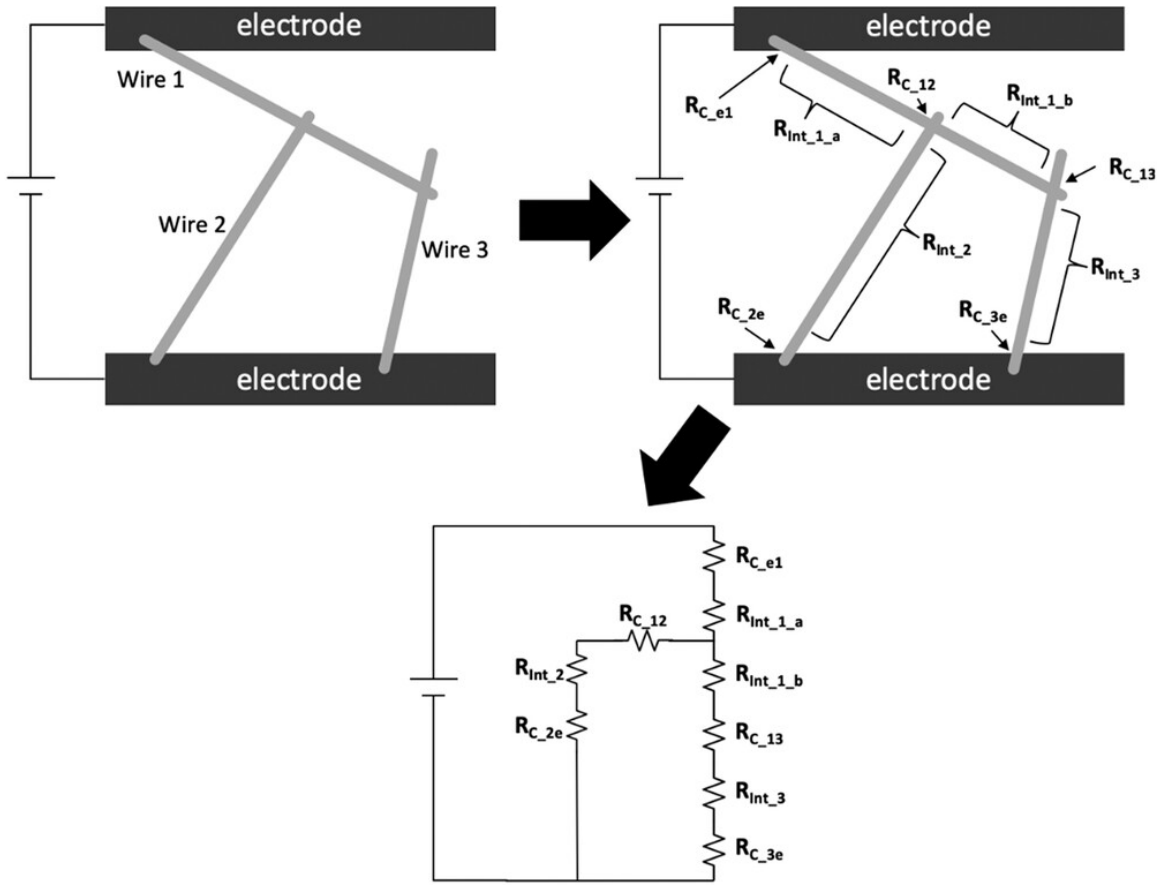

Figure 2.6: Diagram showing how a system of metal nanowires is mapped to the equivalent circuit. R_int denotes internal resistances and R_C denotes contact resistances. Figure taken from [87].

may seem: in many optimized networks the nanowires do interpenetrate (or overlap) significantly [56] and, furthermore, there is strong evidence that the assumption of interpenetration does not significantly affect the density threshold for percolation [126]. The second simplification is that the nanowires are treated as cylinders of constant diameter. This is done to allow for simple computation of the internal resistance of nanowire segments. Third, the nanowires are usually treated as though they are perfectly straight when, in reality, they can bend - sometimes considerably. Because straight lines cross at most once, this assumption that the nanowires are straight means that there can only be up to one contact between different nanowires. This, in turn, allows us to represent the system as a graph. If the nanowires can curve and are therefore able to cross more than once, the system must instead be represented a MultiGraph (a graph in which there can be multiple edges between the same pair of nodes). The final simplification is in the method by which contact resistances are assigned to junctions between nanowires. In reality, the quality of electrical contact between nanowires may depend on many factors—including contact area, angle, separation, and contamination on nanowire surfaces—and there is some evidence to suggest that such contacts may not even be ohmic without post-deposition optimization treatments [69, 10].

In the vast majority of models, however, all inter-wire contacts are assumed to have the same, ohmic contact resistance. Very little is understood about the microphysics governing electrical transport across MNW junctions. There is, however, experimental work which suggests that when activating AgNW junctions via electrical current, the majority of contact resistances lie between 0–50 Ω with a median value of 11 Ω [10]. These experimental values make accurate simulation possible for optimized networks even without a detailed understanding of the physics of junctions.

There are several common variations to the above simulation scheme. In some studies contact resistances are neglected entirely [117, 76]. In others [43, 42], the nanowires are not treated as idealized circuit components, but rather as 1D solids

with resistance per unit length given by ρ/A. Still, the framework described above, especially the computational geometry, serves as the backbone of nearly all network-scale nanowire electrical simulations. Of the many microscale knobs that can be tuned to affect macroscale behavior, the nanowire density, length, orientation, diameter, and contact resistance are most commonly adjusted.

We generate networks by modifying the procedure from [70] as described above in [87]. Each simulated network is square with side length 100 µm and with two horizontal 100 µm wires on the top and bottom serving as the cathode and anode (see Figure 2.7). All networks start at approximately the same density. Nanowires have length 10 µm, diameter 0.15 µm, and are considered to interpenetrate wherever they cross. Care must be taken when assigning junction resistances to the crossings between nanowires. As mentioned before, there are rather few measurements of single junction resistances in the literature. It is known, however, that the junction resistance may vary over several orders of magnitude depending on whether and how the network is optimized after deposition on the substrate [41, 52]. There have been successful endeavors to impute average effective junction resistances in well-defined films [84], but betweenness centrality is, in a sense, a measure of disorder. Therefore assigning equal resistances to all junctions would introduce an artificial homogeneity to our networks that confounds the behavior we seek to study. Instead, we choose to draw junction resistances from the empirical distribution in [10], with a median value of 11 Ω and an interquartile range of 13 Ω. This choice delivers physically reasonable average resistance values while preserving the variability in junction resistance that we expect in real nanowire networks. We account for internal resistance by subdividing nanowires into segments separated by internal resistors. The resistivity used to compute these internal resistances is calculated according to [13] assuming a temperature of 298.15 K. Centralities are calculated using NetworkX [45] and circuits are solved using Xyce [59].

All centrality measures are tested on the same set of 195 networks. This sample

size brought the standard errors for resistance and figure of merit to below 5% at all densities. The tested centrality measures, all of which are betweenness-based, are defined in Equations 2.4-2.7 for a graph $G = (N, E)$ where N is the set of nodes and E is the set of edges. Note that all of these definitions include normalization factors outside the summation. These normalizations are included here for the sake of completeness but are somewhat arbitrary and different authors have used different conventions over time. Because these normalization constants have no effect on the ordering of nodes within a single network by centrality value, they have no bearing on our results.

Betweenness Centrality (Weighted and Unweighted)

$$C_B(v) = \frac{2}{(|N|-1)(|N|-2)} \sum_{s,t \in N} \delta_{st}(v) \tag{2.4}$$

First introduced in [7, 34], Equation 2.4 shows the standard betweenness centrality multiplied by a normalization constant. This measure was originally conceived as a way to quantify the degree of control over information flow that an individual might have within a social network. The normalization in front scales values relative to the maximum number of shortest paths that a node can lie on in a network with $|N|$ nodes. Because $s-t$ paths are not counted as different from $t-s$ paths, this number is $(|N|-1)(|N|-2)/2$. This occurs on a star graph in which one central node is the only neighbor of each other node in the network [34]. Betweenness centrality has computational complexity $\mathcal{O}(|N||E|+|N|^2 \log |N|)$ using the algorithm from [15]. The definition in Equation 2.4 is used for both weighted and unweighted graphs, the only difference being in the calculation of each pair dependency $\delta_{st}(v)$. Betweenness centrality treats all paths in all directions equally during the summation of pair dependency $\delta_{st}(v)$. Our networks, though, lack rotational symmetry. Applying a potential across the cathode and anode, which are shown in Figure 2.6 as electrodes on the top and bottom of the network, destroys the two-fold rotational symmetry the network would otherwise have. There is reason to expect, therefore, that paths traveling in certain directions may be more important than others. For example, we

might expect paths traveling between nodes at identical voltages to matter less than paths traveling between nodes at very different voltages. Because the voltage tends to decrease from top to bottom, paths traveling vertically may therefore be more important than paths traveling horizontally. The centralities described in Equations 2.5-2.7 represent varying ways of accounting for this anisotropy.

Percolation Centrality

$$C_{\text{perc}}(v) = \frac{1}{|N| - 2} \sum_{s,t \in N} \delta_{st}(v) \frac{V(s)}{[\sum_w V(w)] - V(v)} \tag{2.5}$$

First introduced in [93], Equation 2.5 shows the percolation centrality where $V(x)$ is the percolation state (in our case voltage) of the node x. V is restricted to vary between 0 and 1. Percolation centrality is normalized so the average path weight is 1. Computational complexity is $\mathcal{O}(|N||E| + |N|^2 \log |N|)$ using the algorithm from [15]. Percolation centrality was first introduced in the context of epidemiology [93] and is useful when the states of nodes evolve in time. Aside from the choice of normalization, percolation centrality differs from betweenness centrality only in the weight assigned to each pair dependency, $\delta_{st}(v)$. The betweenness centrality has a unit weight for each pair dependency whereas the percolation centrality weights the pair dependency by the percolation state of the source node s. This gives more weight to paths starting at nodes s with higher percolation states. In our system voltage is the percolation state, so percolation centrality weights as more central those nodes that tend to lie on paths starting at higher potentials.

Current Weighted Centrality

$$C_{\text{curr}}(v) = \frac{1}{I_{\text{sys}}(|N| - 2)} \sum_{s,t \in N} \delta_{st}(v) \frac{\text{ramp}\,[V(s) - V(t)]}{R_{st}} \tag{2.6}$$

Introduced in [116], Equation 2.6 defines the current weighted centrality. I_{sys} is the total current through the nanowire network; R_{st} is the length (resistance) of the shortest path from s to t; the ramp function is defined as $\text{ramp}[x] = \max(x, 0)$. These measures are very similar to the source and target dependent percolation centrality

defined in [93] and have computational complexity $\mathcal{O}(|N|^3)$. The pair dependency weight in the current weighted centrality is equal to the current that would flow through the $s-t$ path if the path were electrically isolated with nodes s and t maintaining their current voltages. This measure attempts to rank as more central those nodes lying on paths that carry large currents.

Electrode Centrality

$$C_{\text{elec}}(v) = \frac{1}{(|N|-1)(|N|-2)} \sum_{s \in S, t \in T} \delta_{st}(v) \tag{2.7}$$

Introduced in [116], Equation 2.7 defines the electrode centrality where S, $T \subset N$ are the sets of nanowire nodes touching the cathode or anode respectively. Only paths that flow down potential at every edge are considered. This measure, then, only counts nodes that lie on a small number of high conductivity paths between the electrodes. Note the normalization is divided by 2 relative to betweenness centrality because the down-potential criterion is enforced by treating the graph as directed thus doubling the maximum possible unnormalized betweenness centrality. This measure is a variant of betweenness subset centrality [45]. The primary advantage of electrode centrality is its speed: because we only need to consider shortest paths between subsets of nodes, shortest path calculation and pair dependency accumulation are accelerated dramatically. Technically this measure has the same asymptotic computational complexity as the betweenness centrality but the prefactors are considerably smaller.

We test the ability of a particular centrality measure to de-densify by observing the evolution of the network's resistance and FOM as nanowires are removed in order from lowest to highest centrality values. An example of this process is shown in Figs. 2.7a-2.7d. Note that betweenness centrality is defined for nodes and each nanowire may contain many nodes. We consider the betweenness centrality of a nanowire to be the maximum centrality among the nodes it contains.

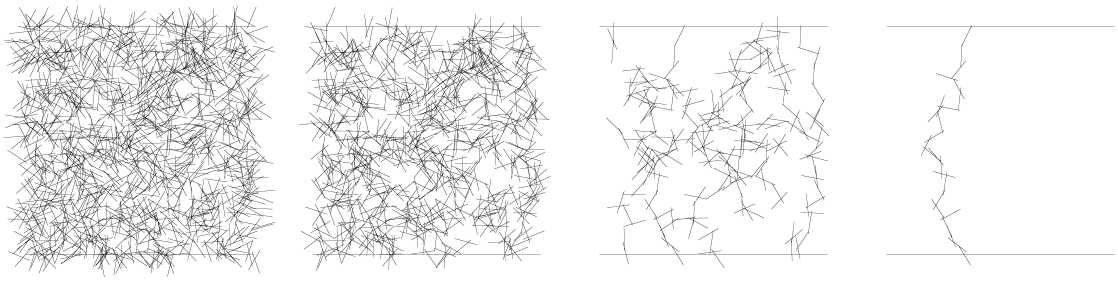

(a) Start density = 2.2 (b) Density = 1.5 (c) Density = 0.4 (d) Density = 0.041, just before failure

Figure 2.7: Example network as nanowires are removed in order of increasing betweenness centrality value. Densities expressed as multiples of n_c^{eff}(see Equation 2.10 for definition).

We define the network's resistance as the series resistance between the cathode and anode. For the FOM calculation, we treat the series resistance between the cathode and anode as equal to the sheet resistance, although this is only strictly true for homogeneous materials. A single trial consists of removing nodes from a network, in the order dictated by a given centrality measure, until the next node removal would render the anode unreachable from the cathode. When the cathode and anode are thus disconnected, we say that a network has failed.

It is worth noting that the removal of a node may affect the centralities of other nodes in the network. We calculate the centrality values of a network's nodes only once - before any nodes have been removed - and use these values for the duration of the simulation. As nodes are removed, then, our centrality values become less accurate. Our results demonstrate that even with this approximation we can successfully de-densify networks to well below the percolation threshold while preserving much of their conductivity.

Transparency calculations are carried out using the formalism developed in [60] where the transparency is given as

$$T = e^{-n_s C_{\text{ext}}} \tag{2.8}$$

where n_s is the number of nanowires per unit area and C_{ext} is the extinction cross sec-

tion for a silver nanowire assuming Mie scattering [96]. Nanowires are approximated as infinite cylinders - we calculate scattering per unit length. We assume normally incident light propagating through vacuum with wavelength 550 nm. We take silver's refractive index at 550 nm to be $0.055+3.32i$ [120] and the surrounding air's refractive index to be 1 [22]. An explicit calculation is shown in Appendix A.1.

Fig 2.8 shows the evolution of network sheet resistance and FOM, averaged across 195 networks, as nanowires are removed from lowest to highest centrality for each of the centralities in Equations 2.4-2.7. The plots also includes the behavior or an "Optimal" network comprising a regularly spaced grid of wires at the given density. The expression for the resistance of this optimal system is shown in Equations 2.9 where L is the network side length, ℓ is the wire length, $\langle R_c \rangle$ is the mean of the empirical contact resistance distribution from [10], and R_w is the internal resistance for a single nanowire. This expression arises by creating a square grid network where the sum all nanowire lengths is equal to the sum of all nanowire lengths in the random network at the same density, as shown in Figure 2.9. A derivation of Equation 2.9 is shown in Appendix A.3.

$$R_{\text{optimal}} = 2\frac{\frac{L}{\ell}R_w + \left(\frac{L}{\ell}+1\right)\langle R_c \rangle}{n_s L \ell} \tag{2.9}$$

For each centrality measure, we plot its evolution from the average starting density of roughly 2.2 until the highest density at which a network has failed. Figure 2.10 shows, for each centrality, the distributions of densities at which the resistance doubles and at which networks fail. Densities in Figures 2.8 and 2.10 are all measured relative to the effective percolation threshold, n_c^{eff}, which is the *size dependent* density at which there is a 50% chance of a cluster connecting the cathode and anode in a finite network. The effective percolation threshold is found empirically in [70] to be

$$n_c^{\text{eff}} = \frac{5.63726}{\ell^2} + \frac{1}{\ell L} + \frac{5.5}{L^2} \tag{2.10}$$

where L is the network side length and ℓ is wire length.

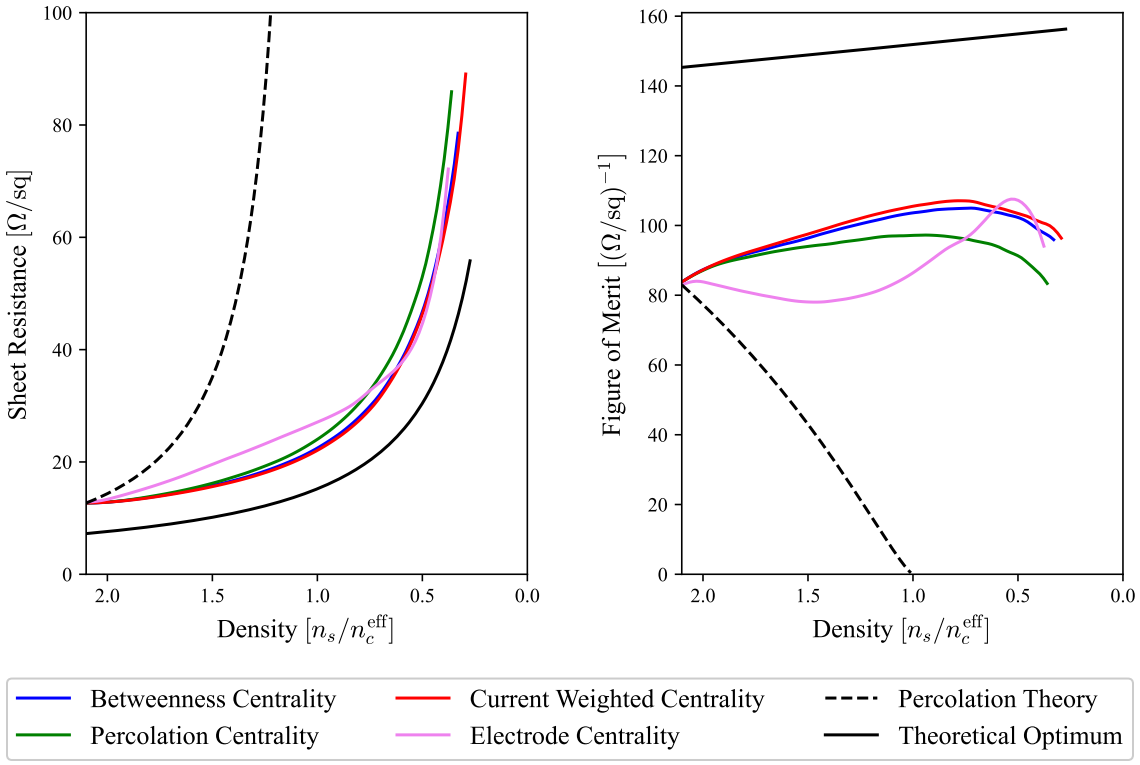

Figure 2.8: The evolution of Sheet Resistance and Figure of Merit (FOM), averaged over 195 networks, as density is decreased by removing nodes in order from lowest to highest centrality value for each of the centrality measures in Equations 2.4-2.7. As a reference, we also show the behavior predicted by percolation theory and the behavior of the "Optimal" square grid network with resistance values given by Equations 2.9. Standard errors are comparable in size to line thickness and are therefore omitted.

Percolation theory predicts that, slightly above the effective percolation threshold, the resistance scales as

$$R \propto (n_s - n_c^{\text{eff}})^{-\gamma} \tag{2.11}$$

with γ being a positive constant. We would therefore expect network resistance to diverge around the effective percolation threshold ($n_s/n_c^{\text{eff}} = 1$). However, the resistance plot in Figure 2.8 shows that all networks in which nodes are removed in increasing order of centrality show finite resistance well below the percolation threshold. This is

Figure 2.9: Two nanowire networks, one random (left) and one square grid (right). The cumulative length of nanowires in each network is equal, as are their areas, giving them equal density. In our formalism, then, they would have the same transparency and differences in the figure of merit arise purely from differences in electrical resistance.

because, while percolation theory assumes a random network, networks optimized by removal of low centrality nodes are decidedly non-random. A similar plot of haze as a function of resistance, using the formalism developed in [60], is included as Appendix A.2. Furthermore, the distributions shown in Figure 2.10 show that networks fail at densities considerably lower than 1; the median failure density for all centralities tested is less than 14% of the effective percolation threshold. These data suggest that betweenness centrality, percolation centrality, current weighted centrality, and electrode centrality arrive at roughly the same densities before causing failure, but electrode centrality is slightly less effective than the other centrality measures at preserving low resistance along the way.

The figure of merit trajectories, however, are considerably different. All FOMs initially increase slightly during the first removals of nanowires - this is caused by the initial removal of nanowires that degrade transparency without contributing meaningfully to conductivity. Beyond this initial improvement, the electrode centrality FOM decreases while the others increase. The electrode centrality FOM trajectory, although it starts off worse than all others, eventually reaches the highest figure of merit shown on the FOM plot. While this might seem to suggest that electrode centrality is the most promising of the measures discussed here, our approximation that series resistance equals sheet resistance very likely breaks down at this density.

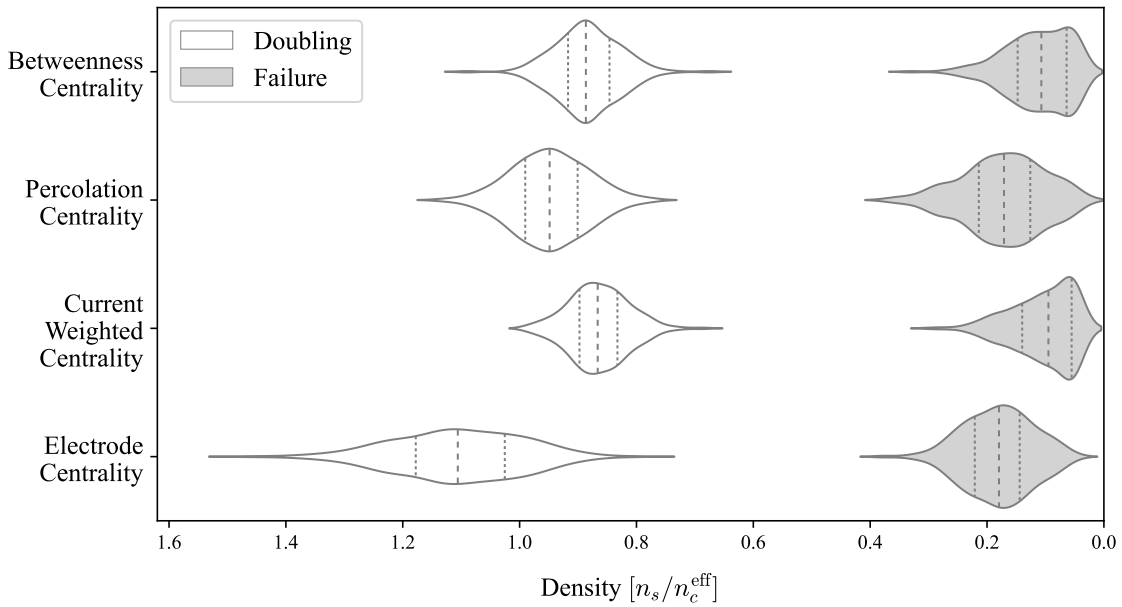

Figure 2.10: Violin plot showing the distributions of densities at which resistance doubles (white) or networks fail (grey) as nodes are removed in order from lowest to highest centrality value for each of the centrality measures in Equations 2.4-2.7. Dashed lines show quartiles.

Looking at Figure 2.7c we can see that, at a comparable density, the network is not just inhomogeneous but *far* from even approximate homogeneity. Furthermore, the figure of merit defined in Equation 1.1 is not comprehensive - most practical applications for TEs demand low resistance and, for sufficiently high resistances, there is no amount of transparency that can compensate. Thus we would better served to focus on the earlier stages of evolution where the resistance is quite low and the material is more homogeneous. In this density regime, the electrode centrality underperforms the other measures.

At this point, our choice of a regular square grid network as "optimal" merits a bit of further scrutiny. There is no method of de-densifying a random nanowire network that could possibly reach the performance of the square grid network because de-densification cannot change the positions or orientations of nanowires to make a grid. Instead, it would make more sense to compare betweenness based de-densification to another strategy based on node removal. It would be technically possible to find the perfect de-densification scheme by a brute force search, but the scaling behavior

of this problem makes this approach extremely impractical. In a nanowire network containing N wires, there are $N!$ possible ways to remove the wires one by one. However, the properties of this system are not path dependent - a network in which nodes $\{1, 2, 3\}$ have been removed has the same properties regardless of the order in which those nodes were removed. This reduces the computational complexity considerably. To find the highest possible FOM achievable by node removal, we need only enumerate all possible states without regard for how these states are reached. We can uniquely identify a state by the collection of nanowires that have been removed. Therefore the number of possible states that can be reached by removing k of the N nanowires is simply the number of ways to choose k items out of a larger collection of N items, i.e. $\binom{N}{k}$. If we define S as the number of possible states we have

$$S = \sum_{k=0}^{N} \binom{N}{k} = 2^N \tag{2.12}$$

where the final equality results from the binomial theorem. Our simulated networks contain thousands of nanowires, so if we set $N = 1000$ we get $S = 2^{1000} \approx 10^{300}$.

Let us put this in more concrete terms. As of June 2023, the top ten fastest supercomputers in the world have a combined peak speed of 3675.79 PFLOPS. If we assume that enumerating a state and calculating its transparency and resistance requires only a single floating point operation (a gross underestimate) and that we could use the entire combined computing power of these top ten supercomputers, this process would take us roughly 10^{274} years. As a comparison, age of the observable universe is roughly 13.8×10^9 years.

As it happens, problems which scale in this manner are actually relatively easy to find in computer science. As a result, there has been considerable research concerning how to optimize an objective on such a large decision space. One such method is Monte Carlo Tree Search [23] also known as MCTS. MCTS samples a decision tree and uses statistics to make informed estimates of the likely rewards of given actions.

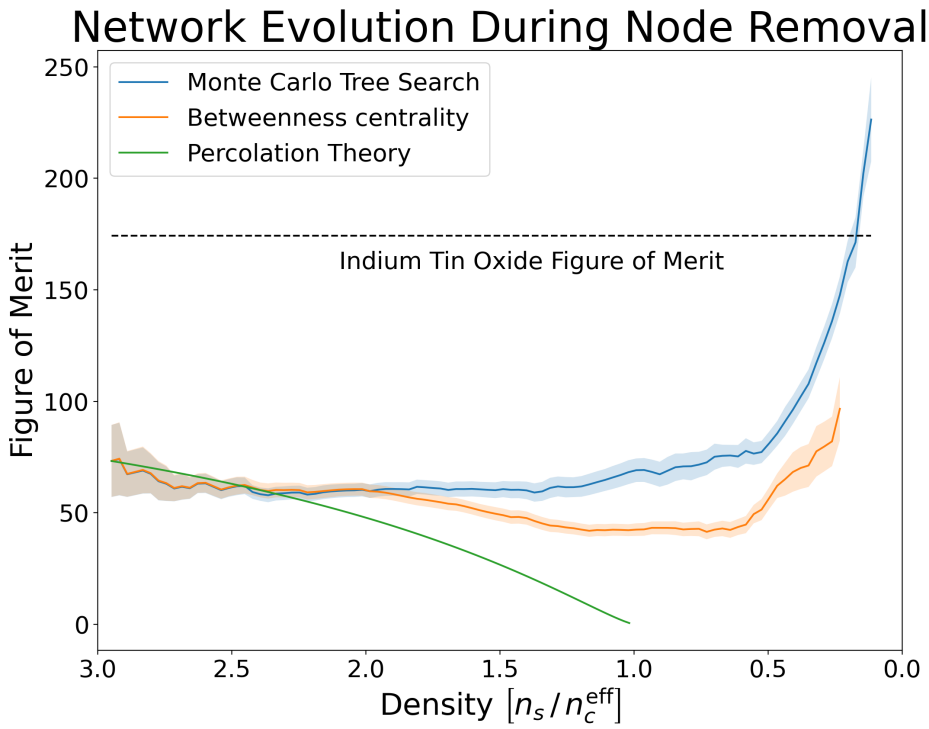

Figure 2.11: Evolution of the transparent conductor figure of merit (FOM) as nodes are removed from the network according to a strategy produced by Monte Carlo Tree Search. This data averages behavior over 50 trials on 25 µm square networks.

MCTS, combined with deep neural networks, is responsible for the recent dramatic improvements in AI gameplay achieved by AlphaZero in Chess and Shogi [108] as well as the game of Go [1]. Even without neural networks, though, MCTS represents a powerful optimization scheme for systems with well defined rules that are nonetheless computationally challenging. With this in mind, we can use MCTS as a technique for finding the set of removed nodes that maximizes the FOM of a given simulated nanowire network. A good general reference for this technique is [17]. The details of our particular implementation are discussed in Appendix A.5.

Figure 2.11 shows the evolution of the TCE figure of merit as nodes are removed according to a strategy produced by Monte Carlo Tree Search. Also shown are the evolution of FOM as nodes are removed in increasing order of betweenness centrality, and the evolution of FOM predicted by percolation theory. In Figure 2.8, the gap between the betweenness centrality trajectory and the "optimal" trajectory is

significant. If we take the MCTS trajectory to be a more realistic optimum for the reasons discussed in paragraphs bove, we see here that betweenness centrality based de-densification performs very nearly as well as the optimal strategy. This indicates that betweenness centrality does indeed do a good job of identifying those nodes that are important to conduction.

In this chapter we have considered four betweenness-based centrality measures and examined their abilities to de-densify simulated nanowire networks while preserving high conductivity. Two of these centrality measures, current weighted centrality and electrode centrality, introduced in my previous work [116], were specifically designed to account for the asymmetry inherent in nanowire networks under electrical bias.

In general, the betweenness-based de-densification methods work reasonably well, achieving FOM improvements from 16.1% to 29.7% relative to the start. This success is not entirely surprising. The number of contacts a nanowire makes with neighboring nanowires (assuming all are straight) is Poisson distributed [50]. This means that, if we neglect internal resistance, nanowire networks have Poisson degree[2] distributions. Erdös-Renyi (ER) [31] networks also have poisson degree distributions for sufficiently large numbers of nodes [6]. Because attacks that remove nodes in order from highest to lowest betweenness centrality have been shown to degrade ER networks faster than random removal [53], it is reasonable to expect the removing nodes in order from lowest to highest centrality would degrade networks more slowly than random removal and therefore more slowly than percolation theory as well.

Although these results are not terribly surprising, the analysis shows interesting merits. As previously mentioned, attacks are a common tool to investigate the vulnerabilities of networks [53, 51, 24]. However, among networks where conductivity is a desirable property, we know of no example of an attack improving the network.

In terms of improving the network, standard betweenness centrality and current

[2]The degree of a node is the number adjacent edges

weighted centrality appear to be the best measures as they achieve the highest figures of merit at almost all densities. Current weighted centrality considers network topology and the network's electrical state while betweenness centrality considers only network topology - it is therefore surprising that the two measures perform so similarly. The networks modified by current weighted centrality reach a maximum average figure of merit of 107 (70% of the theoretical optimum) and the networks modified by betweenness centrality reach a maximum average figure of merit of 105 (68% of the theoretical optimum). The improved performance of current weighted centrality comes at a cost though: the algorithm for calculating current weighted centrality is almost identical to that for calculating target dependent percolation centrality [93] and therefore runs in $\mathcal{O}\left(|N|^3\right)$ time whereas the algorithm for calculating betweenness centrality on a weighted graph runs in $\mathcal{O}\left(|N||E| + |N|^2 \ln |N|\right)$ time [15]. Because betweenness centrality performs so similarly to current weighted centrality but is considerably cheaper to calculate, betweeness centrality seems the most promising measure for future study.

While it is impractical to suggest that nanowire meshes should be optimized at industrial scale by removing individual nanowires, there are clear and promising next steps for extracting general design principles and integrating simulations with experiments. Using the resistivity calculations from [13] and the contact resistances from [10], we can calculate betweenness centrality values for real nanowire networks simply by analyzing images. By identifying regions that tend to contain high betweenness centrality nanowires, we may be able to achieve a higher FOM by density patterning during nanowire depositon. Furthermore, it has been posited that hot spots arising from Joule heating are most likely to form in high resistance regions of otherwise highly conductive pathways [80] and betweenness centrality is a natural candidate to identify these regions. By imaging nanowire networks before and after electrically induced thermal failure and calculating betweenness centralities from these images, we could connect position, betweenness centrality, and probability of failure. This is exactly the strategy we pursue in the following chapter. Selectively depositing extra

nanowires in the regions most likely to fail could harden nanowire networks against electrically induced thermal failure and thus obviate a significant obstacle to their widespread adoption as TEs [87]. In addition, we could reproduce the simulations performed here on real nanowire networks by using a FIB or high dose SEM to sever those wires that are deemed to have the lowest betweenness centrality. Repeating this process and taking sheet resistance measurements along the way would allow us to confirm the trend of finite sheet resistance well below the percolation threshold. Betweenness centrality and other betweenness-based centrality measures, then, show great promise in the rational design of nanowire networks. Furthermore, the mathematical tools discussed here are quite general. By removing low betweenness centrality nanowires, we were removing network components whose contribution to performance was not worth their cost to transparency. Networks in which performance comes at a cost are quite ubiquitous. To name just one example, consider a cell phone company. By identifying the cell towers with the lowest betweenness centralities, one could also identify those towers that could be decommissioned to cut costs while inflicting the least damage on cell coverage. Our optimization scheme, then, shows great promise for application to any network in which performance comes at a price.

Chapter 3

Joining Computation with Experiment

Because most indium is used in the production of ITO, alternative TCEs can obviate present supply problems by replacing ITO wherever possible and, in so doing, increase the availability of indium for those applications in which it cannot be replaced. Networks of metallic nanowires, especially of silver nanowires, have the capacity to replace ITO in many applications and, because these meshes are mechanically flexible, they can be used in applications where ITO cannot. The primary obstacle to more widespread adoption of this promising nanomaterial is stability: meshes of silver nanowires generally do not last as long as ITO. Silver nanowire networks fail from spheroidization, electromigration, chemical corrosion, or a combinations of these factors which can all be accelerated by the high temperatures to which TCEs are regularly subjected [87].

A great deal of research focuses on combating the electrothermal and chemical instabilities that plague nanowire networks [87, 77, 19, 133, 79, 5, 67, 44, 62] and identifying the operating conditions that tend to make these materials fail [119, 20, 19, 61]. Of the aforementioned causes of failure, electrothermal failures are especially important because all nanowire-based TCEs are expected to carry current by definition and therefore will also generate some heat. The dominant microscale mechanisms

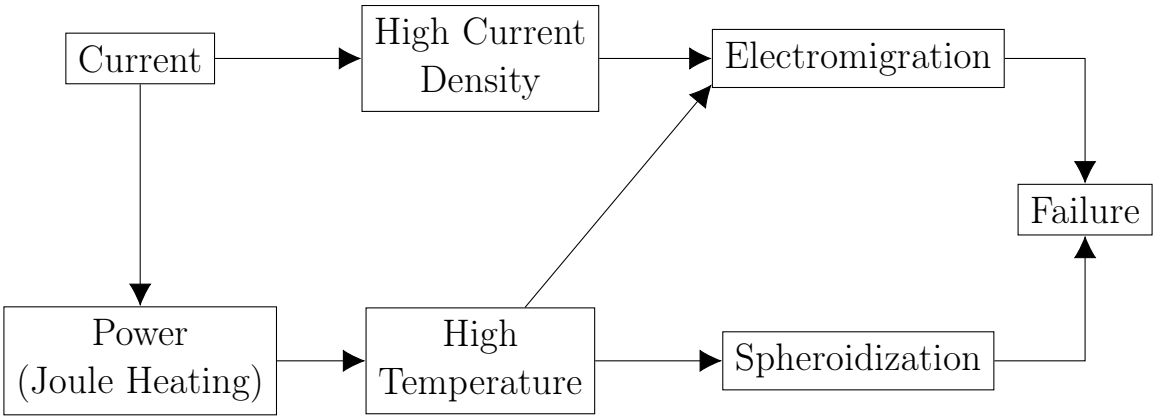

Figure 3.1: A causal graph showing the drivers and mechanisms of nanowire failure under typical operating conditions.

of electrothermal failure are electromigration and spheroidization. Present literature suggests electromigration is not typically observed in full silver nanowire networks, especially when in contact with a substrate of low thermal conductivity [87]. The absence of evidence of electromigration is not, however, proof that electromigration does not occur. For single silver nanowires on the other hand, there is strong evidence that electromigration dominates failure in vacuum under electrical bias [132]. There are two good explanations for this inconsistency. First, nanowire networks contain contacts between nanowires and these play a crucial role in failure dynamics [88]. Second, electromigration and spheroidization are both mediated by surface diffusion which may behave differently outside a vacuum [87]. The question of which failure mechanism dominates in full nanowire networks is further complicated by the highly coupled causal chain that leads to electromigration and spheroidization, as shown in Figure 3.1. In typical silver nanowire networks under electrothermal stress, everything begins with current (top left of Figure 3.1). If nanowire diameters are small, current can yield high current densities which in turn cause electromigration and failure. But current also dissipates power in the form of joule heating and can therefore lead to high temperatures. This can lead to high temperatures which are believed to be the primary driver of spheroidization. High temperatures also increase surface diffusivity [88] thus accelerating both spheroidization and electromigration.

It is also not well understood why specific regions of nanowire networks fail while others remain intact. With the goal of identifying the dominant electrothermal failure mechanism and better understanding the spatial dynamics of failure in nanowire networks under realistic operating conditions, we perform a combined computational and experimental analysis. First we fabricate physical nanowire network samples that are small enough to be computationally tractable but large enough to display the complex network dynamics present in macroscale systems. We then construct *in silico* graph models of these networks based on SEM images, subject the physical samples to a voltage ramp until resistance diverges, and re-image the networks to see which specific elements have been destroyed. This allows us to test hypotheses about nanowire failure in graph theoretic terms.

This is motivated by previous work in Chapter 2 and [116] in which we have shown that that betweenness centrality can identify components of simulated nanowire networks that are disproportionately important to conduction. Given that high centrality paths tend to carry more current, it is reasonable to expect that they might be more likely to fail as well, since current ultimately drives both electromigration and spheroidization. Specifically, we examine whether betweenness centrality and related measures can be used to predict the specific locations of nanowire network electrothermal failures. By taking careful experimental measurements and creating simulated graphs corresponding to each experimental sample, we can infer values of betweenness centrality, percolation centrality, power dissipated by joule heating, and current to test their predictive ability and identify dominant failure modes. In doing so, we aim to develop a better understanding of the interplay between network-scale and local effects as they relate to failure. All source data from this study will be made available to the broader community of nanomaterial engineers.

Going from real nanowire networks to high fidelity *in silico* representations compatible with the aforementioned calculations imposes several constraints on our exper-

imental samples. First, the areal number density of nanowires must be high enough to achieve percolation but low enough that individual nanowires can still be identified in the visual field during microscopy. The percolation threshold, for our purposes, can be defined as the areal number density at which there is a 50 % chance that a conductive path exists from one side of the network to the other (i.e. between a voltage source and ground located on opposite sides of a sample). This critical density n_c takes the form

$$n_c = \frac{5.63726}{\ell^2} \tag{3.1}$$

where ℓ is the length of the nanowire [92, 75], although this only holds asymptotically as the size of the sample approaches infinity. For finite samples, the threshold increases as the sample size decreases [70], as discused in Chapter 2. At the length scales typical of commercial nanowires, a $1\,\mathrm{mm}^2$ sample at the percolation threshold will contain thousands - and possibly tens of thousands, of nanowires. This would make image analysis extremely time consuming and therefore sub-mm samples are required. At this scale, though, the increased percolation threshold becomes relevant and, at the low densities necessary for imaging, there is a reasonable likelihood that a given sample will not percolate. Furthermore, it is quite difficult to precisely control the areal density of nanowires with drop casting. It therefore becomes necessary to fabricate a large number of samples to ensure that at least some are percolating. In summary, this experimental design requires a large number of sub-millimeter scale networks with areal densities of nanowires that are neither too high nor too low. A procedure for fabricating samples that satisfy these constraints, is detailed in Figure 3.2 and a description of the samples themselves is shown in Figure

Each isolated nanowire network on the slide is imaged via SEM and then subjected to a voltage ramp on a probe station at a rate of $1\,\mathrm{V\,min}^{-1}$ until it fails. This process is shown in Figure 3.3. The data collected during the voltage ramp (time, current, voltage, resistance) make it extremely clear when failure occurs as the resistance increases by at least three orders of magnitude within a single time step of

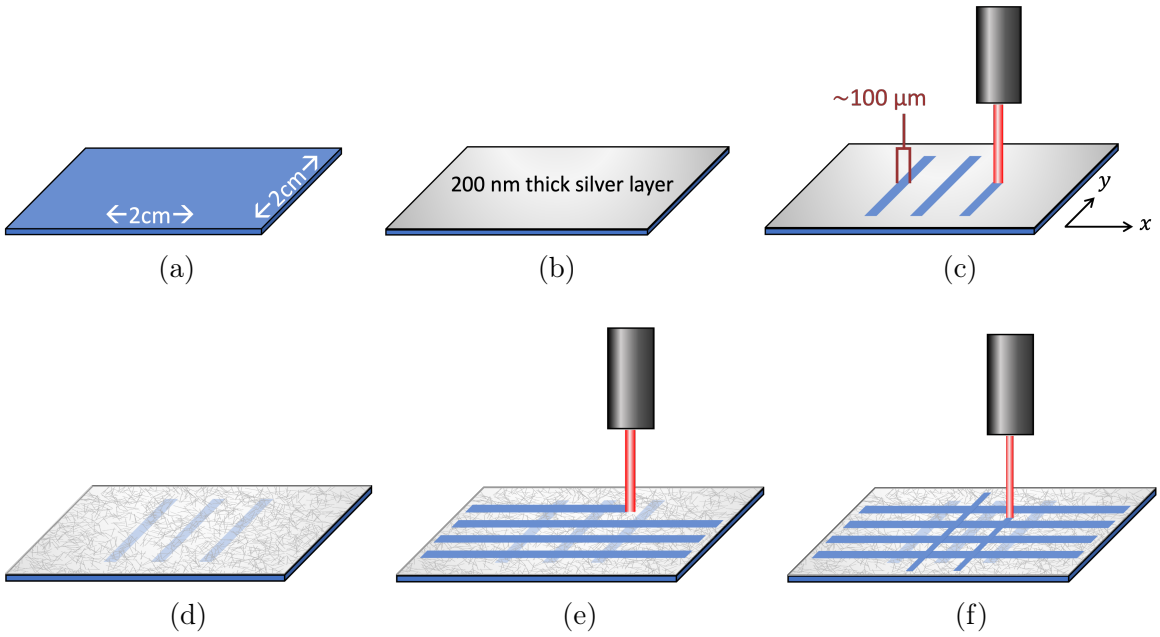

Figure 3.2: (3.2a) Fabrication begins with a 2 cm by 2 cm glass slide. (3.2b) Electron beam evaporation of 200 nm thick layer of silver onto glass with 10 nm chromium adhesion layer. (3.2c) A laser scribe set to maximum raster spacing scans in the $\hat{y}$ direction to ablate away the silver creating insulating channels in which the glass is exposed. Channels are roughly ≈100 µm wide. (3.2d) The silver nanowire suspension (aqueous Ag120 from ACS Material, 120 nm diameter, 30–50 µm length) is drop cast onto the slide and dried. (3.2e) The laser scribe scans again but this time cutting in the $\hat{x}$ direction. This removes both the evaporated silver and the silver nanowires thus creating insulating boundaries between adjacent rows of samples. (3.2f) The laser scribe scans once more in the $\hat{y}$ direction to create insulating boundaries between adjacent columns of samples. Repeated laser scribing causes the glass to crack in many instances, and thermally annealing the sample after laser scribing causes the glass to crack reliably. Therefore no usable samples were thermally annealed and, as a result, the contacts in these usable samples are unlikely to have sintered. To ameliorate the problem of the cracking glass, the laser was defocused in the third batch of samples to spread radiant energy over a larger area. This resulted in slightly smaller samples in the third batch. In some cases on this third batch, the final laser scribing step caused a substantial portion of the nanowires on the sample to spheroidize thus destroying conductivity between the electrodes. In these cases, additional nanowires were drop cast onto the slide and the third scribing step was repeated with a razor blade rather than the laser.

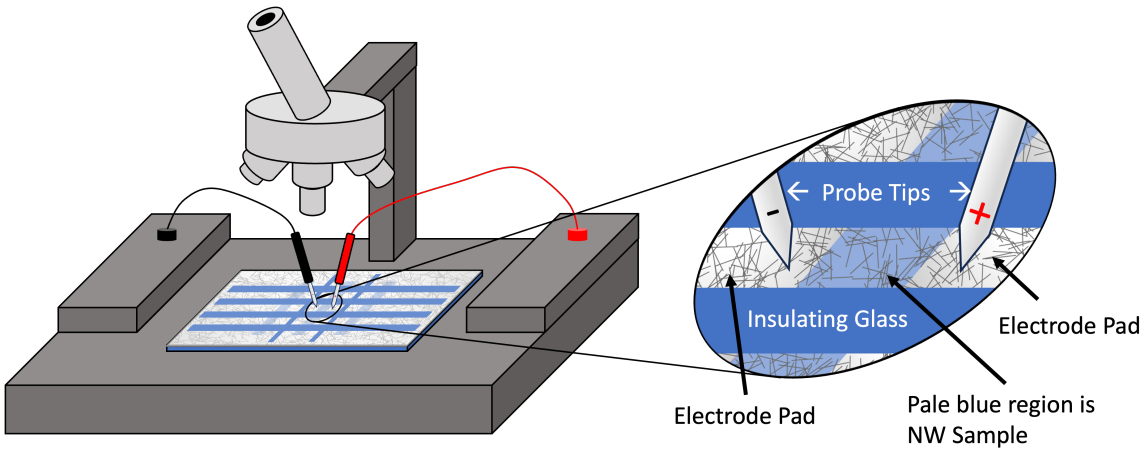

(a) Diagram of probe station setup

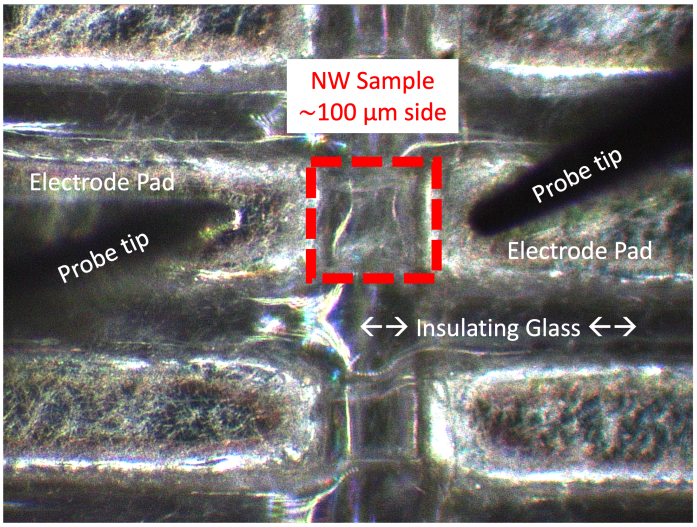

(b) Image taken through probe station optical microscope

Figure 3.3: Diagram (3.3a) and microscope image (3.3b) of the probe station setup. Note that each sample (example enclosed by red dotted line) is a region that was scribed in the first laser step and is now bounded on the left and right electrode pads and on the top and bottom an insulating glass channel.

1 s. As shown in the closeup of Figure 3.3, the positive and negative probe tips are placed on the evaporated silver electrode pads to the left and right of the sample. While the probe tips certainly come into contact with some nanowires in addition to the evaporated electrode pads, we assume that conduction through these peripheral nanowires is negligible compared to the conduction through the electrode pads and that, therefore, the vast majority of the current flowing through the sample region goes from probe tip to electrode pad to nanowire sample to other electrode pad to other probe tip. After failure, the sample is imaged again via SEM.

Image analysis begins by manually overlaying the pre-ramp and post-ramp images to match scale, position, and orientation. Quantitative size information is extracted from scalebars. The overlaid images are then annotated by manually tracing over each nanowire on an iPad. The goal of this tracing is to reconstruct the network as it was before the voltage ramp. Each trace is treated as an instance segmentation mask for an individual wire. The traces are processed as shown in Figure 3.4. First, using scikit-image [121], each mask is skeletonized. The skeletonization process can turn kinks in the original mask into dangling ends that distort the original geometry (see Figures 3.4a-3.4b). To circumvent this problem, the skeleton is converted into a region adjacency graph (RAG) in which adjacent pixels are treated as connected nodes. By finding the shortest path connecting the periphery[1] we can not only eliminate any fictitious dangling branches but also get an ordered list of the pixels making up the segment. A subset of these pixels are selected and used as the points of a linestring[2] which serves as a simplified, 1-dimensional representation of the nanowire.

Each linestring then becomes a node in a multigraph (a graph in which multiple edges can exist between the same pair of nodes) and edges between nodes occur wherever distinct linestrings cross. A multigraph is necessary because real nanowires can curve and therefore can intersect more than once as opposed to the straight rods that are usually used in simulations. Using the nominal diameter of the nanowires

[1] In some graph $G = (N, E)$, let $d(s, t)$ be the length of the shortest path between nodes $s, t \in N$. The *periphery* of G is the pair of nodes $\{s, t\}$ for which $d(s, t)$ takes its maximum value.

[2] A sequence of points and the line segments connecting them

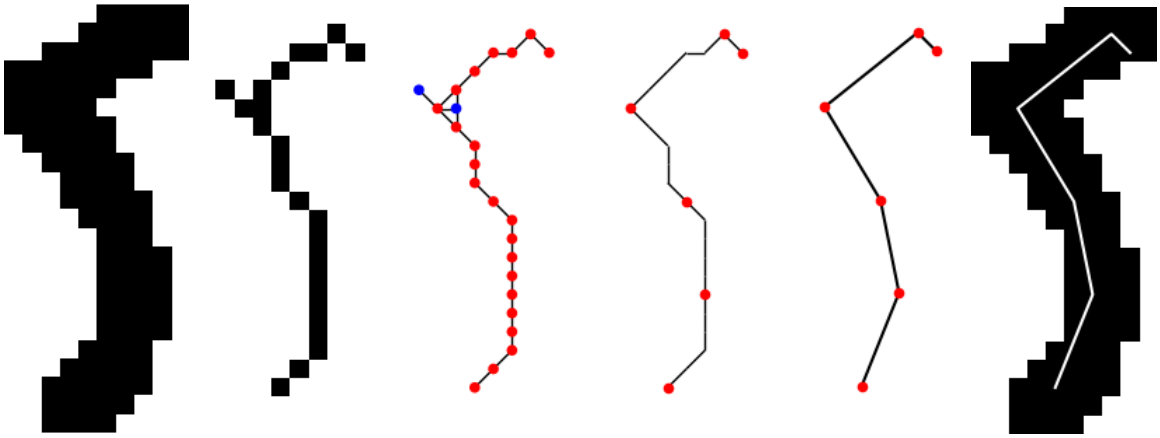

(a) Original mask (b) Skeleton (c) RAG (d) Anchors (e) Simplified linestring (f) Simplified linestring over original mask

Figure 3.4: Illustration of the conversion of a manual trace to 1-dimensional curve. (3.4a) the original, manually traced wire mask. (3.4b) the skeleton of the wire mask. (3.4c) the region adjacency graph (RAG) made from the skeleton. The nodes connecting the periphery (see footnote 1 on page 69) are shown in red and other nodes in blue. (3.4d) a subset of the nodes on the peripheral path used to simplify the shape. (3.4e) the simplified shape of the nanowire. (3.4f) simplified shape superimposed on the original mask to demonstrate that the original geometry has been faithfully preserved.

(120 nm) we can subdivide our linestrings and assign internal resistances as edges where appropriate - we use the same scheme detailed in [87, 116] and calculate internal resistivities (including the effects of surface scattering) according to [13]. This process ensures that our model can now be described as a graph rather than a multigraph because the way in which we assign internal resistances guarantees that no two segments will cross more than once. We assume that all contacts between nanowires have the same resistance and find this value by requiring that the calculated series resistance of each computerized network matches the measured series resistance of the corresponding physical network. This is done by decomposing the series resistance R_s into the sum of contributions from internal resistance α and contact resistances at nanowire contacts βR_c:

$$R_s = \alpha + \beta R_c \tag{3.2}$$

where α, β are unique to the individual network and R_c is the per contact resistance chosen for the simulated network. Varying the chosen value of R_c and solving the simulated circuit allows us to extrapolate values of α, β and solve for the R_c that produces the experimentally measured R_s [84].

In general, we identify failures by examining each nanowire in the images before and after the voltage ramp. In one case, sample 2B-11, the pre-ramp images were lost. To compensate for this, we developed explicit criteria to identify failed segments that function for both complete and incomplete image data. The complexity of these rules demonstrates the difficulty in this undertaking: the details we seek to observe are very small and image noise or unclean samples can greatly hamper analysis. To explain our criteria clearly, it is useful to define a set of symbolic logical functions that take a region x as argument and return True or False depending on whether the associated statement is true or false of x. Using these definitions, stated in Table 3.1, we can write our logical failure function $F(x)$ in Equation 3.3. When $F(x)$ is True,

$A(x)$	=	In the pre-ramp images, $\geq 95\%$ confidence that the nanowires in region x are clearly intact. If there are no pre-ramp images, this is False.
$B(x)$	=	In the pre-ramp images, the nanowires in region x have some imaging artifacts but $\geq 75\%$ confidence that they are intact. If there are no pre-ramp images, this is False.
$C(x)$	=	In the post-ramp images, there are no visible nanowires in region x.
$D(x)$	=	In the post-ramp images, the regions surrounding x contain a mix of intact and failed nanowires indicating that any failed segments failed from joule heating and not from the laser scribing.
$E(x)$	=	In the post-ramp images, region x contains multiple regularly spaced spheroidized silver particles on a path connecting parallel tips of nearby nanowire segments. If pre-ramp images exist, they must show this region as intact.
$F(x)$	=	Region x has failed.

Table 3.1: Logical functions used to define failure criteria

Batch	Sample	R_s [Ω]	R_c [Ω]	Density	Area [µm^2]
2BM	03	6.40e+03	6.36e+04	5.09	2.55e+04
	05	8.24e+02	5.06e+03	6.38	1.92e+04
	11	2.90e+03	3.69e+04	7.27	2.02e+04
3B	01	2.69e+01	2.45e+01	8.12	5.95e+03

Table 3.2: R_s is the measured two-probe resistance. R_c is the imputed average effective contact resistance. The density is expressed as a multiple of the percolation threshold assuming that wires are 40 µm long.

region x has failed, and when $F(x)$ is False, region x is intact.

$$F(x) = \Big(A(x) \text{ and } C(x)\Big) \text{ or } \Big(B(x) \text{ and } C(x) \text{ and } D(x)\Big) \text{ or } \Big(C(x) \text{ and } D(x) \text{ and } E(x)\Big) \tag{3.3}$$

Failed regions are marked manually with a stylus on an iPad. Regions identifying failed segments and failed contacts are annotated separately. With the digital network thus constructed and failures identified, we proceed to statistical and graph theoretic analyses to elucidate failure dynamics.

Out of 28 of fabricated samples, 19 proved to be percolating. Of these 19 percolating samples, only 5 had density and image quality suitable for analysis. Of these 5 suitable samples, one yielded an imputed value of $R_c < 0$ which suggests the presence of a non-visible short rendering this network inappropriate for analysis. Table 3.2 shows the properties of the remaining four networks before the voltage ramp. The first thing to notice in Table 3.2 is that the imputed average effective contact resistance, R_c, of 3B-01 is at least two orders of magnitude smaller than all values of R_c from batch 2BM. We attribute this to differences in the quality of contacts between nanowires and the electrode pads. In batch 3B, the laser was slightly defocused; this destroyed percolation by causing many of the nanowires to spheroidize but it also likely optimized the contacts between the remaining nanowires and the evaporated silver electrodes. Therefore when the second dose of nanowires was deposited, they

could make good electrical contacts with the preexisting nanowires which already had good electrical contacts with the electrodes. The defocusing of the laser also explains why sample 3B-01 is roughly one quarter the area of the samples from batch 2BM (the size of the beam determines the size of the channels between samples and larger channels means smaller samples).

The failures identified in our four samples are listed in Table 3.3 for both nanowire segments and contacts between nanowire segments. In all cases, the identified failures were not nearly sufficient to cause the observed total network failure. This shows that a substantial number of destroyed circuit elements are not identifiable in the SEM images. There are several possible explanations for this. First, we know that failure occurs preferentially at the contacts between wires [87]. The 3D nature of the sample, with nanowires tending to touch either on top of or beneath each other, could make these failures very hard to see. At the contact between two nanowires, it would be possible for the bottom wire to disconnect only in the region directly below the top wire while the top nanowire remains largely unchanged. This change, although it would increase the system's total resistance, would be undetectable via SEM imaging. It is also possible for a nanowire to undergo only partial morphological evolution that results in the formation of a narrow neck. If the neck is sufficiently small, this could be undetectable or appear as noise in an SEM image even though it might effectively zero out conduction through the neck.

The small number of identified failures, especially the very small number of identifiable failed contacts, requires merging the data from all samples to obtain meaningful statistics. However, as mentioned before, many centrality measures are ill suited to be compared between different networks. Therefore we scale all attributes of interest such that, on each network, each attribute's maximum value is 1 and minimum value is 0.

In our previous analysis of various measures of node importance, we have con-

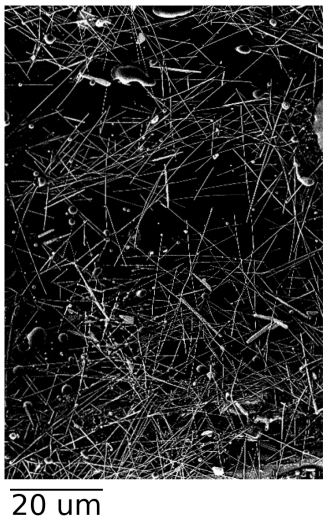

(a) Before voltage ramp

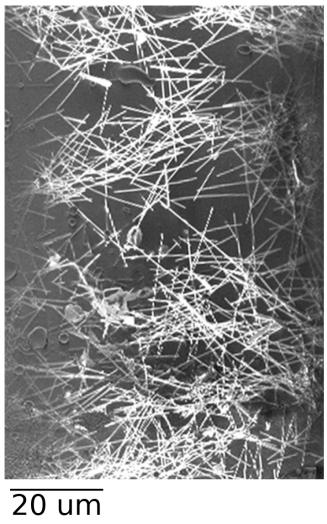

(b) After voltage ramp

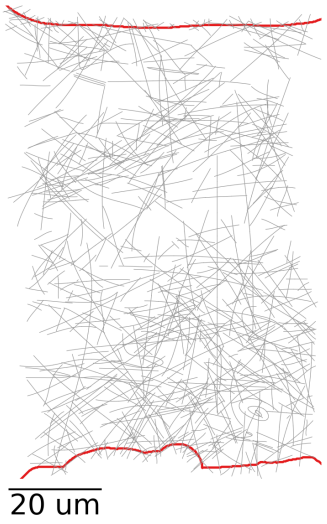

(c) Extracted geometry

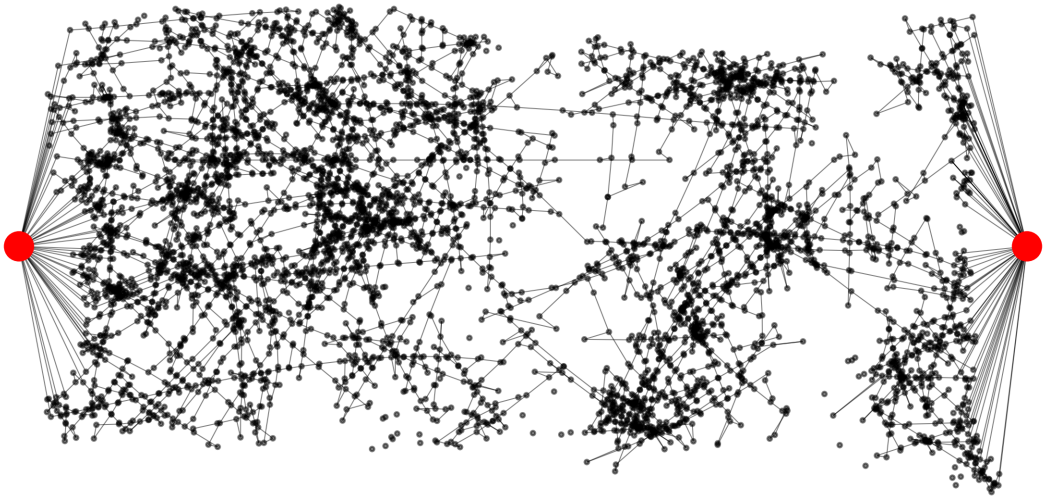

(d) Equivalent graph

Figure 3.5: Sample 3B-01 during various steps of testing and analysis. Figures 3.5a,3.5b show the sample before and after the voltage ramp, respectively. Figure 3.5c shows the geometric objects extracted from the before and after ramp images. Figure 3.5d shows the graph corresponding to the network before the ramp. Positions in 3.5d roughly correspond to the positions in 3.5c when rotated 90° clockwise.

Batch	Sample	Nanowire Segment Intact	Nanowire Segment Failed	Contact Intact	Contact Failed
2BM	03	10,944	82	5,678	24
	05	12,273	49	6,348	11
	11	16,084	31	8,310	7
3B	01	5,425	15	2,766	2
Total		44,726	177	23,102	44

Table 3.3: Number of visible failures of nanowire segments and inter-nanowire contacts. Note that each nanowire may be divided into multiple segments. A segment is marked as failed if any portion of it has failed.

sidered betweenness centrality and percolation centrality among many others. The self propagating nature of thermal cracks suggests that another measure of node importance known as *eigenvector centrality* [68] may be relevant to failure. We know that local failures cause current redirections which can in turn cause more failures. It is reasonable, then, to suppose that a nanowire node's tendency to fail depends on its neighbors' tendency to fail and the strength of the connection to each neighbor. Defining x_i to be the tendency of node i to fail, we can express this as

$$x_i = \frac{1}{\lambda} \sum_{j \in N} a_{ij} x_j \tag{3.4}$$

where λ^{-1} is a normalization constant and a_{ij} is the conductance between nanowires i and j. Note that, because the vast majority of pairs of wires do not intersect, the vast majority of conductances a_ij are zero. Rewriting equation 3.4 in matrix form and multiplying both sides by λ, the cause of the name eigenvector centrality becomes clear

$$\lambda \vec{\mathbf{x}} = \overleftrightarrow{\mathbf{A}} \vec{\mathbf{x}} \tag{3.5}$$

where $\overleftrightarrow{\mathbf{A}}$ is the matrix of elements a_{ij} (also known as the adjacency matrix for a graph with conductances as edge weights) and λ, which was previously called a normalization constant, can now be clearly identified as an eigenvalue. Note that, for

Equation 3.5 to be soluble, we must only consider strongly connected graphs. For our purposes, we only include the elements of the percolating cluster in A and we define the eigenvector centrality of all other nodes not in the percolating cluster to be zero. Equation 3.5 has many solutions. Given the requirement of strong connectivity, the matrix A is guaranteed to be irreducible which, by the Perron-Frobenius theorem [91, 36] ensures that the eigenvalue of largest magnitude will be real and have a corresponding eigenvector that can be chosen to have strictly positive components. The components of this strictly positive eigenvector are taken to be the eigenvector centrality values of the nodes in the graph.

For nanowire segments, the extracted values of betweenness centrality, percolation centrality, eigenvector centrality, current, and power are shown in Figure 3.6. We include values of current and power dissipated by joule heating to compare our graph theoretic tools against more conventional physical analysis. Nanowire segments correspond to nodes in a graph. Because power and current are ill-defined for a node, we take the node's power and current to be half the respective sums of power or current through adjacent resistors. The vertical axis on the left of Figure 3.6 details the attribute being calculated. The horizontal axis shows all values normalized such that, within a given sample, the minimum value of each attribute is 0 and the maximum value of each attribute is 1. The color coding, shown in the legend in the top right, distinguishes between values of failed vs. intact segment samples. The right side of each plot shows p and t values comparing the failed vs. intact sample means as calculated by Welch's t-test [125, 25, 26]. The p-value indicates the probability that the difference between intact and failed sample means is the result of pure chance. The t-value indicates the size of the difference between intact and failed sample means relative to the size of variation within each sample. Interpreting the top row of data in Figure 3.6, for example, we could say that the betweenness centrality of failed nanowire segments is greater than that of intact nanowire segments. The p-value, which is roughly 0.0005, indicates a very small probability that this difference in betweenness centrality arises from pure chance. This analysis of the

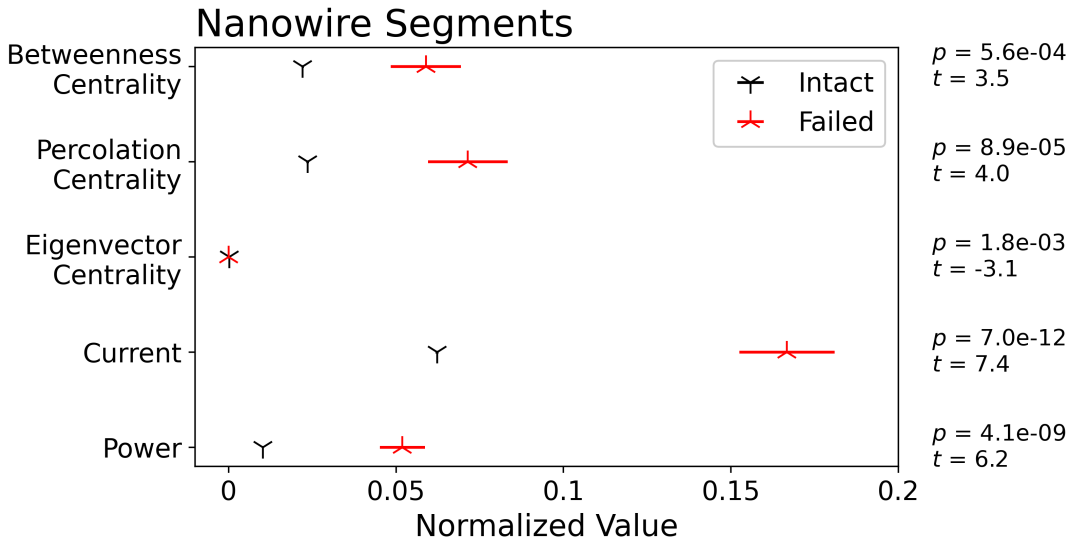

Figure 3.6: Mean attribute values for intact and failed nanowire segments. Vertical axis on left labels the attribute value being displayed in that row. Values on horizontal axis are normalized such that, for each attribute within each network, the minimum attribute value is 0 and the maximum is 1.

betweenness centrality of nanowire segments is consistent with our predictions: we expected high betweenness centrality nodes to be more likely to fail. The percolation centrality of nanowire segments shows a similar pattern: the mean value of percolation centrality on the failed sample is meaningfully higher than that of the intact sample. Furthermore, the t-value for percolation centrality is higher than that of betweenness centrality. Recall that percolation centrality weights paths by the voltage of the starting node. This suggests that including electrical information in our graph theoretic analysis may strengthen the ability of centrality-based measures to predict failure.

Eigenvector centrality, which is not derived from considerations of betweenness, requires special attention. The data from Figure 3.6 show reasonable with reasonable confidence ($p = 0.0018$) that low values of eigenvector centrality of nanowire segments are associated with higher probability of failure, but the miniscule size of most values give reason for caution. Recall that the eigenvector centrality of each node is calculated by finding the dominant eigenvector of the graph's adjacency matrix, as shown

in Equation 3.5. We perform this calculation in NetworkX [45], which uses power iteration. The procedure terminates when

$$||\vec{\mathbf{b}}_k - \vec{\mathbf{b}}_{k-1}|| \leq 10^{-6} \tag{3.6}$$

where $\vec{\mathbf{b}}_k$ s the approximate dominant eigenvector yielded by the k^{th} iteration. For our (unnormalized) eigenvector centrality values, though, there are only a total of 35 nanowire segments with eigenvector centrality greater than our tolerance of 10^{-6}. Of course, this tolerance is specified for the whole vector, not for individual components. To get a rough sense of the precision for individual components, we assume that this error will be evenly distributed over all components. If the eigenvector has N components, we would expect the per component precision Δb to satisfy

$$\sqrt{\sum_{i}^{N}(\Delta b)^2} = \sqrt{N(\Delta b)^2} \leq 10^{-6} \tag{3.7}$$

This inequality yields an approximate precision of $\Delta b \leq 10^{-6}/\sqrt{N}$ for each nodal value of eigenvector centrality. Calculating these approximate precisions for each sample, we find that each sample has only 12 nodes with eigenvector centralities that are greater than the per node precision of that sample. Values smaller than the precision should not be used for analysis. Therefore, while it is certainly possible that eigenvector centrality has something to say about failure of nanowire segments, we consider this data insufficient to imply any conclusion with confidence.

The current and power data for nanowire segments, shown in Figure 3.6, show an even stronger pattern than betweenness centrality and percolation centrality. The t-values for current and power are larger than those of the graph theoretic measures and the p-values for current and power are smaller than those for the graph theoretic measures. This suggests that, while our graph theoretic measures are applicable here, they may not be as descriptive as a more conventional circuit analysis.

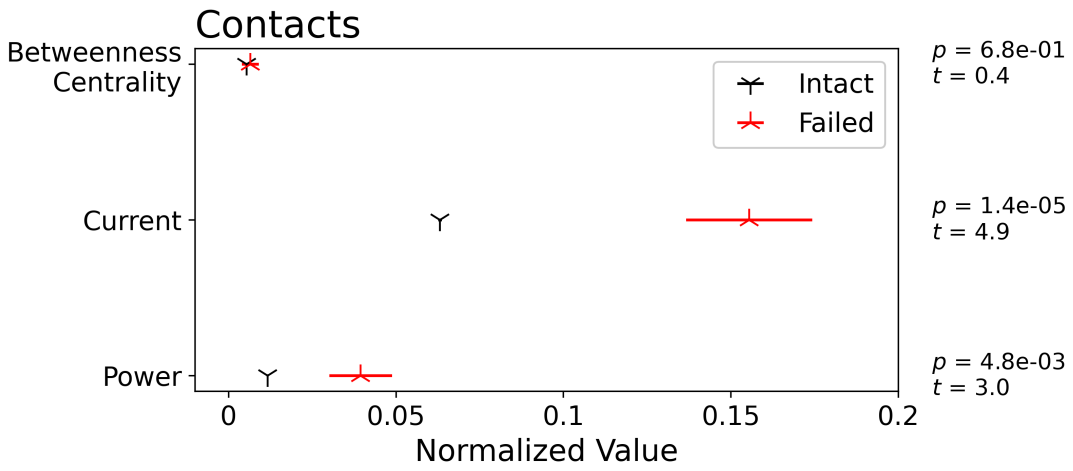

Figure 3.7: Mean attribute values for intact and failed contacts between nanowire segments. Vertical axis on left labels the attribute value being displayed in that row. Values on horizontal axis are normalized such that, for each attribute within each network, the minimum attribute value is 0 and the maximum is 1.

For contacts between nanowire segments, the extracted values of betweenness centrality, current, and power are shown in Figure 3.7. Contacts are represented as edges in our graph. Calculating the betweenness centrality of an edge is identical to calculating the betweenness centrality of node, except that we consider whether shortest paths traverse a given edge rather than a given node. The definition of node v's betweenness centrality, shown in Equation 2.3, could be modified to describe the betweenness centrality of some edge e by simply making the substitution $v \rightarrow e$, as shown in the equation below.

$$C_B(e) = \sum_{s,t \in N} \delta_{st}(e) \tag{3.8}$$

The betweenness centrality of edge e is obtained by summing, for all possible source and target nodes s and t, the fraction of shortest paths from s to t that pass through edge e. Figure 3.7 does not include percolation centrality or eigenvector centrality because these are not defined for edges. The axes and normalization conventions of Figure 3.7 are otherwise identical to those of Figure 3.6.

The betweenness centrality of failed vs intact contacts have $p = 0.68$ and $t = 0.4$. The t-value being less than one is particularly important: this indicates that the dif-

ference between these means is smaller than the variation within each sample. This renders the betweenness centrality of failed and intact contacts statistically indistinguishable. This is marked departure from the results for segments where betweenness centrality and percolation centrality both had statistically significant differences in means between failed and intact samples. The results for current and power in contacts, on the other hand, mirror those for segments: the current and power through failed contacts are statistically significantly larger than the current through intact contacts, although the case is stronger for current ($p = 1.4 \times 10^{-5}$) than it is for power ($p = 4.8 \times 10^{-3}$). This cements the observation made regarding the nanowire segment data shown in Figure 3.6: while the betweenness-based graph theoretic measures we have tested do appear to be connected to failure, they do not perform as well as conventional physical analysis.

The final point to make with respect to Figures 3.6-3.7 is that, for both nanowire segments and contacts, the t-values for current are greater than the t-values for power. This suggests that current may be a better predictor of failure than power. To test this, we will perform a logistic regression on current and power for both nanowire segments and contacts.

Logistic regression is a technique used to map from numerical values to binary categorical outcomes. We begin by assuming that probability of failure for a single network element is given by

$$p = \frac{1}{1 + \exp\left[-\vec{\mathbf{B}} \cdot \vec{\mathbf{x}}\right]} \tag{3.9}$$

where $\vec{\mathbf{B}}$ is a vector of coefficients and $\vec{\mathbf{x}}$ is a vector of the network element's attribute values. If the component B_i is positive, this indicates that p increases as attribute x_i increases. If the component B_i is *negative*, this indicates that p decreases as x_i increases. Note that we can also write p as a function of a binary variable y which

equals 1 for failure and 0 for remaining intact.

$$p(y\,|\vec{\mathbf{x}}) = \frac{y}{1+\exp\left[-\vec{\mathbf{B}}\cdot\vec{\mathbf{x}}\right]} + \frac{1-y}{1+\exp\left[-\vec{\mathbf{B}}\cdot\vec{\mathbf{x}}\right]} \tag{3.10}$$

We define $\vec{\mathbf{x}}_i$ to be the attributes (current and power) of network component i. We define y_i to be the status (failed = 0, intact = 1) of network component i. We obtain the values of the coefficients $\vec{\mathbf{B}}$ by maximizing the likelihood L shown in Equation 3.11.

$$L\left(\{\vec{\mathbf{x}}_i\},\{y_i\}\right) = \prod_i p(y_i\,|\,\vec{\mathbf{x}}_i) \tag{3.11}$$

In practice, this optimization is usually done on the (negative) log-likelihood since this converts a product into a sum and thereby greatly simplifies calculations.

We perform separate regressions for nanowire segments and for contacts. Before discussing the extracted coefficient values, it behooves us to discuss the performance of these regressors. We show confusion matrices in Figure 3.8 as a measure of this performance. The horizontal axes in the confusion matrices show the label predicted by the regression. The vertical axes show the true label (label observed in images). Each matrix has four quadrants. Starting in the upper left corner and moving clockwise, these quantrants are: correctly labeled as intact, incorrectly labeled as failed, correctly labeled as failed, and incorrectly labeled as intact. The number in each quadrant corresponds to the number of elements in that category. The 177 in the bottom left of the nanowire segments confusion matrix indicates that the regressor looked at the attributes of 177 failed segments and erroneously predicted they would remain intact. Out of 44 failed contacts, our regressor predicted zero failures of any kind. This is a result of a gargantuan class imbalance: there are at least 250 times more intact network components than failed network components. This biases the model to predict that most elements will remain intact. In fact, the model can achieve a very high likelihood by treating failure probability as strictly zero. Taken together,

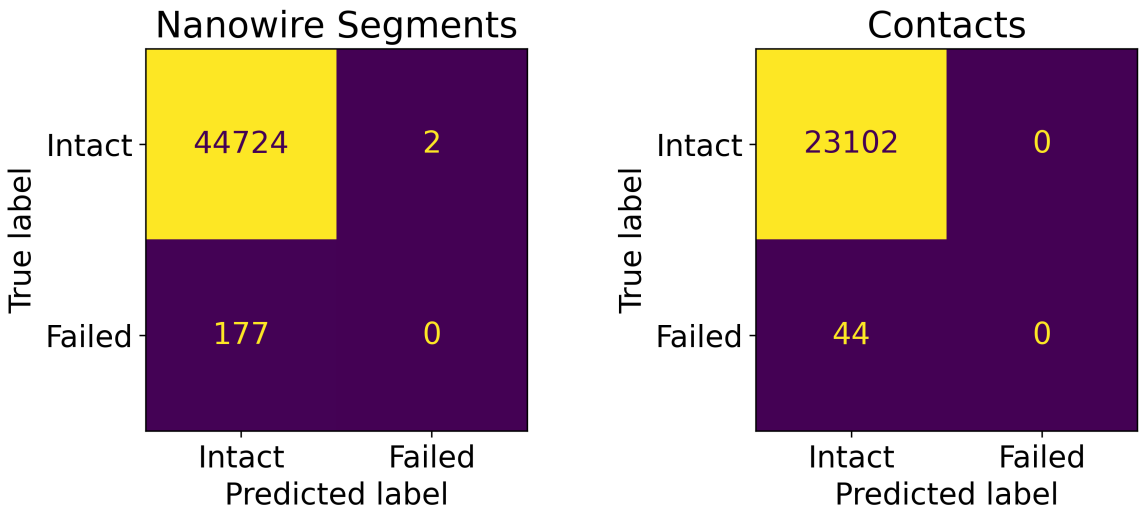

Figure 3.8: Confusion matrices for logistic regressions performed separately on nanowire segment data and contact data.

		Nanowire Segments	Contacts
Coefficients	Current	3.5	18
	Power	3.3	-25
Likelihoods	L_{fit}	0.98	0.99
	L_{null}	0.97	0.99

Table 3.4: Regression coefficients and likelihoods for a logistic regression to predict failures. Failed components are class 1 and intact components are class 0 so positive coefficients indicate that high values of the listed attribute increase probability of failure. L_{fit} is the likelihood of the best fit and L_{null} is the likelihood of the null hypothesis (that there is a single, constant failure probability).

these factors mean that our regressions are *not* predictive, but the extracted coefficients can absolutely still show trends and patterns.

Coefficients and likelihoods for our logistic regression are shown in Table 3.4. Note that the likelihoods of our fits are very close to the likelihoods of the null hypotheses because of the aforementioned class imbalance. Recall that a positive coefficient means that an increase in the corresponding attribute value will increase the probability of failure. For nanowire segments, current and power have coefficients of 3.5 and 3.3 respectively. This is consistent with our understanding of failure as discussed

in Figure 3.1. Power drives high temperatures which accelerates both spheroidization and electromigration by increasing surface diffusivity. Further, power is ultimately driven by current so, while current is the primary driver electromigration, it also has an impact on spheroidization. For the contacts between nanowire segments, current appears to increase failure probability while power *decreases* failure probability. This result is somewhat surprising given the highly coupled nature of current and power. We must, however, be cautious about over-interpreting the results of this analysis. We performed our logistic regression using Scikit-Learn [90] with neither regularization nor class weighting, but statistical models can be quite sensitive to these types of parameters that are chosen by the user. If the opposing signs of the current and power coefficients are the result of a statistical fluke, we should not infer anything from them. To ensure that these results show a meaningful trend, we have performed our regression with a few other sets of input parameters (regularization and/or class weighting) and have shown the results in Appendix A.6. In two out of the three new test cases, the current and power coefficients for contacts still have opposite signs. In the third new test case, the current coefficient for contacts is 2.5 while the power coefficient for contacts is 0.36. While this last regression does not support the conclusion that joule heating protects contacts, this regression and all others still strongly support the argument that current is much more important in causing contact failure than is power. One alternate explanation of this pattern is that we are simply observing the effect that high temperatures have on un-optimized contacts in our network.

Figure 3.9 shows the time evolution of the resistance of our four samples during their voltage ramps. Recall that thermal annealing is a common step in the fabrication of nanowire networks. The thermal annealing step sinters contacts between nanowires and thereby increases their conductance by several orders of magnitude. This process is often referred to as junction optimization. With this in mind, we have grouped the samples into two categories. The samples on left (Figure 3.9a) begin at some finite resistance and then have their resistance slowly increase before it diverges. This resistance evolution is consistent with these networks having most of their inter-

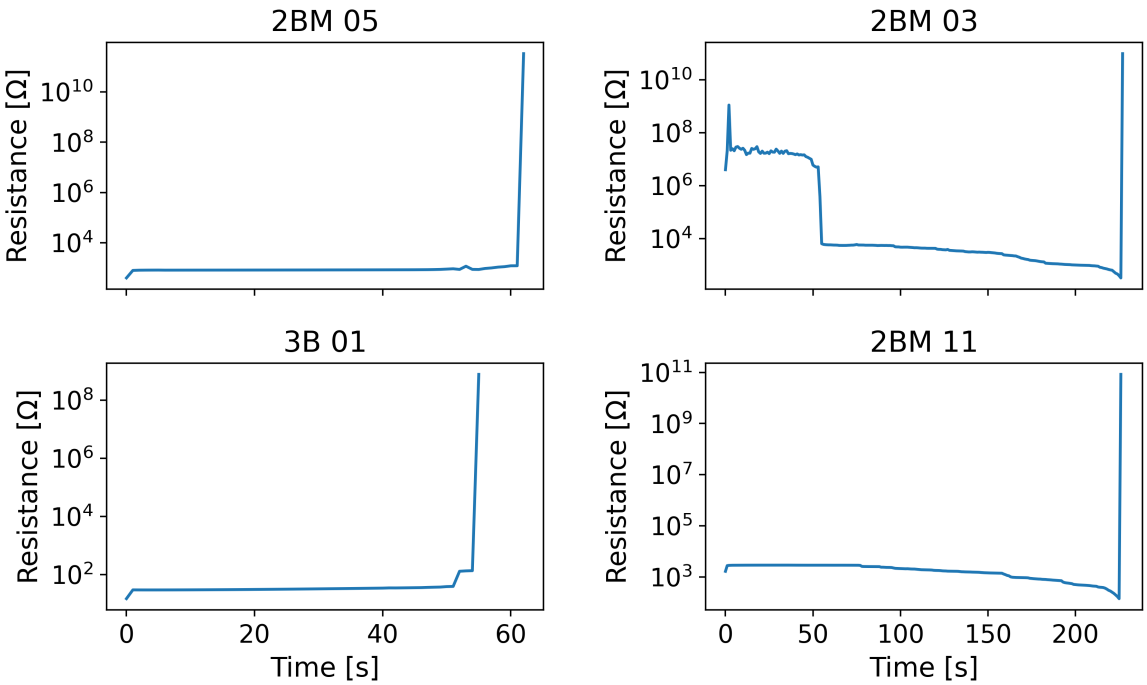

(a) Samples in which contacts were optimized before ramp

(b) Samples in which contacts are optimizing during ramp

Figure 3.9: Time evolution of resistance for each sample. Voltage is ramped at rate of 1 V per minute until resistance explodes.

		Nanowire Segments	Contacts
Pre-Optimized Coefficients	Current	3.8	31
	Power	0.41	-47
Optimizing Coefficients	Current	4.3	14
	Power	4.2	-19

Table 3.5: Results of logistic regression on pre-optimized samples (from Fig. 3.9a) and optimizing samples (from Fig. 3.9b).

nanowire contacts already optimized before the voltage ramp begins. This means that resistance changes are primarily driven by failures. The samples on the right (Figure 3.9b) begin at some finite resistance and then see their resistance slowly decrease until it suddenly reverses and diverges. This resistance evolution is consistent with these networks having inter-nanowire contacts optimize *during* the voltage ramp. It is entirely possible that network elements are being destroyed during the ramp as well but, because the total resistance is decreasing, the contact optimization is clearly the dominant effect. Eventually, though, an avalanch of failure occurs and the resistance diverges. It is possible that the regression coefficients for contacts in Table 3.4, which suggest current driving failure and power preventing failure, are being biased by the contact optimization occurring in Figure 3.9b. To account for this, we now perform separate regressions on the pre-optimized (2BM 05, 3B 01) and optimizing (2BM 03, 2BM 11) samples.

The results of these regressions are shown in Table 3.5. For both the pre-optimized and optimizing contacts, current has a positive coefficient and power has a negative coefficient. Surprisingly, the data from the samples that were optimizing during the ramp was not biasing the power coefficient to be more negative - in fact the opposite is true. The power coefficient for the optimizing samples is actually greater than the one for the pre-optimized samples. The trend we observe with current appearing to increase failure probability while power appears to decrease failure probability is therefore certainly not a result of junction optimization that occurs during the voltage ramp.

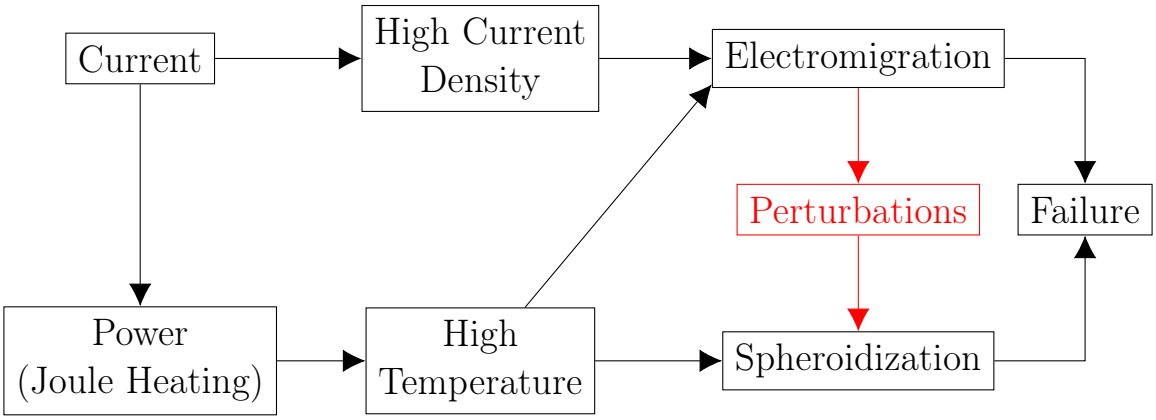

Figure 3.10: A causal graph showing the drivers and mechanisms of silver nanowire failure under typical operating conditions.

In understanding the implications of the results of this regression, it is useful to refer to the causal graph of failure discussed earlier in this chapter. For the convenience of the reader, we show another copy of this diagram in Figure 3.10. Note that this copy has a small addition, shown in red. The evidence we have accumulated suggests that current tends to drive contact failure while power appears to delay or prevent it. The most direct result of power dissipation via joule heating is high temperatures, as we see in Figure 3.10. Taken together, these factors suggest that high temperatures, much like power, decrease contact failure probability. Therefore, we infer that the dominant pathway to contact failure be the top branch of Figure 3.10: Current $\rightarrow$ High Current Density $\rightarrow$ Electromigration $\rightarrow$ Failure. In other words, electromigration appears to dominate over spheroidization when it comes to the failure of contacts between silver nanowires. All that said, the experimental observations [87] tend to show visible evidence of spheroidization in failed networks. Contacts between nanowires make up a very small portion of the area of a given silver nanowire network. It is therefore possible that silver nanowire segments fail from spheroidization while contacts fail from electromigration but, because of the size disparity between the two, only the spheroidization is observed in post-failure imaging. There is, however, another explanation that unifies our analysis with the existing literature. As depicted

in red in Figure 3.10, electromigration could very well provide a crucial source of the kinetic perturbations that initiate the process of spheroidization of contacts.

These results do not paint a particularly clear picture of the failure of silver nanowire *segments* (as opposed to contacts). Depending on the regression parameters, either power or current may appear more important. The picture for contacts, however, is very clear. At the very least, electromigration appears to far and away dominate over spheroidization in the failure of contacts and there is strong but less conclusive evidence that joule heating may actually protect against failure. Our results therefore indicate that the key to protecting against silver nanowire contact failure is preventing electromigration. Given that silver nanowire network failure is driven by contact failure, we should therefore also view preventing contact electromigration as priority one in bringing these exciting materials closer to market.

3.1 Conclusions

We have created high fidelity *in silico* models of real silver nanowire networks and used these models to elucidate failure dynamics. But the difficulty of identifying failed network components in SEM images, and the resulting mammoth class imbalance, make it challenging to precisely predict exactly which network elements will fail. Nonetheless, this analysis bears much useful fruit. First, our methodology for image extraction will be useful to other scientists studying collections of tubular structures and, in particular, the RAG-based technique demonstrated in Figure 3.4 is an elegant solution to the well known false branch problem of many skeletonization methods, albeit with the caveat that it only works on structures with no true branches. Second, we conclude that graph theoretic considerations alone appear to provide relatively little new information about silver nanowire network failure dynamics. Graph theoretic measures perform better the more physical information they include, but do not offer any understanding beyond that provided by more traditional examinations of current and joule heating. It was demonstrateed in [132] that, for single silver nanowires in

vacuum under electrical bias, electromigration is far and away the dominant failure mechanism. Our analysis suggests extends and modifies these results to contacts between silver nanowires in networks operating under ambient conditions. We show that, in a silver nanowire network under electrical bias, the failure of contacts between nanowire segments is driven primarily by electromigration - either directly (ionic dislocations causing necking and eventual disconnection) or indirectly (ionic dislocations providing the kinetic perturbations to initiate spheroidization). Further, the junction data suggest that joule heating may tend to protect junctions rather than degrade them. These last points illustrate the importance of combining experimental and computational analysis. In experiments, it is well documented that an un-optimized network can see significant conductivity gains by simply applying an electrical bias and letting joule heating sinter network junctions [102]. But only by combining experimental measurements and high quality simulations of those measurements can we reveal surprising behavior such as electromigration inducing spheroidization or thermally activated junction protection The fact that temperature can mediate both optimization and destruction means that, in future analysis, we must capture both effects to accurately describe the failure dynamics. In conclusion, this work has developed novel methods for digitizing real nanowire networks, provided a unique dataset to the nanomaterial engineering community, and extended some of our understanding of the failure of isolated silver nanowires in vacuum to networks of silver nanowires under ambient conditions.

Chapter 4

From Images to Non-Planar Graphs

In our previous analysis, we treat nanowires as though they all have equal diameters. In reality the diameters of these nanowires are variable and may have significant impacts on both local resistances and current densities. Consider a nanowire of fixed length L with a fixed potential difference V between its ends. The current density through the nanowire is

$$J = \frac{V}{RA} = \frac{VA}{\frac{\rho L}{A}A} = \frac{1}{\rho}\frac{V}{L} \tag{4.1}$$

where A is the nanowire's cross-sectional area. Thus we have that $J \propto \frac{1}{\rho}$ where V/L fixes the constant of proportionality. Using the resistivity results from [13] and assuming a fixed ratio V/L, we have plotted the diameter dependence of $1/\rho$ and therefore of J in Figure 4.1. The data in Figure 4.1 show that differing wire diameters can can yield meaningfully different current densities, an effect which is amplified by the nonuniform distribution of current in real conductors.

The logical next step in solidifying our conclusions about the relative importance of electromigration and spheroidization is therefore to include diameter information in our analysis, but this information does not come cheaply. Developing automated ways of accessing local diameter information is the subject of this final chapter of the thesis.

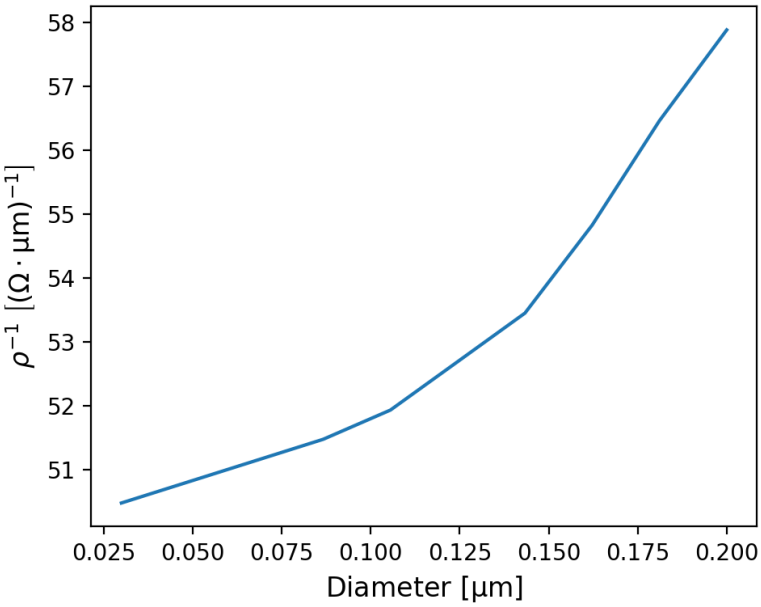

Figure 4.1: Plot of reciprocal of resistivity ($1/\rho$) as a function of diameter. To calculate a numerical value of current density J for a given nanowire one would multiply y axis values by the voltage V between nanowire tips and divide by the length L of the nanowire in µm.

The ideal process for analyzing our networks in a diameter depdendent way is substantially similar to the process outlined in Chapter 3, except our masks must highlight all or most of the pixels that make up each nanowire instead of simply capturing the general shape. One can then extract diameter information from these pixel maps relatively easily, for instance using a euclidean distance transform as done in [35]. This segmentation is significantly more tedious than our previous method if done manually. We proceed with a brief discussion of existing automatic image segmentation techniques and their drawbacks. This discussion also motivated our decision to use a semi-manual segmentation in the analysis of Chapter 3.

One of the best known tools for turning images into graphs is NEFI (Network Extraction from Images) [27]. This software library is designed to be an end to end solution; it can perform preprocessing, filtering, segmentation, and junction detection. NEFI would be ideal for our use case but for one requirement: NEFI only works on planar graphs. A planar graph is a graph which, if embedded in a 2D plane with

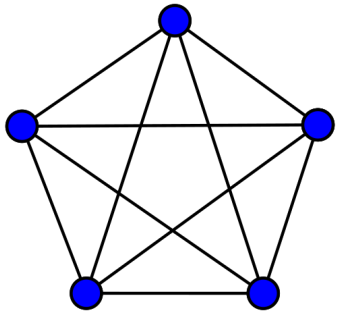

(a) The complete Kuratowski graph K_5

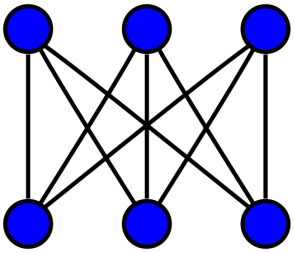

(b) The complete bipartite Kuratowski graph $K_{3,3}$

Figure 4.2: Kuratowski subgraphs

nodes as points and edges as lines connecting those points, can be drawn such that edges only cross at nodes. More formally, a graph can be said to be planar if and only if it does not contain a subgraph that is a subdivision of the complete graph with 5 nodes K_5 or the complete bipartite graph with 6 nodes $K_{3,3}$, both shown in Figure 4.2. This result is known as Kuratowski's theorem [65] and these subgraphs are known as Kuratowski subgraphs after the first mathematician to publish the proof. Because a graph only needs to contain a single Kuratowski subgraph subdivision to be nonplanar, the probability of a graph being planar must decrease as the number of nodes increases. To examine this in the context of our nanowire networks, we can consider the graphs of nanowire networks without worrying about adding internal resistance because the graph of a nanowire network with internal resistances is a subdivision of the graph of a nanowire network without internal resistances. In a simulation of 10,000 small nanowire networks with anywhere from 36-94 nanowires, only 200 proved to be planar (a planarity rate of 2%). Therefore, because the nanowire networks examined in Chapter 3 contain 10-100 times more nanowires and nodes, there is a very small chance that these networks are also planar. More generally, any image processing routine that relies on planarity can be expected to fail much of the time in extracting a graph from an image of a nanowire network.

An alternative strategy relies on recent advances in artificial neural networks to perform image segmentation. Segmentation, in this context, is the term of art for

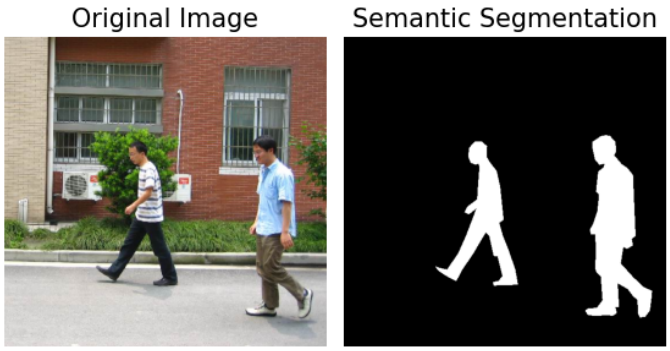

(a) Original image (left) and semantic segmentation (center). White pixels in semantic segmentation are labeled as "person" and black pixels are the background.

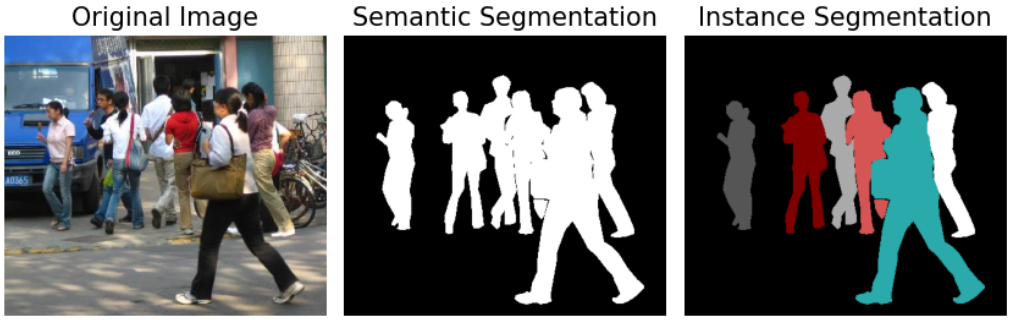

(b) Original image (left), semantic segmentation (center), and instance segmentation (right). Note that in the semantic segmentation there is a large mass of undifferentiated pixels all simply labeled as "person" whereas in the instance segmentation people are distinguished from the background *and* distinguished from each other.

Figure 4.3: Images from PennFudan dataset [123]

mapping each pixel in an image to a label. Semantic segmentation maps each pixel in an image to a class label. For example, suppose we are training a binary classifier to identify which pixels in an image are part of a person. A semantic segmentation is shown in Figure 4.3a. The color white indicates that given pixel has been assigned the label "person" and the black color denotes everything that is not a person. In a simple image with an uncrowded visual field, this semantic segmentation conveys all the information we could plausibly want about the scene. If, however, we consider a more visually crowded scene, such as the images in Figure 4.3b, we can see the limits of semantic segmentation. While the semantic segmentation of Figure 4.3b does successfully identify which pixels come from people and which pixels come from other objects, there is a large undifferentiated mass of pixels in the center of the image cor-

responding to multiple different overlapping people. Instance segmentation, shown in the third panel of Figure 4.3b, successfully identifies people in the image and then also distinguishes people from each other. Thus instance segmentation is a strictly harder task than semantic segmentation because instance segmentation requires accurate semantic segmentation and then adds additional computation on top of it.

Experimental images of nanowire networks are much more like the visually crowded images of Figure 4.3b than the simpler images of Figure 4.3a: we have a large number of overlapping and partially obscured nanowires. In order to extract a graph from a nanowire image, individual nanowires must be distinguished from each other. Therefore the task at hand calls for instance segmentation. The current gold standard in instance segmentation is MaskRCNN (Mask Region Convolutional Neural Network) [46]. As the image is fed through MaskRCNN, multiple rectangular regions of interest (ROIs) are proposed. The final step of the network is prediction of a mask for each possible class in each ROI and the parallel and decoupled prediction of the most likely class for the ROI. Then, only the mask of the most likely class is returned. SEM images of nanowire networks have several attributes that challenge this architecture. First, nanowires are long and thin and therefore occupy a small poportion of the area in any given image. In the correct ROI for a given nanowire, the pixels of that nanowire contribute very little information to be used in the segmentation masking [35]. Finally, SEM images of nanowire networks tend to be quite crowded with many nanowires overlapping in nontrivial ways. In our particular case, we must add the difficulty that our nanowire images have significant imaging artifacts and large amounts of particulates on the samples. Extensions of MaskRCNN such as FibeRCNN [35] have been proposed to predict keypoints and widths of nanowire segments. Accurate keypoint and width information would be sufficient for us to reconstruct equivalent circuits of our network in a fully automated way, but FibeRCNN, while showing great promise in segmenation of images containing separated fibers, does not perform well in the analysis of densely overlapping fibers. The most serious problem, though, is that training these models requires a significant quantity of correctly annotated im-

ages which does not currently exist.

We propose and test a novel preprocessing routine that adds an extra channel of local angle information to binarized grayscale images in the hopes that this technique will allow existing algorithms to properly identify and distinguish tubelike structures in a crowded visual field with a high degree of overlap. The first step in this process is binarization (also known as thresholding) in which each pixel in the image is assigned either 0 (background) or 1 (foreground). While the results of the local angle detection certainly depend on the output of this thresholding, the local angle detection algorithm is independent of the choice of thresholding algorithm. Therefore, as there is already significant literature discussing the merits of different thresholding techniques (see [107] for example), we will not compare multiple thresholding techniques and instead will simply state the thresholding method used where appropriate. We now proceed to a discussion of the algorithm for local angle detection.

The algorithm we devise is quite similar to the well known Radon Transform[97] which is used in modern tomographical imaging. The Radon Transform begins by describing a grayscale image's brightness f as a function of position x, y. We use the convention that a purely black region has $f(x, y) = 0$ and a purely white region has $f(x, y) = 1$ but other choices are possible. Define $l_{\phi,s}$ to be a line with distance s from a chosen origin and with a normal vector that makes an angle ϕ when measured counterclockwise from the x-axis. We define our radon transform g as the line integral of $f(x, y)$ along the line $l_{\phi,s}$

$$g(\phi, s) = \int_{l_{\phi,s}} f(x, y)\, \mathrm{d}l_{\phi,s} \tag{4.2}$$

This operation transforms our function f from the two dimensional space defined by x, y to a new two dimensional space defined by ϕ, s. We can evaluate g at many values of ϕ and s obtain a new image as shown in Figure 4.4.

Using many of the same concepts, we can define a new algorithm that assigns

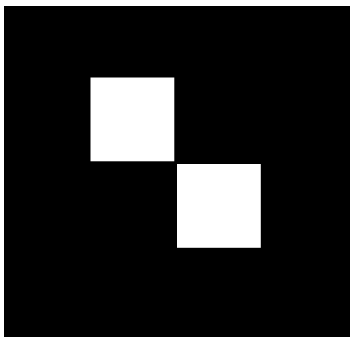

(a) Original Image $f(x, y)$

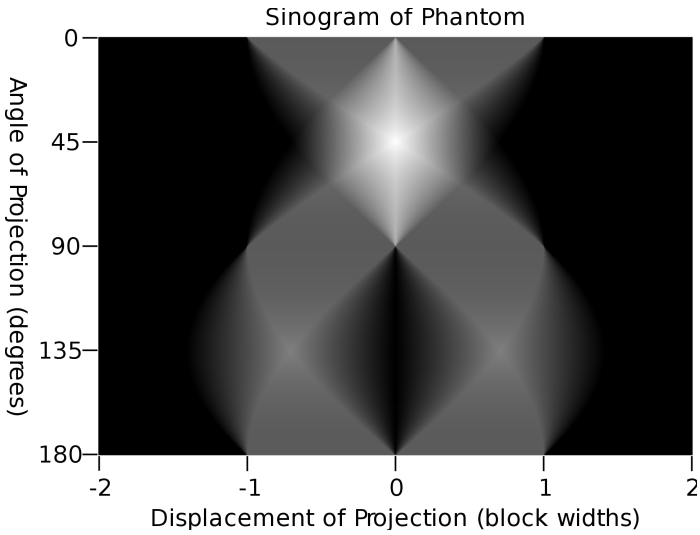

(b) Radon Transform $g(\phi, s)$ with s on the horizontal axis and ϕ on the vertical axis

Figure 4.4: Demonstration of the Radon Transform. In 4.4a the brightness represents values of the function $f(x, y)$ and in 4.4b the brightness represents values of the function $g(\phi, s)$. Images taken from Wikipedia.

some angle θ to each point (x, y). We call this algorithm the Radon Local Angle Transform. Once again, we define $f(x, y)$ to be image brightness at position x, y but we now require that the function f returns only 0 or 1. We will use the same parameterization of lines so that $l_{\phi,s}$ is a line with distance s from the origin and making an angle ϕ with the x axis. We now reparametrize the line integral from Equation 4.2 in terms of t with $x(t) = x_0 - t\sin\phi$ and $y(t) = y_0 + t\cos\phi$ where x_0, y_0 denote some chosen reference point on the line $l_{\phi,s}$. With this parametrization we can write

$$\int_{l_{\phi,s}} f(x,y)\,\mathrm{d}l_{\phi,s} = \int_{-\infty}^{\infty} f\left(x(t),\, y(t)\right)\sqrt{\left(\frac{\mathrm{d}x}{\mathrm{d}t}\right)^2 + \left(\frac{\mathrm{d}y}{\mathrm{d}t}\right)^2}\,\mathrm{d}t \tag{4.3}$$

$$= \int_{-\infty}^{\infty} f(x_0 - t\sin\phi, y_0 + t\cos\phi)\sqrt{\sin^2\phi + \cos^2\phi}\,\mathrm{d}t \tag{4.4}$$

$$= \int_{-\infty}^{\infty} f(x_0 - t\sin\phi, y_0 + t\cos\phi)\,\mathrm{d}t \tag{4.5}$$

Define $L_{\phi,s}(x_0, y_0)$ to be the maximum length that may be travelled from point x_0, y_0 in either direction along $l_{\phi,s}$ without encountering any zero values. Note that this

function is only defined if the line $l_{\phi,s}$ actually passes through the point x_0, y_0. In terms of the above integral, we may write L as

$$L_{\phi,s}(x,y) = \int_a^b f(x_0 - t\sin\phi, y_0 + t\cos\phi)\,\mathrm{d}t = b - a \tag{4.6}$$

where a, b are chosen to satisfy

$$f(x(a), y(a)) = 0 \text{ and there is no } t' > a \text{ such that } f(x(t'), y(t')) = 0 \tag{4.7}$$

$$f(x(b), y(b)) = 0 \text{ and there is no } t' < b \text{ such that } f(x(t'), y(t')) = 0 \tag{4.8}$$

We now define the local angle of the point x_0, y_0 as the angle ϕ that maximizes $L_{\phi,s}(x_0, y_0)$ and offset by 90° because the direction of travel along the line $l_{\phi,s}$ is actually perpendicular to the direction indicated by ϕ:

$$\theta(x,y) = \underset{\phi}{\operatorname{argmax}}\,[L_{\phi,s}(x_0, y_0)] - 90 \tag{4.9}$$

It is useful to visualize an example. Suppose we have a binarized image in which 1 valued pixels are shown in white and 0 valued pixels are shown in black. We assume that all white pixels are nanowire and all black pixels are background[1]. An example of a small region of such an image is shown in Figure 4.5a. We wish to assign a single angle value to the pixel shown in blue in Figure 4.5b. To accomplish this, we begin by extending a horizontal line to the left and right of this selected (blue) pixel as far as it can go while remaining on the nanowire (i.e. while remaining on white pixels), as shown in Figure 4.5c. As this line rotates (shown in Figure 4.5d), we imagine its length expanding and contracting such that it is as long as it can be while still remaining fully on the white pixels. For a series of angular values between 0 and π, we record both the angle and the length of this line. A sample of these lines are

[1] In general, 1 valued pixels should be nanowires, but there is a good degree of noise in real images so some portions of nanowires are 0 valued and some portions of background are 1 valued.

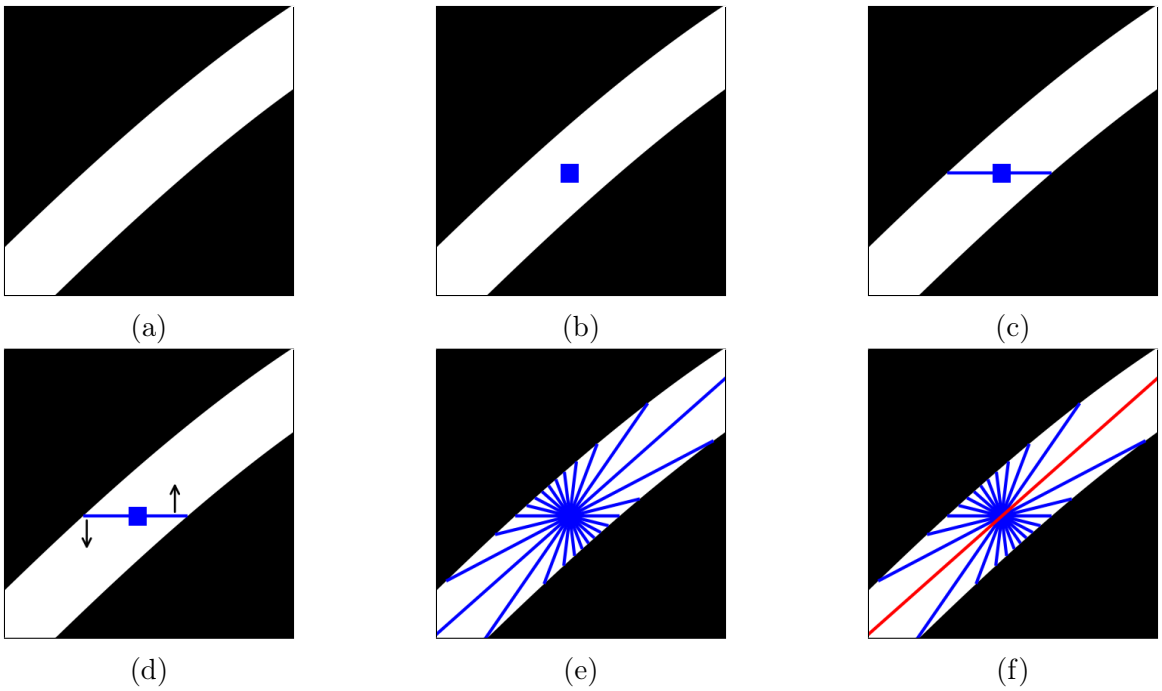

Figure 4.5: Pictorial description of a transform which we call the Radon Local Angle Transform. The angle assigned to the pixel shown in blue in Figure 4.5b is the angle that the red line of Figure 4.5f makes with the horizontal.

plotted in Figure 4.5e. We then identify the longest such line (highlighted in red in Figure 4.5f). The angle that this longest line makes with the horizontal is the angle assigned to the selected (blue) pixel.

An implementation of this algorithm in pseudocode is shown in Algorithm 1 which is based on the scikit-image [121, 99] implementation of the Radon Transform [97]. Note that in order to implement Algorithm 1 in practice, one must also define a zero-padding operation so that the contents of the image may be rotated while allowing the entire image to remain in frame. This therefore also requires an unpadding operation be performed after the inverse rotation.

There are several desirable features of Algorithm 1. First, the precision of the output can be tuned by using a finer-grained sequence of input angles $\{\theta\}$, although the finite resolution of the image sets a limit on the value of increasing angle sampling beyond a certain point. Secondly, many of the operations here can be described in terms of vector and matrix operations, such as indexing or rotation, and therefore

Algorithm 1 Radon Local Angle Transform Algorithm. Arguments are binary image tensor F of size $(m,\, n)$ and a sequence of angles $\{\theta_1,\, \theta_2,\, ...\, \theta_\ell\} = \{\theta\}$

function ROTATE(F, θ)
    returns F rotated by angle θ counter-clockwise about center, rounded to nearest integer.

function ROWCONTIGUOUS(F)
    $F' \leftarrow F$
    For each row of pixels in F', calculate the length of each contiguous sequence of 1-valued pixels in this row. Replace the value of each 1-valued pixel in this row of F' with the length of the contiguous row sequence to which they belong.
    Return F'

Declare L as empty tensor of size $(\ell,\, m,\, n)$
for all $\theta_i \in \{\theta\}$ **do**
    $G \leftarrow \text{ROTATE}(F,\, -\theta_i)$
    $G \leftarrow \text{ROWCONTIGUOUS}(G)$
    $G \leftarrow \text{ROTATE}(G, \theta_i)$

    for all $\mu \in \{1,\, 2,\, ...\, m\}$ **do**
        for all $\nu \in \{1,\, 2,\, ...\, n\}$ **do**
            $L_{i\mu\nu} \leftarrow G_{\mu\nu}$

Declare ϕ as empty tensor of size $(m,\, n)$
for all $\mu \in \{1,\, 2,\, ...\, m\}$ **do**
    for all $\nu \in \{1,\, 2,\, ...\, n\}$ **do**
        $j \leftarrow \text{argmax}_i(L_{i\mu\nu})$
        $\phi_{\mu\nu} \leftarrow \theta_j$

return ϕ

(a) Original Image (b) Binarized Image (c) Radon Local Angles

Figure 4.6: Demonstrating the Radon Local Angle Transform (RLAT) on a small section of a real SEM image of a nanowire network. Figure 4.6b was binarized using Otsu's Method [107]. Figure 4.6c shows each pixel color coded by its angle as determined by the RLAT. All angles are measured counterclockwise from the horizontal.

this code should be compatible with many highly optimized numerical libraries. Finally, the calculation of each layer in V is entirely independent, so this algorithm is ripe for parallelism. It is worth noting that we can decrease the number of rotations required to get a given resolution by defining a ColumnContiguous function and then applying both RowContiguous and ColumnContiguous to each rotated image, but results of the ColumnContiguous would correspond to measurements for the angle $\theta + \pi/2$ rather than θ.

As a concrete example, we consider the Radon Local Angle Transform (henceforth RLAT) of a small region of an SEM image of a nanowire network as shown in Figure 4.6. Figure 4.6a shows the original image. Figure 4.6b shows the result of binarization using Otsu's method [107]. Figure 4.6c shows the results of the RLAT where all angles are measured counterclockwise from horizontal and the color coding of a pixel corresponds to the angle value assigned to that pixel. Even before any further analysis, the results of the RLAT appear to have done a reasonable job of separating overlapping nanowires! Even discontiguous nanowires are colored consistently,

suggesting that this approach may help overcome some of the difficulties of applying MaskRCNN to crowded images.

Each pixel in Figure 4.6c can be uniquely described by a point $\vec{\mathbf{p}} = (c, r, \phi)$ where c is the column index (corresponding to its horizontal position), r is its row index (corresponding to its vertical position), and ϕ is its angle. We define a distance metric d between any two pixels with points $\vec{\mathbf{p}}_1$ and $\vec{\mathbf{p}}_2$ as

$$d(\vec{\mathbf{p}}_1, \vec{\mathbf{p}}_2) = \sqrt{(c_1 - c_2)^2 + (r_1 - r_2)^2} + \min\left(|\phi_1 - \phi_2|, 180 - |\phi_1 - \phi_2| \right) \quad (4.10)$$

The second term accounts for the fact that, since we are measuring angles using lines, the angular distance can be no more than 90°. In other words, a line with angle of 0° is indistinguishable from a line with angle of 180°. With this metric, and therefore a notion of closeness, defined, we can reframe our problem as one of data clustering: we want to find the sets of points that belong to the same cluster (i.e. sets of pixels that belong to the same nanowire). Before choosing a clustering algorithm, we note that our clustering algorithm cannot just cluster points separated by small distances - this would exclude points from the same nanowire with very similar angles if they are separated by many rows and columns. The chosen clustering algorithm must also be able to cluster points that are separated by large distances as long as they are connected by a chain of other points with small distances between them. Finally, we want to be able to exclude particulates and other objects that are not wire shaped, so the clustering algorithm should have some way of identifying data points that should be ignored. The algorithm known as DBSCAN [32, 104] (Density Based Spatial Clustering of Applications with Noise) fits the bill quite nicely. DBSCAN, in addition to clustering nearby *core* points together, also includes other points in the cluster if they are *reachable* by traversing an unbroken chain of core points. The most important free parameters of this algorithm are m and ε which define a core point as a point with at least m other points within a distance ε. DBSCAN then labels each data point with some label from -1, 0, 2, ... where -1 indicates noise and the nonnegative integers

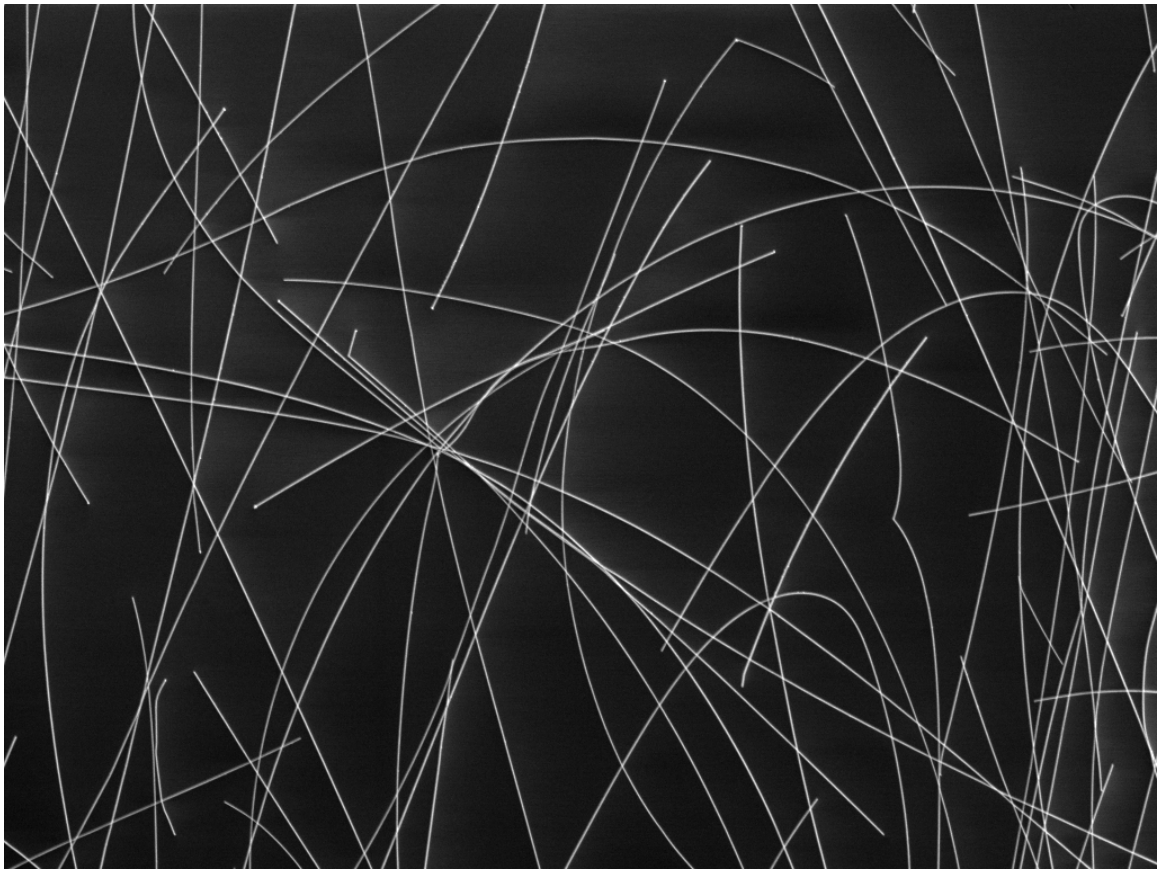

Figure 4.7: Clean, low density image of region of nanowire network

represent different clusterings (each clustering should, ideally, identify all pixels in an image belonging to a single nanowire). These nonnegative labels, when viewed as an image rather than as datapoints, become our instance segmentation masks.

One challenge in implementing this is the large number of data points that require classification from a given image. For example, in the very clean and relatively low density image shown in Figure 4.7, we have $N = 4.35E4$ nanowire pixels (and therefore data points) which gives us $N(N-1)/2 = 9.46E8$ pairwise distances to compute. In denser images, such as the ones produced by our most recent experiments, the number of computations and memory required will further increase. To circumvent this, we subdivide our images into a number of overlapping rectangles and then apply DBSCAN to each rectangle individually. Rectangles are chosen such that half of each rectangle's width overlaps with its neighbors to the left and right and half

of each rectangle's height overlaps with its neighbors above and below. To restitch our images together, we apply a a maximum weight matching algorithm [28, 37].

The matching algorithm requires a graph as input. To construct such a graph, we first select two adjacent and overlapping rectangles. For clarity, we will refer to these as the left rectangle and the right rectangle. All distinct masks contained in these rectangles are added as nodes in a graph. We then add edges such that our graph is bipartite: each node/mask from the left rectangle is connected to each node/mask in the right rectangle (and vice versa) but nodes/masks that come from the same rectangle are never connected. For a given edge connecting masks m_1, m_2, the edge weight is assigned to be the Intersection over Union (IoU) of the two masks. For our purposes, the intersection is defined as the number of points in common between the two masks and the union is defined as the number of points in either or both of the masks. With the graph thus defined, our max weight matching algorithm restitches nanowire instances across rectangle boundaries. For simplicity, we begin by restitching all rectangles in the same row and merging matched masks. We then apply the same matching algorithm to adjacent and overlapping pairs of reconstructed row segmentations.

As proof of concept, we will first test this algorithm on the extremely clean and relatively low density image from Figure 4.7. Some examples of the segmentations proposed by the combination of DBSCAN and the matching algorithm are shown in Figure 4.8. To quantify the performance of the algorithm, we must first match each predicted mask to a true mask. We achieve this result much as we stiched images together: we create a bipartite graph with one partition containing the predicted masks and the other partition containing the true masks with edge weights as IoUs. The correspondence between true and predicted masks is then produced by application of the maximum weight matching algorithm. For each pair of matched masks, we

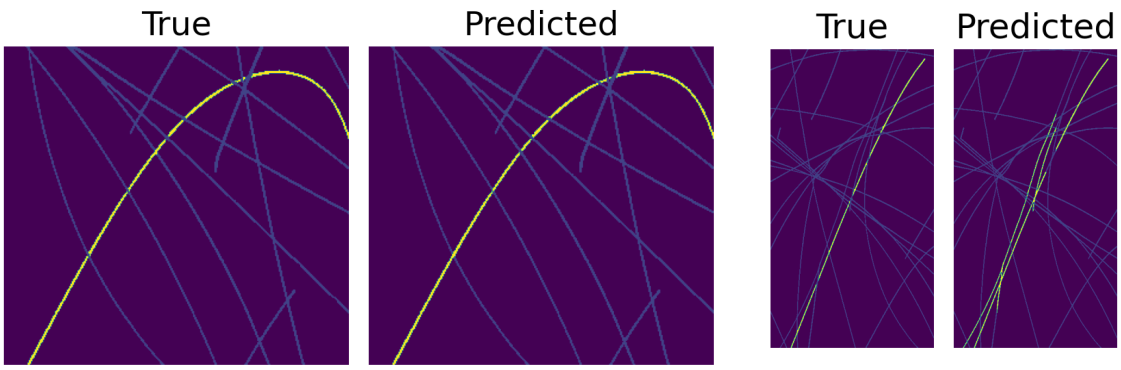

(a) Successful Segmentation (b) Failed Segmentation

Figure 4.8: Examples of segmentations produced by the combination of DBSCAN and the RLAT

quantify the performance of the algorithm by the Dice coefficient which is defined as

$$\text{Dice} = \frac{2\,TP}{2\,TP + FP + FN} \tag{4.11}$$

where TP , FP, and FN stand for True Positive, False Positive, and False Negative. True Positive is the number of pixels in both the true and predicted masks. False Positive is the number of pixels in the predicted mask but not in the true mask. False Negative is the number of pixels in the true mask but not in the predicted mask. Perfect segmentation gives a Dice coefficient of 1 and completely incorrect segmentation (which can be achieved in many ways) gives a Dice coefficient of 0. Note that if a true mask is not matched to a predicted mask then the Dice coefficient evaluates to zero. In general, the algorithm performs decently, yielding a mean Dice coefficient of 0.72. Examples of impressive and not-so-impressive segmentations are shown in Figure 4.8. These successes and failures are typical of the rest of the segmentation: the combination of RLAT+DBSCAN can successfully segment straight or curved nanowires as long as they do not intersect with other nanowires at a shallow angle, such as the highlighted curve shown in Figure 4.8a.

This is, already, a significant milestone and it strongly suggests that this algorithm is viable. With very little optimization, we have developed a straightforward

and automated algorithm for accurate segmentation of complex images of overlapping nanowires. In Figure 4.8b, we can see this algorithm's weakness: we have a collection of a nearly parallel and intersecting wires which are mistakenly identified as a single wire. This pattern repeats itself in many of the mistaken mask predictions. These failed masks pose a at least two problems. First, the geometry recovered from the mask may not faithfully represent the underlying nanowire geometry. Second, and perhaps more importantly, any nanowire pixels that are included in the wrong segmentation are thereby excluded from the correct segmentation since DBSCAN assigns data to mutually exclusive groups. This will lead to false distinctions between masks that should actually refer to different parts of the same wire. We propose several possible explanations for the failure of RLAT+DBSCAN to distinguish between wires intersecting at shallow angles.

It is possible that the RLAT+DBSCAN method is, in general, sound, but that hyperparameters (ε, m, and the size and shape of rectangular subsections) need to be optimized. Alternatively, is is possible that plausibly distinguishing between nanowires that intersect at shallow angles is too complex to be achieved by RLAT+DBSCAN. In this case, we would likely need to explore options using deep learning. Both optimization of RLAT+DBSCAN hyperparameters and using deep learning would require a large set of correctly annotated images of nanowire networks, but unfortunately no such dataset exists. Were we to create such a dataset using simulations, we would overcome one significant obstacles to using MaskRCNN, the deep learning architecture that has proven most successful in instance segmentation. Recall that MaskRCNN has been tested on structures such as nanowires before and been found wanting. Nonetheless, we shall test if a sufficient quantity and complexity of training images can overcome these previously found limitations. Therefore we now proceed with a discussion creating this synthetic data.

A synthetic image and a real image are shown side by side in in Figure 4.9. The pipeline generating each of these synthetic images can be broadly divided into two

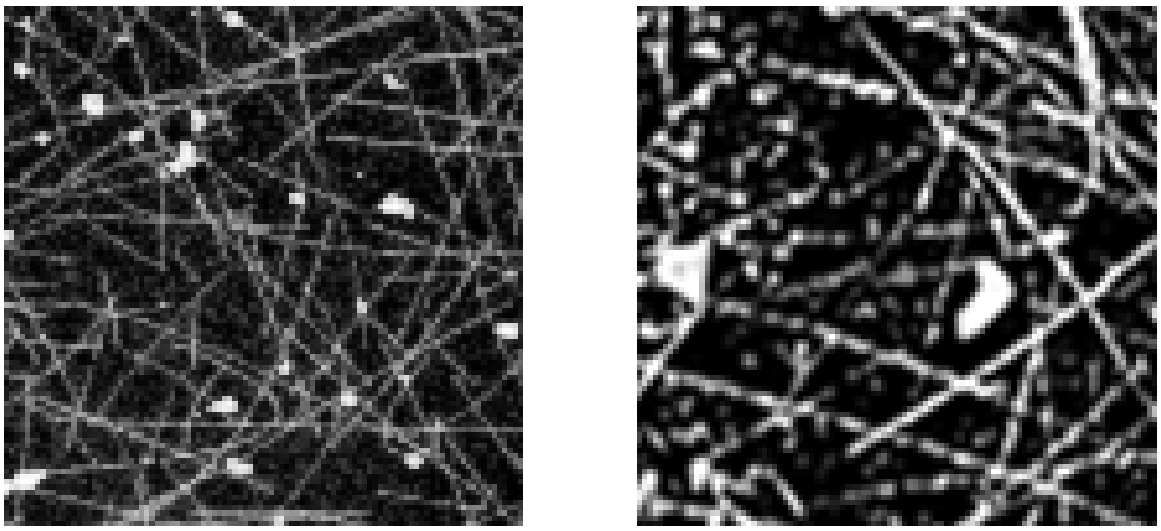

(a) (b)

Figure 4.9: Close up of real and synthetic image side by side. Readers are invited to try to determine which is which.

Real image: 4.9b, Synthetic image: 4.9a

stages: (1) creating the underlying geometrical model and (2) turning that model into a realistic image by adding imaging artifacts, particulates, noise, etc. We create a geometrical model by generating a sequence of planar curves with similar shapes as real nanowires. We use the measured distribution of nanowire lengths from Chapter 3 as input to draw simulated nanowire lengths from appropriate lognormal distributions. The trajectories of these simulated are curves are generated by imagining a particle with random initial position and momentum undergoing a series of collisions with other particles with random momenta and recording the initial particle's position after each collision. Collisions are separated by a fixed time t_{sep}, chosen at the time of data generation, that controls the curviness of the resulting wires (with higher values of t_{sep} yielding straighter nanowires). Widths of these nanowires are drawn from a distribution based on data from the supplier. We then generate an image from this geometry using the geospatial analysis tools shapely[38] and GeoPandas[57]. We then perform a series of noising operations to degrade image quality. Finally we use PoresPy[39] to generate correlated noise that we use to create both particulates and spatially correlated brightness variations.

We generated a sythetic dataset of 16,000 images as described in detail in Appendix A.7. After image generation, we perform a thresholding and then perform the RLAT on the thresholded image. To test the value of the RLAT, we train MaskR-CNN on two different kinds of input data. In the first case, the input image has three channels: a grayscale SEM-like image, the thresholded image, and RLAT image. In the second case, the input image also has three channels but the first and last are equal, so the channels are: a grayscale SEM-like image, the thresholded image, and the grayscale SEM-like image. We use the same underlying data in both cases.

We begin training MaskRCNN using a training set of 1024 images and a validation set of 256 images. We use a Resnet50 FPN backbone with weights pretrained on COCO [78]. The hidden layer used for classification has a width of 256. Maximum detections per image is set to 2000. We set our detector to have two possible classes (nanowire and non-nanowire). We use FastRCNN to predict bounding boxes. AdamW is the optimizer with learning rate scheduler and other hyperparameters as described in [94]. The training progress of these models is shown in Figure 4.10. Unfortunately, both samples here show evidence of almost immediate overfitting. The validation loss decreases over about 10 epochs before it starts to increase. Further, the performance of the model using the RLAT data as input appears to be a little bit worse than the model without using the RLAT data. This throws into question the utility of the RLAT as a preprocessing step for MaskRCNN. There is a possibility that the training data set is too small to capture the the full heterogeneity possible in our synthetic dataset, but the results do not change meaningfully when we incrase the training data set size. Furthermore, when training a model on synthetic data, we must expect some differences between the synthetic data and eventual target which is real data. If MaskRCNN cannot generalize from the training set to the validation set - which were both generated by the same algorithm using the same parameters - there is a vanishingly small chance that it will generalize from training data to experimental data. While it is true that MaskRCNN was trained for 27,000 epochs in previous

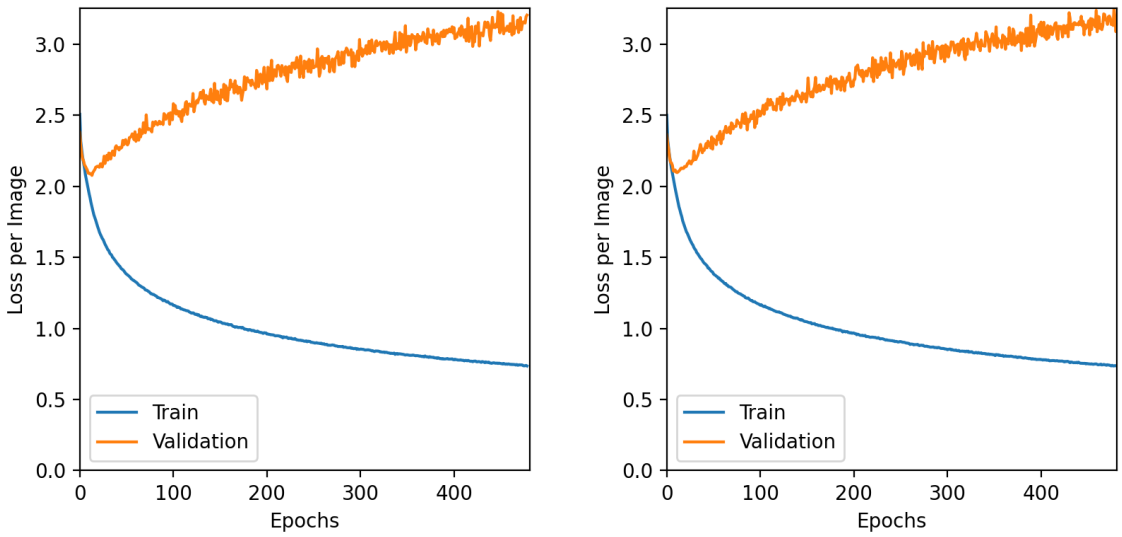

(a) Loss without RLAT input

(b) Loss with RLAT input

Figure 4.10: Training progress of MaskRCNN both with and without RLAT input included in training data.

nanowire segmentation work [35], the validation loss is continuing to increase so there is no reason to believe that further training would be beneficial.

Chapter 5

Conclusion

Transparent conducting electrodes (TCEs) are ubiquitous in modern life: from airplane windshields to cell phone screens, they are everywhere. The dominant material to make them, ITO, has several drawbacks. Networks of silver nanowires are among the most promising candidates to replace ITO, but these networks are liable to reconfigure themselves under electrothermal stress. This tendency toward reconfiguration is an obstacle toward widespread adoption of silver nanowire networks as TCEs but also, if it can be controlled, could serve as a platform for future nano-electronic engineering. In this work, we have applied a wide array of computational, analytical, and experimental tools to better understand how silver nanowire networks reconfigure themselves under electrothermal stress.

In Chapter 2, we demonstrated that certain concepts from graph theory such as betweenness centrality and other betweenness based measures of node importance can be used to identify nanowires in a simulated network that are systematically less important to conduction. By removing these wires, we can actually improve the TCE figure of merit of these simulated networks. This shows a potential application of this novel type of network attack to arbitrary networks: if the nodes in a network improve flow but at some finite cost, removing low betweenness centrality nodes may actually improve total efficiency of the network. Further, we demonstrated that Monte Carlo Tree Search is extremely efficient at finding these nodes to remove. The power of

these betweenness-based strategies lends creedence to the idea that high betweenness centrality nodes may fail preferentially in a real network under electrothermal stress.

In Chapter 3 we test this theory. First we developed a method for fabricating a large number of small, percolating silver nanowire networks. We then image the networks before and after subjecting them to electrothermal stress that destroys percolation. Using a semi-automatic image segmentation algorithm, we extract equivalent graphs from pre-ramp and post-ramp images and use these graphs to connect failure with properties of the network elements that have failed. We find good evidence that betweenness based centrality measures are correlated with a higher probability of failure but this correlation is not strong enough to be predictive. Furthermore, the graph theoretic measures do not appear to be as correlated with failure as is the calculated electrical current. The most valuable result here is that electromigration appears to be the primary driver of failure of inter-nanowire contacts in silver nanowire networks. Electromigration drives contact failure either by causing failure directly or by providing a crucial source of kinetic perturbations that initiate spheroidization.

In Chapter 4, we work to advance the state of the art in fully automated segmentation of images of nanowire networks, a problem that lies at the intersection of several hard problems in computer vision. We introduce a novel image analysis routine, which we call the Radon Local Angle Transform or RLAT, that maps each pixel in a binarized image to a direction. We demonstrate how this transform can be used with an existing clustering algorithm, DBSCAN, to perform fully automatic segmentation of very clean images of sparse nanowire networks but show that it fails for more dense networks with a greater proportion of noise. To make further progress, we generate a large number of synthetic images of nanowire networks with varying degrees of noise, clutter, and distortion. We test the current state-of-the-art model for instance segmentation, MaskRCNN, on these simulated images and find two results: (1) the RLAT does not appear to aid MaskRCNN in this context and (2) MaskRCNN shows an extreme inability to generalize - even failing to generalize between different partitions of the same synthetic dataset.

For future researchers, the path forward is clear. First and foremost, this present set of experiments should be reproduced with the goal of fabricating much cleaner nanowire networks. A great deal of time and energy was spent developing techniques to produce reliably sized and extremely small nanowire networks. Using the recipes developed here, future researchers will have time to wash samples, ensure the nanowire supply is reasonably free of particulates, and optimize SEM settings so resultant images are cleaner. In addition, different SEMs were used for the pre-failure and post-failure images. This introduces an unnecessary confounding variable in our analysis. In our case, it was necessary to change because the images produced by the first SEM were so grainy and time considerations precluded us from re-imaging the samples before conducting the voltage ramp. Using the same SEM in all images would provide a straightforward improvement in the quality of the results.

In terms of data analysis, the large simulated dataset we have produced here should be used to refine the hyperparameters of the DBSCAN+RLAT algorithm introduced here. Generating these images is computationally cheap, so new image parameters may be worth trying as well in the event that the current set of images does not sufficiently resemble the experimental data. The utility[1] function of this hyperparameter optimization should be the IoU metric between ground-truth segmentations and the machine-produced segmentations (where target and prediction masks are matched to each other using the maximum weight matching algorithm discussed in Chapter 4). Assuming that future researchers are able to get the DBSCAN+RLAT method to produce reliable segmentations, wire diameters can be retrieved by applying a euclidean distance transform[2] to each instance mask. This transform is a well-tested approach to extracting width information from tubelike structures [35].

There is also room to further test deep-learning approaches to the segmentation

[1] if a loss function is necessary instead, one could use the negative IoU

[2] A euclidean distance transform maps each nonzero pixel in a binary image to the distance from that pixel to the nearest zero valued pixel

of these highly cluttered images. To denoise the existing images, we suggest using a binary classification tool such as a U-Net [100]. By treating the denoising operation as a binary classification problem, we may achieve two goals the same time: removing particulates and noise from the image (because they are regognized as non-nanowires) and binarizing the image without using thresholding algorithms. Then one could feed this clean, binarized image into MaskRCNN. In addition, novel variants of MaskR-CNN have been introduced that use transformers and show improved performance, so these should be tested as well.

In this work, we have provided a recipe for the future analysis of silver nanowire network failure. We have shown the utility of both Monte Carlo Tree Search and betweenness centrality as combinatorial optimization tools for pruning networks in which the target property is maximum conductivity with the minimmum number of nodes. The image analysis methods demonstrated here, especially the Radon Local Angle Transform, are well-suited to analysis of any class of image containing primarily tubular structures. We have provided evidence that the preponderance of contact failures in silver nanowire networks under electrothermal stress are driven either directly or indirectly by electromigration, and that therefore preventing electromigration should be a top priority in future devices. In doing so, we have pushed networks of silver nanowires ever closer to widespread adoption.

Chapter 6

Afterword

When people ask why I pursued a PhD in Physics, I tell the truth: I thought it would be fun. This usually elicits some combination of guffaws and assertions that I am a masochist. The truth is it *was* fun. There were of course setbacks and failures and months in which I felt that I might just be the worst scientist to ever live. On average, though, it was a great time. I consider myself very lucky to have had this opportunity. At the behest of my committee, I include here a series of brief meditations on my experiences during my PhD. I certainly hope these will guide some future scientist as they begin their career but, given the typical readership of a PhD thesis, it's much more likely these memories will serve only as a letter to my future self. If the future Dr. Trebach ever reads this, I hope he finds my words entertaining. Failing that, I hope he does some serious reflection on how he lost his sense of humor.

6.1 Read, Damnit!

> Why spend a day in the library when you can learn the same thing by working in the laboratory for a month?
>
> Frank Henry Westheimer

Professor Westheimer was obviously being sarcastic when he delivered the above quip, but it reveals something deep and true about research: there is much more joy in discovering something for yourself than there is in reading about it in a journal. Unfortunately, discovering everything for yourself is a terribly inefficient way to use your time. I have probably learned this lesson a dozen times by now. Of course failed experiments tend not to get published, so if you are trying something that doesn't work, there's a good chance another scientist also knows it doesn't work but couldn't find a journal to publish it. More often than not, though, I found myself learning things twice. Once as the result of much toil and trouble and then again, much later, gift-wrapped in someone else's paper - a present I had never bothered to open. If you are a young academic, building a reading habit is one of the best things you can do. Now that I think about it, this actually holds for old academics too.

There are many corollaries to this lesson of "read before you leap." One of the best, in my opinion, is the understanding that review papers are invaluable when you are starting something. Reviews are written for a (comparatively) general audience. They usually include very helpful background; they tend to define jargon that would elsewhere be used without explanation; and they typically contain references to many seminal results in the field.

Of course you cannot spend *all* your time reading - to do research you must do some original work of your own. But many scientists, absolutely including me, would benefit from spending more time reading. There are giants among us; if our goal is

to see further, we would be fools not to stand upon their shoulders.

6.2 The Seduction of Simplicity

If you have an idea that seems novel, easy, and promising ... no you don't. If the idea truly is easy and promising, it likely isn't novel . If it the idea truly is novel and easy, it might not be that valuable. And if an idea truly is promising and novel, you can bet your bottom dollar that it is *not* easy. I doubt that this rule holds all the time, but it's certainly a good heuristic to keep in mind.

Based on my experiences, I think it is best to focus on finding things that are promising and novel and assuming that everything will be hard to execute if you want to do it well. Therefore you should try to choose projects that will require you to learn skills you want to have. That way, even if the idea doesn't pan out, you've learned how to do something you care about.

6.3 Unsigned Stirling Numbers of the First Kind

Figure 6.1: The truest tweet ever twote. Permalink

I expected, correctly, that I would not be the smartest person at MIT. I did not expect, however, to so regularly feel so very stupid. I remember walking into a colloquium about the relevance of the p-adic numbers to string theory. The lecture washed over me. It was a melange of phonemes, a sound salad. If there had not been others in the room nodding and chuckling to themselves, I would not have believed it to be language.

My point here is that there are a great many things to know, and you cannot hope to know all of them. We do research because we want to learn and discover, so not being able to know everything is quite unpleasant. I tried to comfort myself with the notion that, by the time I graduated, I would know as much as these other people. This was a bad strategy. While I was learning my colleagues were learning too. Even worse, they were learning *faster than me*. Of course I (usually) didn't begrudge my friends for being so darn smart. I just wanted to be that smart too!

This line of thinking is a trap. I was actually told this multiple times during my tenure here, but I suppose there are some mistakes you must make for yourself. For me, the way out was to focus on myself. Rather than comparing myself to my colleagues, I would compare myself today to myself yesterday. The goal is to become a little bit better every day, at least on average. Making lists of bite-sized tasks and checking them off greatly helped with this. That way, if I ever felt like I wasn't accomplishing anything, I could look through my pages and pages of checklists and see hard evidence that I was working and learning and growing. This isn't something I've mastered - it's hard to do when surrounded by such brilliant people. But being around these people has certainly worth the trouble of keeping a list. So if you feel like you aren't accomplishing anything, really try to keep track of how you spend your time. It's very likely you aren't giving yourself enough credit.

Appendix A

A.1 Transparency Calculations

Transparency calculations are based on the formalism developed in [60]. Equations A.5-A.6 are derived from the Mie scaterring solution for plane waves incident on infinite cylinders [96].

$$T = e^{-n_s C_{\text{ext}}} \tag{A.1}$$

$$C_{\text{ext}} = \frac{1}{2}\left(C_{\perp} + C_{\parallel}\right) \tag{A.2}$$

$$T_{\parallel}(\theta) = a_0 + 2\sum_{1}^{\infty} a_n \cos(n\theta) \tag{A.3}$$

$$T_{\perp}(\theta) = b_0 + 2\sum_{1}^{\infty} b_n \cos(n\theta) \tag{A.4}$$

$$C_{\parallel} = \mathrm{Re}\left\{\frac{2\lambda\ell}{\pi}T_{\parallel}(0)\right\} = \mathrm{Re}\left\{\frac{2\lambda\ell}{\pi}\left(a_0 + 2\sum_{n=1}^{\infty} a_n\right)\right\} \tag{A.5}$$

$$C_{\perp} = \mathrm{Re}\left\{\frac{2\lambda\ell}{\pi}T_{\perp}(0)\right\} = \mathrm{Re}\left\{\frac{2\lambda\ell}{\pi}\left(b_0 + 2\sum_{n=1}^{\infty} b_n\right)\right\} \tag{A.6}$$

n_s is the number density of nanowires in wires per square meter. The constants $C_{\perp}$, $C_{\parallel}$ are, respectively, the extinction cross sections for light polarized perpendicular and parallel to the long axis of the wire while C_{ext} is the average of these. ℓ is the length of a single nanowire (10µm in our simulations). a_n and b_n are defined in [96] (pg 276). Because we are considering the $r = 0$ case (a homogeneous cylinder), the expressions for a_n and b_n can be substantially simplified and are shown in Eqs. A.7-A.8.

$$a_n = \frac{J_n(x_r)J_n'(m_r x_r) - m_r J_n'(x_r)J_n(m_r x_r)}{H_n(x_r)J_n'(m_r x_r) - m_r H_n'(x_r)J_n(m_r x_r)} \tag{A.7}$$

$$b_n = \frac{m_r J_n(x_r)J_n'(m_r x_r) - J_n'(x_r)J_n(m_r x_r)}{m_r H_n(x_r)J_n'(m_r x_r) - H_n'(x_r)J_n(m_r x_r)} \tag{A.8}$$

J_n are the Bessel functions of the first kind. H_n are the Hankel functions of the first kind. $x_r = k_0 R$ where k_0 is the wavenumber of the incident radiation in surrounding medium, which we treat as air, and R is the radius of the cylinder (0.075µm in our simulations). m_r is the ratio of the wire's refractive index to the surrounding medium's refractive index. Because the surrounding medium is air (refractive index = 1 [22]), m_r is simply the refractive index of silver at $\lambda = 550$nm which is $n = 0.055 + 3.32i$ [120]. Using these values, we calculate

$$C_{\text{ext}} = 2.7 * 10^{-12}\text{m}^2 \tag{A.9}$$

A.2 Haze Calculations

Haze is defined as the proportion of transmitted light that is refracted at an angle between 2.5° and 90° upon exiting the nanowire film. As defined in [60], the haze can be calculated as

$$H = \frac{F_{12}F_{23}(C_{2.5}^{90}/(C_{\text{ext}})\left(1 - e^{-n_s C_{\text{ext}}}\right)}{F_{12}F_{23}F_{31}e^{-n_s C_{\text{ext}}} + F_{12}F_{23}(C_0^{90}/(C_{\text{ext}})\left(1 - e^{-n_s C_{\text{ext}}}\right)} \tag{A.10}$$

where

$$C_{\alpha 1}^{\alpha 2} = \frac{2\lambda\ell}{\pi}\int_{\theta 1}^{\theta 2}\frac{1}{2}\left(F_{\parallel 31}|T_{\parallel}(\theta)|^2 + F_{\perp 31}|T_{\perp}(\theta)|^2\right)\sin(\theta)d\theta \tag{A.11}$$

Our optical interfaces are labeled as

$$12 = \text{air} \rightarrow \text{air}$$

$$23 = \text{air} \rightarrow \text{nanowire film}$$

$$31 = \text{nanowire film} \rightarrow \text{air}$$

$T_{\parallel}$ and $T_{\perp}$ are as defined in Eqs. A.5-A.6. The angle dependent fresnel transmission terms are

$$F_{\parallel 31}(\theta) = \frac{\sin(2\theta)\sin(2\alpha)}{\sin^2(\theta+\alpha)}$$
$$F_{\perp 31}(\theta) = \frac{\sin(2\theta)\sin(2\alpha)}{\sin^2(\theta+\alpha)\cos^2(\theta-\alpha)}$$

with θ being the angle of propagation in the nanowire film and α being the angle of propagation in the air beyond the film. Note that α and θ are related by Snell's law. F_{ij} are the angle averaged Fresnel transmission terms at each optical interface

$$F_{ij} = \frac{4n_i n_j}{(n_i + n_j)^2} \tag{A.12}$$

Note that $F_{12} = 1$ and is only included for notational consistency with the source material. Unlike in [60], we ignore the presence of a glass or PET substrate for the nanowires when calculating transparency and haze. Note also that the index of refraction n_3 is the index of refraction of the film of nanowires, not of bulk silver.

Because our networks comprise homogeneous wires, the haze is a pure and monotonic function of nanowire areal density. For this reason, the plot of Haze vs Sheet Resistance in Fig. 1.1 looks very similar to a rotated version of the plot of Sheet Resistance vs Density included in the main paper. Plotting the haze vs density would only show a single line, because all networks at the same density will have the same haze using this method.

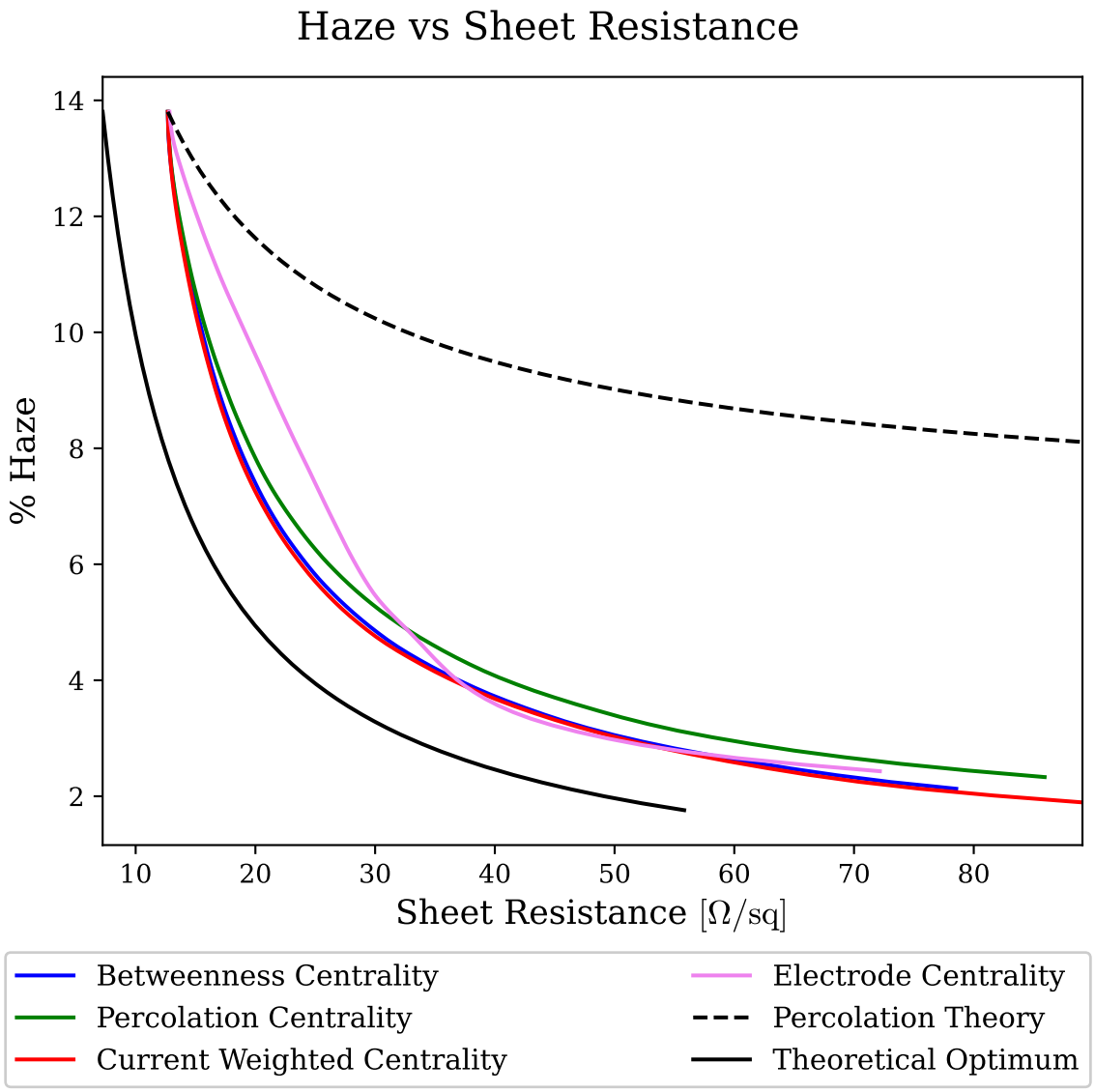

Figure 1.1: Plot of Haze as a function of sheet resistance.

A.3 Resistance of a Theoretically Optimal Network

In the following, we derive an expression for the resistance of an "optimal" network of nanowires. Using this theoretical network, we can compare the performance of real nanowire networks to the best possible performance at a given density. First, consider some random network of nanowires with length ℓ that are deposited on a square sample of side length L. Define N_{tot} to be the total number of nanowires in this random network.

Now consider the optimal network: a regularly spaced grid of nanowires. Each nanowire has length ℓ. The substrate onto which the nanowires are deposited is a square of side length L. The substrate has, on the top and bottom, long wires of length L that serve as the cathode and anode. Between the cathode and anode is a regularly spaced grid of nanowires each of length $\ell < L$. The number of vertical nanowires required to span the sample is

$$N_{\text{span}} = \frac{L}{\ell} \tag{A.13}$$

and the number of contacts between the vertical nanowires in this series (including contacts with the electrodes) is

$$N_{\text{contacts}} = \frac{L}{\ell} + 1 \tag{A.14}$$

Let R_c be the contact resistance at any junction between nanowires or between a nanowire and an electrode. Let R_w be the internal resistance of a single nanowire. The series resistance of a single straight path spanning the distance from one electrode to the other is the sum of the contributions from contact resistances and internal resistances.

$$R_{\text{span}} = N_{\text{span}} R_w + N_{\text{contacts}} R_c = \frac{L}{\ell} R_w + \left(\frac{L}{\ell} + 1 \right) R_c \tag{A.15}$$

Assuming that the random and optimal networks are at the same density, the number of nanowires in the random network (N_{tot}) will turn into $N_{\text{span}}^{\text{tot}}$ spanning sets of nanowiresin the optimal network.

$$N_{\text{span}}^{\text{tot}} = \frac{N_{\text{tot}}}{N_{\text{span}}} = \frac{N_{\text{tot}}}{L/\ell} \tag{A.16}$$

The spanning sets of nanowires will be both horizontal and vertical. Only the vertical sets will contribute to conduction between the electrodes. Therefore the number of spanning sets of nanowires that contribute to conduction is $N_{\text{span}}^{\text{tot}}/2$. As these spanning sets are equivalent to resistors in parallel, we can say that the resistance between the electrodes is

$$R_{\text{optimal}} = \frac{R_{\text{span}}}{N_{\text{span}}^{\text{tot}}/2} \tag{A.17}$$

$$= \frac{2R_{\text{span}}}{N_{\text{tot}}/(L/\ell)} \tag{A.18}$$

$$= \frac{2R_{\text{span}}}{N_{\text{tot}}\ell/L} \tag{A.19}$$

Note that the total number of wires N_{tot} can also be expressed as the number density of wires (n_s) times the area of the sample: $N_{\text{tot}} = n_s L^2$ which yields

$$R_{\text{optimal}} = \frac{2R_{\text{span}}}{n_s L^2 \ell/L} \tag{A.20}$$

$$= 2\frac{R_{\text{span}}}{n_s L\ell} \tag{A.21}$$

$$= 2\frac{\frac{L}{\ell}R_w + \left(\frac{L}{\ell}+1\right)R_c}{n_s L\ell} \tag{A.22}$$

If we then take the contact resistance R_c to be the average contact resistance $\langle R_c \rangle$ at junctions in our random network, we get

$$R_{\text{optimal}} = 2\frac{\frac{L}{\ell}R_w + \left(\frac{L}{\ell}+1\right)\langle R_c \rangle}{n_s L\ell} \tag{A.23}$$

A.4 Correcting for Finite Size Effects

Formally, the percolation threshold is the density at which there is a 50% chance of forming an *infinite* connected cluster of sticks. Dealing with finite networks requires some modification of this definition. We define percolation as the existence of a cluster of sticks that is connected to both the cathode and anode. Because our samples are finite, we must rescale our percolation threshold. The standard expression for this density in an infinite network is

$$n_c = \frac{5.63726}{\ell^2} \tag{A.24}$$

Where n_c is the critical density in wires per area and ℓ is the wire length [71]. Defining L to be the side length of our square samples, we can get an expression for the rescaled, effective percolation threshold using an empirical expression from [70].

$$n_c^{\text{eff}} = \frac{5.63726}{\ell^2} + \frac{1}{\ell L} + \frac{5.5}{L^2} \tag{A.25}$$

We measure all densities in terms of the dimensionless parameter α which represents density divided by the critical density

$$\alpha = \frac{n}{n_c^{\text{eff}}} = \frac{N_w/L^2}{\frac{5.63726}{\ell^2} + \frac{1}{\ell L} + \frac{5.5}{L^2}} = \frac{N_w}{5.63726L^2/\ell^2 + L/\ell + 5.5} \tag{A.26}$$

Where N_w is the number of wires of length ℓ in the network. Because our nanowires are subdivided, though, the number of nanowires in the network at any given time is not obvious. To circumvent this, we multiply the numerator and denominator of the above by ℓ^2

$$\alpha = \frac{N_w \ell^2}{5.63726L^2 + L\ell + 5.5\ell^2} \tag{A.27}$$

Note that the term $N_w\ell$ is the number of wires times the length per wire and is therefore equal to the total length of all wire segments on the sample, a quantity we

call Σ_ℓ.

$$\alpha = \frac{\ell \Sigma_\ell}{5.63726L^2 + L\ell + 5.5\ell^2} \tag{A.28}$$

With this expression, can measure the density of the network, relative to n_c^{eff}, without explicit reference to the number of wires present. With this rescaling, we must also modify our expression giving the relationship between resistance and density near the percolation threshold. With no rescaling, we have

$$R_s \propto (n - n_c)^{-\gamma} \tag{A.29}$$

To account for the finite size of our network, we convert this expression to be

$$R_s \propto (n - n_c^{\text{eff}})^{-\gamma} = n_c^{\text{eff}} \left(\frac{n}{n_c^{\text{eff}}} - 1 \right)^{-\gamma} = n_c^{\text{eff}} (\alpha - 1)^{-\gamma} \tag{A.30}$$

which assumes that the critical exponent γ is unaffected by the network's finite size. Because n_c^{eff} is a constant, it can simply be absorbed into the constant of proportionality yielding

$$R_s \propto (\alpha - 1)^{-\gamma} \tag{A.31}$$

We fix the constant of proportionality by matching the theoretical resistance to the simulated resistance at the starting (highest) density before any nodes are removed α_0, and define $R_0 = R_s(\alpha_0)$.

$$R_s = C(\alpha - 1)^{-\gamma} \tag{A.32}$$

$$R_s(\alpha_0) = R_0 = C(\alpha_0 - 1)^{-\gamma} \tag{A.33}$$

$$C = R_0(\alpha_0 - 1)^{\gamma} \tag{A.34}$$

$$R_s = R_0 \left(\frac{\alpha - 1}{\alpha_0 - 1} \right)^{-\gamma} \tag{A.35}$$

A.5 Monte Carlo Tree Search Implementation

We define actions and states here such that readers could reproduce this method by reading this appendix and [17]. To understand how MCTS is applied, we first reframe our problem as a Markov Decision Process defined by a set of states S and a set of actions A. Each state is a graph comprising a set of nodes N representing nanowire segments and a set of edges E representing connections between these nanowire segments. Recall that each nanowire may contain multiple segments and therefore may correspond to multiple nodes. Connected nodes that come from the same nanowire are connected by internal edges. Connected nodes that come from different, intersecting nanowires are connected by contact edges.

We define the percolating cluster to be the cluster of nodes connected to current source (cathode) and current sink (anode). We define a dangling end to be a nanowire that is connected to exactly one other nanowire through a contact edge. Each possible action a involves the following

1. Select a node $n \in N$ at random
2. Remove n from the graph along with any other nodes that are part of the same nanowire as n.[1]
3. While there are any remaining nodes that are not in the percolating cluster or or remaining nodes in dangling ends, remove those nodes. Repeat this process until there are no more dangling ends and all remaining nodes are in the percolating cluster.

For some starting state s_0, the full state space S contains s_0 as well as any other state that can be reached from s_0 by a sequence of actions. A state is defined as terminal

[1]Note that this strategy is actually somewhat problematic. Nanowires with many segments and therefore many nodes will be chosen more frequently than other nanowires. Nanowires have many segments because they intersect with many other nanowires. Therefore the nanowires that are preferentially sampled are ones that are somewhat more likely to be important to conduction. This likely artificially degrades the de-densification power of MCTS. In future work, scientists should instead select *nanowires* at random, rather than individual segment nodes.

if there is no longer a path connecting current source and current sink. The reward function of a terminal state is the FOM of its parent state divided by 200. We divide by 200 to ensure that reward values lie on the interval $[0, 1]$ which is required for the Upper Confidence Bound [17] to properly minimize regret.

A.6 Regressions with Varying Model Parameters

Table A.1 shows the results of several logistic regressions on the same experimental data trying to predict failure. The regressor treats failure as the positive outcome (value 1) and remaining intact as the negative outcome (value 0), so a positive coefficient indicates that an increase in the associated attribute will increase failure probability while a negative coefficient indicates that an increase in the associated attribute will decrease failure probability. For a given class (0 or 1), balanced class weighting is implemented as

$$w_i = \frac{N}{2N_i} \tag{A.36}$$

where w_i is the weight for class i, N is the total number of samples, and N_i is the number of samples with a true label of i. L2 regularization is implemented with a coefficient of 1, so this adds a term of $\vec{\mathbf{B}} \cdot \vec{\mathbf{B}}$ to the negative log loss function during optimization. The value of $\vec{\mathbf{B}}$ is defined in Equation 3.10.

Model Parameters	Attribute	Nanowire Segments	Contacts
No class weighting, no regularization	Current	3.5	18
	Power	3.3	-25
Balanced class weighting, no regularization	Current	4.7	22
	Power	13	-32
No class weighting, L2 regularization	Current	3.3	2.5
	Power	2.5	0.36
Balanced class weighting, L2 regularization	Current	4.8	15
	Power	11	-17

Table A.1: Logistic regression coefficients extracted from data in Chapter 3. First row is reproduction of the regression results from Table 3.4

Attribute	Draw Frequency	Distribution	Units
Resolution	Once per image	$U(2.58, 9)$	pixels/µm
Wire length / area	Once per image	$U(0.44, 1.5)$	1/µm
s	Once per image	$U(0.33, 0.8)$	None
μ	Once per image	$U(-1.74, -1.69)$	µm
Y	Once per image	$U(6.57, 20.2)$	µm
Sample width w	Once per image	$U(40, 90)$	µm
Sample height h	Once per image	$U(50, 100)$	µm
Nanowire length l	Once per nanowire	Eq. A.37	µm
Nanowire Diameter	Once per nanowire	$\mathcal{N}(0.120, 0.02)$	µm
Number anchors n	Once per nanowire	$p_n \propto 1/n,\ 2 \leq n \leq 5$	None
$\vec{\mathbf{v}}_\sigma$	Once per image	$U(5, 15)$	µm s^{-1}
$\vec{\mathbf{v}}$	$n-1$ times per nanowire	$\mathcal{N}\left(\vec{\mathbf{0}}, \vec{\mathbf{v}}_\sigma\right)$	µm s^{-1}
t_-	Once per image	$U(0.1, 1)$	s
t_+	Once per image	$U(2, 7)$	s
α	Once per image	$U(1.1, 10)$	None
t'	Once per nanowire	$\dfrac{e^{-t'}}{1 - 1/\alpha}$	None

Table A.2: Table of of properties used in generating synthetic data. In the distribution column, $U(a, b)$ denotes the uniform distribution with support only between a and b; $\mathcal{N}(\mu, \sigma)$ indicates the normal distribution with mean μ and standard deviation σ.

A.7 Synthetic Image Generation

As discussed in Chapter 4, the process of generating synthetic images can be broadly divided into two stages: (1) creating the underlying geometrical model and (2) turning that model into a realistic image by adding imaging artifacts, particulates, noise, etc. A table of parameters and distributions used in generating the geometric model are shown in Table A.2.

To ensure heterogeneity in our dataset, the values in the "Attribute" column are drawn from the distribution in the "Distribution" column with frequency as indicated in the "Draw Frequency" column. In the distribution column, $U(a, b)$ indicates the uniform distribution with lower bound a and upper bound b while $\mathcal{N}(\mu, \sigma)$ indicates the normal distribution with mean μ and standard deviation σ. As much as possible, these values are informed by the experimental data collected in Chapter 3. The bounds of the distributions for resolution, wire length per area, s, μ, and Y are set

with the distribution lower bounds equal to 0.85 times the experimentally observed lower bounds and the upper bounds equal to 1.15 times the experimentally observed upper bounds. The per sample values of μ, Y, s are obtained by a maximum likelihood fit of the lognormal distribution of Equation A.37 to the observed nanowire length distributions for that sample.

$$p(l \mid s, \mu, Y) = \frac{1}{s(l-\mu)\sqrt{2\pi}} \exp\left(\frac{\ln^2\left(\frac{l-\mu}{Y}\right)}{2s^2}\right) \tag{A.37}$$

The width and height of the sample are drawn from uniform ditribution with bounds of 40–90 µm for width and 50–100 µm for height. This yields synthetic images that cover roughly half the area of our experimental images, but this is necessary because, at typical resolutions, images of experimental size cannot fit on a GPU during MaskR-CNN training. To create an image, nanowires are added individually according the previously drawn parameters until the target density is reached (or exceeded). We use wire length per area rather than number density of nanowires because our sample is considerably smaller than a single nanowire. It is therefore somewhat undefined exactly how to quantify a single nanowire. The notion of total nanowire length, however, does not suffer from this ambiguity and is also a suitable way of specifying nanowire density.

The process of adding a single nanowire to the image begins with drawing a target length l, a number of anchors n, an initial timestep t_0, and an initial position somewhere on the sample. The parameters l and n are drawn as described in Table A.2. The value of t_0 is set by

$$t_0 = t_- + (t_+ - t_0)\left(1 - \frac{t'}{\ln \alpha}\right) \tag{A.38}$$

where t', t_-, t_+ have been drawn as described in Table A.2. The initial position $\vec{\mathbf{r}}_0$ is drawn from a uniform distribution covering the entire rectangular sample region. The point $\vec{\mathbf{r}}_0$ is the first of the n anchor points. Then a sequence $\vec{\mathbf{v}}_1, \vec{\mathbf{v}}_2, ...\vec{\mathbf{v}}_{n-1}$ of

$n-1$ velocities are drawn from the distribution $\mathcal{N}(\vec{\mathbf{0}}, \vec{\mathbf{v}}_\sigma)$. We then iterate through this sequence starting at the second velocity and setting $\vec{\mathbf{v}}_m \leftarrow \vec{\mathbf{v}}_m + \vec{\mathbf{v}}_{m-1}$. These velocities are then turned into the other $n-1$ anchor points using the relations

$$\vec{\mathbf{r}}_m = \begin{cases} \vec{\mathbf{r}}_0 \text{ if } i = 0 \\ \vec{\mathbf{r}}_{m-1} + \vec{\mathbf{v}}_m t_0 (1.1)^{-m} \end{cases} \tag{A.39}$$

These anchor points are then splined into a curve using the scipy utility SPLPREP with $k = n-1$ and represented by a sequence of 100 points obtained by evaluating the spline. If the curve is longer than the drawn value of l, which is almost always the case, the line is shortened by removing some points until its length is correct.

We add noise to the images using PoresPy [39]. We first add large scale, mostly transparent, spatially correlated gaussian noise to simulate brightness fluctuations. Then we add small scale, mostly opaque, spatially correlated gaussian noise to simulate particulates on the sample surface.

Bibliography

[1] Artificial intelligence: Google's AlphaGo beats Go master Lee Se-dol. *BBC News*, March 2016.

[2] Stress Evolution and Damage Formation in Confined Metal Lines under Electric Stressing: 1D Analysis. In Chao-Kun Hu, Martin Gall, Paul S. Ho, and Valeriy Sukharev, editors, *Electromigration in Metals: Fundamentals to Nano-Interconnects*, pages 80–126. Cambridge University Press, Cambridge, 2022.

[3] Abundance of Elements in the Earth's Crust and in the Sea. In John R. Rumble, editor, *CRC Handbook of Chemistry and Physics*. CRC Press/Taylor & Francis, 104 edition, 2023.

[4] Sheet resistance, April 2023. Page Version ID: 1151451760.

[5] Yumi Ahn, Youngjun Jeong, Donghwa Lee, and Youngu Lee. Copper Nanowire–Graphene Core–Shell Nanostructure for Highly Stable Transparent Conducting Electrodes. *ACS Nano*, 9(3):3125–3133, March 2015. Publisher: American Chemical Society.

[6] Réka Albert, Hawoong Jeong, and Albert-László Barabási. Error and attack tolerance of complex networks. *Nature*, 406(6794):378–382, July 2000. Bandiera_abtest: a Cg_type: Nature Research Journals Number: 6794 Primary_atype: Research Publisher: Nature Publishing Group.

[7] J. M. Anthonisse. The rush in a directed graph. *Journal of Computational Physics*, January 1971.

[8] Mukti Aryal, Joseph Geddes, Oliver Seitz, Jonathan Wassei, Ian McMackin, and Boris Kobrin. 16.1: Sub-Micron Transparent Metal Mesh Conductor for Touch Screen Displays. *SID Symposium Digest of Technical Papers*, 45(1):194–196, 2014. _eprint: https://onlinelibrary.wiley.com/doi/pdf/10.1002/j.2168-0159.2014.tb00053.x.

[9] Daniel Bellet, Mélanie Lagrange, Thomas Sannicolo, Sara Aghazadehchors, Viet Huong Nguyen, Daniel P. Langley, David Muñoz-Rojas, Carmen Jiménez, Yves Bréchet, and Ngoc Duy Nguyen. Transparent Electrodes Based on Silver Nanowire Networks: From Physical Considerations towards Device Integration. *Materials*, 10(6):570, June 2017. Number: 6 Publisher: Multidisciplinary Digital Publishing Institute.

[10] Allen T. Bellew, Hugh G. Manning, Claudia Gomes da Rocha, Mauro S. Ferreira, and John J. Boland. Resistance of Single Ag Nanowire Junctions and Their Role in the Conductivity of Nanowire Networks. *ACS Nano*, 9(11):11422–11429, November 2015.

[11] Bentley and Ottmann. Algorithms for Reporting and Counting Geometric Intersections. *IEEE Transactions on Computers*, C-28(9):643–647, September 1979. Conference Name: IEEE Transactions on Computers.

[12] Ran Bi, Chuantao Zheng, William W. Yu, Weitao Zheng, and Dingdi Wang. Breaking through the plasma wavelength barrier to extend the transparency range of ultrathin indium tin oxide films into the far infrared. *Journal of Applied Physics*, 134(16):165301, October 2023.

[13] Aveek Bid, Achyut Bora, and A. K. Raychaudhuri. Temperature dependence of the resistance of metallic nanowires of diameter >= 15 nm : Applicability of Bloch-Gruneisen theorem. *Physical Review B*, 74(3):035426, July 2006.

[14] Donald I. Bleiwas. Byproduct Mineral Commodities Used for the Production of Photovoltaic Cells. Circular 1365, 2010. Series: Circular.

[15] Ulrik Brandes. A faster algorithm for betweenness centrality*. *The Journal of Mathematical Sociology*, 25(2):163–177, June 2001.

[16] Ulrik Brandes. On variants of shortest-path betweenness centrality and their generic computation. *Social Networks*, 30(2):136–145, May 2008.

[17] Cameron B. Browne, Edward Powley, Daniel Whitehouse, Simon M. Lucas, Peter I. Cowling, Philipp Rohlfshagen, Stephen Tavener, Diego Perez, Spyridon Samothrakis, and Simon Colton. A Survey of Monte Carlo Tree Search Methods. *IEEE Transactions on Computational Intelligence and AI in Games*, 4(1):1–43, March 2012. Conference Name: IEEE Transactions on Computational Intelligence and AI in Games.

[18] Weiran Cao, Jian Li, Hongzheng Chen, and Jiangeng Xue. Transparent electrodes for organic optoelectronic devices: a review. *Journal of Photonics for Energy*, 4(1):040990, October 2014.

[19] Woo Hyun Chae, Thomas Sannicolo, and Jeffrey C. Grossman. Double-Sided Graphene Oxide Encapsulated Silver Nanowire Transparent Electrode with Improved Chemical and Electrical Stability. *ACS Applied Materials & Interfaces*, 12(15):17909–17920, April 2020.

[20] Nicolas Charvin, Joao Resende, Dorina T. Papanastasiou, David Muñoz-Rojas, Carmen Jiménez, Ali Nourdine, Daniel Bellet, and Lionel Flandin. Dynamic degradation of metallic nanowire networks under electrical stress: a comparison between experiments and simulations. *Nanoscale Advances*, 3(3):675–681, 2021. Publisher: Royal Society of Chemistry.

[21] Zhangxian Chen, Wanchao Li, Ran Li, Yunfeng Zhang, Guoqin Xu, and Hansong Cheng. Fabrication of Highly Transparent and Conductive Indium–Tin Oxide Thin Films with a High Figure of Merit via Solution Processing. *Langmuir*, 29(45):13836–13842, November 2013. Publisher: American Chemical Society.

[22] Philip E. Ciddor. Refractive index of air: new equations for the visible and near infrared. *Applied Optics*, 35(9):1566, March 1996.

[23] Rémi Coulom. Efficient Selectivity and Backup Operators in Monte-Carlo Tree Search. In H. Jaap van den Herik, Paolo Ciancarini, and H. H. L. M. (Jeroen) Donkers, editors, *Computers and Games*, Lecture Notes in Computer Science, pages 72–83, Berlin, Heidelberg, 2007. Springer.

[24] Paolo Crucitti, Vito Latora, Massimo Marchiori, and Andrea Rapisarda. Error and attack tolerance of complex networks. *Physica A: Statistical Mechanics and its Applications*, 340(1):388–394, September 2004.

[25] Marie Delacre, Daniël Lakens, and Christophe Leys. Why Psychologists Should by Default Use Welch's t-test Instead of Student's t-test. 30(1):92, April 2017. Number: 1 Publisher: Ubiquity Press.

[26] Marie Delacre, Daniël Lakens, and Christophe Leys. Correction: Why Psychologists Should by Default Use Welch's t-test Instead of Student's t-test. 35(1):21, November 2022. Number: 1 Publisher: Ubiquity Press.

[27] M. Dirnberger, T. Kehl, and A. Neumann. NEFI: Network Extraction From Images. *Scientific Reports*, 5(1):15669, November 2015. Number: 1 Publisher: Nature Publishing Group.

[28] Jack Edmonds. Paths, Trees, and Flowers. *Canadian Journal of Mathematics*, 17:449–467, 1965.

[29] Jose Luis Elechiguerra, Leticia Larios-Lopez, Cui Liu, Domingo Garcia-Gutierrez, Alejandra Camacho-Bragado, and Miguel Jose Yacaman. Corrosion at the Nanoscale: The Case of Silver Nanowires and Nanoparticles. *Chemistry of Materials*, 17(24):6042–6052, November 2005.

[30] Andreas Elschner and Wilfried Lövenich. Solution-deposited PEDOT for transparent conductive applications. *MRS Bulletin*, 36(10):794–798, October 2011.

[31] P. Erdös and A. Rényi. *The Structure and Dynamics of Networks*. Princeton University Press, October 2011. Pages: 38-82 Publication Title: The Structure and Dynamics of Networks Section: The Structure and Dynamics of Networks.

[32] Martin Ester, Hans-Peter Kriegel, and Xiaowei Xu. A Density-Based Algorithm for Discovering Clusters in Large Spatial Databases with Noise.

[33] F. Fievet, J. P. Lagier, and M. Figlarz. Preparing Monodisperse Metal Powders in Micrometer and Submicrometer Sizes by the Polyol Process. *MRS Bulletin*, 14(12):29–34, December 1989. Publisher: Cambridge University Press.

[34] Linton C. Freeman. A Set of Measures of Centrality Based on Betweenness. *Sociometry*, 40(1):35, March 1977.

[35] Max Frei and Frank Einar Kruis. FibeR-CNN: Expanding Mask R-CNN to Improve Image-Based Fiber Analysis. *Powder Technology*, 377:974–991, January 2021. arXiv:2006.04552 [cs].

[36] Georg Frobenius. Ueber Matrizen aus nicht negativen Elementen. *Sitzungsberichte der Königlich Preussischen Akademie der Wissenschaften*, pages 457–477, May 1912.

[37] Zvi Galil. Efficient algorithms for finding maximum matching in graphs. *ACM Computing Surveys*, 18(1):23–38, March 1986.

[38] Sean Gillies, Casper van der Wel, Joris Van den Bossche, Mike W. Taves, Joshua Arnott, Brendan C. Ward, et al. Shapely, December 2022.

[39] Jeff T. Gostick, Zohaib A. Khan, Thomas G. Tranter, Matthew D. r Kok, Mehrez Agnaou, Mohammadamin Sadeghi, and Rhodri Jervis. PoreSpy: A Python Toolkit for Quantitative Analysis of Porous Media Images. *Journal of Open Source Software*, 4(37):1296, May 2019.

[40] Jonathan L. Gross, Jay Yellen, Ping Zhang, Jay Yellen, and Ping Zhang. *Handbook of Graph Theory*. Chapman and Hall/CRC, December 2013.

[41] Chuan Fei Guo and Zhifeng Ren. Flexible transparent conductors based on metal nanowire networks. *Materials Today*, 18(3):143–154, April 2015.

[42] M. P. Gupta, N. Kumar, and S. Kumar. Computational Study of Thermal Transport in Nanowire-Graphene Thin Films. *IEEE Transactions on Nanotechnology*, 17(4):829–836, July 2018.

[43] Man Prakash Gupta and Satish Kumar. Numerical study of electrical transport in co-percolative metal nanowire-graphene thin-films. *Journal of Applied Physics*, 120(17):175106, November 2016.

[44] Manuela Göbelt, Ralf Keding, Sebastian W. Schmitt, Björn Hoffmann, Sara Jäckle, Michael Latzel, Vuk V. Radmilović, Velimir R. Radmilović, Erdmann Spiecker, and Silke Christiansen. Encapsulation of silver nanowire networks by atomic layer deposition for indium-free transparent electrodes. *Nano Energy*, 16:196–206, September 2015.

[45] Aric A Hagberg, Daniel A Schult, and Pieter J Swart. Exploring Network Structure, Dynamics, and Function using NetworkX. In *Proceedings of the 7th Python in Science Conference*, pages 11–15, Pasadena, CA USA, 2008.

[46] Kaiming He, Georgia Gkioxari, Piotr Dollár, and Ross Girshick. Mask R-CNN. *IEEE Transactions on Pattern Analysis and Machine Intelligence*, 42(2):386–397, February 2020. Conference Name: IEEE Transactions on Pattern Analysis and Machine Intelligence.

[47] Linxiang He and Sie Chin Tjong. Nanostructured transparent conductive films: Fabrication, characterization and applications. *Materials Science and Engineering: R: Reports*, 109:1–101, November 2016.

[48] Xin He, A'lei Liu, Xuyang Hu, Mingxia Song, Feng Duan, Qiuming Lan, Jundong Xiao, Junyan Liu, Mei Zhang, Yeqing Chen, and Qingguang Zeng. Temperature-controlled transparent-film heater based on silver nanowire–PMMA composite film. *Nanotechnology*, 27(47):475709, October 2016. Publisher: IOP Publishing.

[49] David S. Hecht and Richard B. Kaner. Solution-processed transparent electrodes. *MRS Bulletin*, 36(10):749–755, October 2011.

[50] Jérôme Heitz, Yann Leroy, Luc Hébrard, and Christophe Lallement. Theoretical characterization of the topology of connected carbon nanotubes in random networks. *Nanotechnology*, 22(34):345703, July 2011. Publisher: IOP Publishing.

[51] Petter Holme, Beom Jun Kim, Chang No Yoon, and Seung Kee Han. Attack vulnerability of complex networks. *Physical Review E*, 65(5):056109, May 2002.

[52] Liangbing Hu, Han Sun Kim, Jung-Yong Lee, Peter Peumans, and Yi Cui. Scalable Coating and Properties of Transparent, Flexible, Silver Nanowire Electrodes. *ACS Nano*, 4(5):2955–2963, May 2010. Publisher: American Chemical Society.

[53] Swami Iyer, Timothy Killingback, Bala Sundaram, and Zhen Wang. Attack Robustness and Centrality of Complex Networks. *PLoS ONE*, 8(4):e59613, April 2013.

[54] Milind Jagota and Nelson Tansu. Conductivity of Nanowire Arrays under Random and Ordered Orientation Configurations. *Scientific Reports*, 5:10219, May 2015.

[55] Shulin Ji, Weiwei He, Ke Wang, Yunxia Ran, and Changhui Ye. Thermal Response of Transparent Silver Nanowire/PEDOT:PSS Film Heaters. *Small*, 10(23):4951–4960, 2014.

[56] Richard W. Johnson, Adam Hultqvist, and Stacey F. Bent. A brief review of atomic layer deposition: from fundamentals to applications. *MATERIALS TODAY*, 17(5):236–246, June 2014. Num Pages: 11 Place: Oxford Publisher: Elsevier Sci Ltd Web of Science ID: WOS:000338412300017.

[57] Kelsey Jordahl, Joris Van Den Bossche, Martin Fleischmann, Jacob Wasserman, James McBride, Jeffrey Gerard, Jeff Tratner, Matthew Perry, Adrian Garcia Badaracco, Carson Farmer, Geir Arne Hjelle, Alan D. Snow, Micah Cochran, Sean Gillies, Lucas Culbertson, Matt Bartos, Nick Eubank, Maxalbert, Aleksey Bilogur, Sergio Rey, Christopher Ren, Dani Arribas-Bel, Leah Wasser, Levi John Wolf, Martin Journois, Joshua Wilson, Adam Greenhall, Chris Holdgraf, Filipe, and François Leblanc. geopandas/geopandas: v0.8.1, July 2020.

[58] Hyungseok Kang, Yeontae Kim, Siuk Cheon, Gi-Ra Yi, and Jeong Ho Cho. Halide Welding for Silver Nanowire Network Electrode. *ACS Applied Materials & Interfaces*, 9(36):30779–30785, September 2017. Publisher: American Chemical Society.

[59] Eric R Keiter, Thomas V Russo, Richard L Schiek, Heidi K Thornquist, Ting Mei, Jason C Verley, Peter E Sholander, and Karthik V Aadithya. Xyce Parallel Electronic Simulator Users' Guide, Version 6.1, 2019.

[60] G. Khanarian, J. Joo, X.-Q. Liu, P. Eastman, D. Werner, K. O'Connell, and P. Trefonas. The optical and electrical properties of silver nanowire mesh films. *Journal of Applied Physics*, 114(2):024302, July 2013. Publisher: American Institute of Physics.

[61] Farhan Nur Kholid, Hui Huang, Yongqi Zhang, and Hong Jin Fan. Multiple electrical breakdowns and electrical annealing using high current approximating breakdown current of silver nanowire network. *Nanotechnology*, 27(2):025703, December 2015.

[62] Areum Kim, Yulim Won, Kyoohee Woo, Chul-Hong Kim, and Jooho Moon. Highly Transparent Low Resistance ZnO/Ag Nanowire/ZnO Composite Electrode for Thin Film Solar Cells. *ACS Nano*, 7(2):1081–1091, February 2013. Publisher: American Chemical Society.

[63] H. Kim, C. M. Gilmore, A. Piqué, J. S. Horwitz, H. Mattoussi, H. Murata, Z. H. Kafafi, and D. B. Chrisey. Electrical, optical, and structural properties of indium-tin-oxide thin films for organic light-emitting devices. *Journal of Applied Physics*, 86(11):6451–6461, November 1999. Publisher: American Institute of Physics.

[64] TaeYoung Kim, Yeon Won Kim, Ho Seok Lee, Hyeongkeun Kim, Woo Seok Yang, and Kwang S. Suh. Uniformly Interconnected Silver-Nanowire Networks for Transparent Film Heaters. *Advanced Functional Materials*, 23(10):1250–1255, 2013.

[65] Casimir Kuratowski. Sur le probleme des courbes gauches en Topologie. *Fund. Math.*, 15:217–283, 1930.

[66] Yue Chau Garen Kwan, Quang Luan Le, and Cheng Hon Alfred Huan. Time to failure modeling of silver nanowire transparent conducting electrodes and effects

of a reduced graphene oxide over layer. *Solar Energy Materials and Solar Cells*, 144:102–108, January 2016.

[67] M. Lagrange, T. Sannicolo, D. Muñoz-Rojas, B. Guillo Lohan, A. Khan, M. Anikin, C. Jiménez, F. Bruckert, Y. Bréchet, and D. Bellet. Understanding the mechanisms leading to failure in metallic nanowire-based transparent heaters, and solution for stability enhancement. *Nanotechnology*, 28(5):055709, December 2016.

[68] Edmund Landau. Publications of Edmund Landau. In I. J. Schoenberg and Paul Turán, editors, *Number Theory and Analysis: A Collection of Papers in Honor of Edmund Landau (1877–1938)*, pages 335–355. Springer US, Boston, MA, 1969.

[69] D. P. Langley, M. Lagrange, G. Giusti, C. Jiménez, Y. Bréchet, N. D. Nguyen, and D. Bellet. Metallic nanowire networks: effects of thermal annealing on electrical resistance. *Nanoscale*, 6(22):13535–13543, 2014.

[70] Daniel Langley. *Silver nanowire networks: effects of percolation and thermal annealing on physical properties*. PhD thesis, University of Grenoble, 2014.

[71] Daniel P. Langley, Mélanie Lagrange, Ngoc Duy Nguyen, and Daniel Bellet. Percolation in networks of 1-dimensional objects: comparison between Monte Carlo simulations and experimental observations. *Nanoscale Horizons*, 3(5):545–550, August 2018. Publisher: The Royal Society of Chemistry.

[72] Jin Hwan Lee, Phillip Lee, Dongjin Lee, Seung Seob Lee, and Seung Hwan Ko. Large-Scale Synthesis and Characterization of Very Long Silver Nanowires via Successive Multistep Growth. *Crystal Growth & Design*, 12(11):5598–5605, November 2012. Publisher: American Chemical Society.

[73] Jinhwan Lee, Phillip Lee, Hyungman Lee, Dongjin Lee, Seung Seob Lee, and Seung Hwan Ko. Very long Ag nanowire synthesis and its application in a highly transparent, conductive and flexible metal electrode touch panel. *Nanoscale*, 4(20):6408–6414, September 2012. Publisher: The Royal Society of Chemistry.

[74] Hongpeng Li, Xiran Li, Jiajie Liang, and Yongsheng Chen. Micro-Supercapacitors: Hydrous RuO2-Decorated MXene Coordinating with Silver Nanowire Inks Enabling Fully Printed Micro-Supercapacitors with Extraordinary Volumetric Performance (Adv. Energy Mater. 15/2019). *Advanced Energy Materials*, 9(15):1970050, 2019.

[75] Jiantong Li and Shi-Li Zhang. Conductivity exponents in stick percolation. *Physical Review E*, 81(2):021120, February 2010. Publisher: American Physical Society.

[76] Yuan Li, Kaoru Tsuchiya, Hironori Tohmyoh, and Masumi Saka. Numerical analysis of the electrical failure of a metallic nanowire mesh due to Joule heating. *Nanoscale Research Letters*, 8(1):370, December 2013.

[77] Jiajie Liang, Lu Li, Kwing Tong, Zhi Ren, Wei Hu, Xiaofan Niu, Yongsheng Chen, and Qibing Pei. Silver Nanowire Percolation Network Soldered with Graphene Oxide at Room Temperature and Its Application for Fully Stretchable Polymer Light-Emitting Diodes. *ACS Nano*, 8(2):1590–1600, February 2014. Publisher: American Chemical Society.

[78] Tsung-Yi Lin, Michael Maire, Serge Belongie, Lubomir Bourdev, Ross Girshick, James Hays, Pietro Perona, Deva Ramanan, C. Lawrence Zitnick, and Piotr Dollár. Microsoft COCO: Common Objects in Context, February 2015. arXiv:1405.0312 [cs].

[79] Philipp Maisch, Kai Cheong Tam, Luca Lucera, Hans-Joachim Egelhaaf, Horst Scheiber, Eugen Maier, and Christoph J. Brabec. Inkjet printed silver nanowire percolation networks as electrodes for highly efficient semitransparent organic solar cells. *Organic Electronics*, 38:139–143, November 2016.

[80] Kerry Maize, Suprem R. Das, Sajia Sadeque, Amr M. S. Mohammed, Ali Shakouri, David B. Janes, and Muhammad A. Alam. Super-Joule heating in graphene and silver nanowire network. *Applied Physics Letters*, 106(14):143104, April 2015.

[81] Hugh G. Manning, Claudia Gomes da Rocha, Colin O' Callaghan, Mauro S. Ferreira, and John J. Boland. The Electro-Optical Performance of Silver Nanowire Networks. *Scientific Reports*, 9(1):11550, August 2019. Bandiera_abtest: a Cc_license_type: cc_by Cg_type: Nature Research Journals Number: 1 Primary_atype: Research Publisher: Nature Publishing Group Subject_term: Computational methods;Electronic devices;Nanowires Subject_term_id: computational-methods;electronic-devices;nanowires.

[82] Hugh G. Manning, Fabio Niosi, Claudia Gomes da Rocha, Allen T. Bellew, Colin O'Callaghan, Subhajit Biswas, Patrick F. Flowers, Benjamin J. Wiley, Justin D. Holmes, Mauro S. Ferreira, and John J. Boland. Emergence of winner-takes-all connectivity paths in random nanowire networks. *Nature Communications*, 9(1):3219, August 2018. Number: 1 Publisher: Nature Publishing Group.

[83] Cecilia Mattevi, Hokwon Kim, and Manish Chhowalla. A review of chemical vapour deposition of graphene on copper. *Journal of Materials Chemistry*, 21(10):3324–3334, February 2011. Publisher: The Royal Society of Chemistry.

[84] Rose M. Mutiso, Michelle C. Sherrott, Aaron R. Rathmell, Benjamin J. Wiley, and Karen I. Winey. Integrating Simulations and Experiments To Predict Sheet Resistance and Optical Transmittance in Nanowire Films for Transparent Conductors. *ACS Nano*, 7(9):7654–7663, September 2013.

[85] Yong-Jin Noh, Seok-Soon Kim, Tae-Wook Kim, and Seok-In Na. Cost-effective ITO-free organic solar cells with silver nanowire–PEDOT:PSS composite electrodes via a one-step spray deposition method. *Solar Energy Materials and Solar Cells*, 120:226–230, January 2014.

[86] Dorina T. Papanastasiou, Amélie Schultheiss, David Muñoz-Rojas, Caroline Celle, Alexandre Carella, Jean-Pierre Simonato, and Daniel Bellet. Transparent Heaters: A Review. *Advanced Functional Materials*, 30(21):1910225, 2020.

[87] Jatin J. Patil, Woo Hyun Chae, Adam Trebach, Ki-Jana Carter, Eric Lee, Thomas Sannicolo, and Jeffrey C. Grossman. Failing Forward: Stability of Transparent Electrodes Based on Metal Nanowire Networks. *Advanced Materials*, page 2004356, 2020.

[88] Jatin J. Patil, Zhengmao Lu, Michael J. Zachman, Ningxin Chen, Kimberly S. Reeves, Asmita Jana, Griselda Revia, Brandon MacDonald, Brent D. Keller, Edgar Lara-Curzio, Jeffrey C. Grossman, and Nicola Ferralis. Chemical and Physical Drivers for Improvement in Permeance and Stability of Linker-Free Graphene Oxide Membranes. *Nano Letters*, 23(14):6414–6423, July 2023. Publisher: American Chemical Society.

[89] H R Patils and H B Huntington. ELECTROMIGRATION AND ASSOCIATED VOID FORMATION IN SILVER"?

[90] Fabian Pedregosa, Gael Varoquaux, Alexandre Gramfort, Vincent Michel, Bertrand Thirion, Olivier Grisel, Mathieu Blondel, Peter Prettenhofer, Ron Weiss, Vincent Dubourg, Jake Vanderplas, Alexandre Passos, and David Cournapeau. Scikit-learn: Machine Learning in Python. *Journal of Machine Learning Research*, 12:2825–2830, 2011.

[91] Oskar Perron. Zur Theorie der Matrices. *Mathematische Annalen*, 64(2):248–263, June 1907.

[92] G. E. Pike and C. H. Seager. Percolation and conductivity: A computer study. I. *Physical Review B*, 10(4):1421–1434, August 1974.

[93] Mahendra Piraveenan, Mikhail Prokopenko, and Liaquat Hossain. Percolation Centrality: Quantifying Graph-Theoretic Impact of Nodes during Percolation in Networks. *PLOS ONE*, 8(1):e53095, January 2013. Publisher: Public Library of Science.

[94] PyTorch. vision/references/detection/train.py at main · pytorch/vision, October 2023.

[95] Feng Qin, Zhiyang Yan, Jinfeng Fan, Jinliang Cai, Xingzhong Zhu, and Xiaogang Zhang. Highly Uniform and Stable Transparent Electromagnetic Interference Shielding Film Based on Silver Nanowire–PEDOT:PSS Composite for High Power Microwave Shielding. *Macromolecular Materials and Engineering*, 306(2):2000607, 2021.

[96] Michael Quinten. *Optical Properties of Nanoparticle Systems: Mie and beyond*. Wiley-VCH Verlag GmbH & Co. KGaA, Weinheim, Germany, January 2011.

[97] Johann Radon. On the determination of functions from their integral values along certain manifolds. *IEEE Transactions on Medical Imaging*, 5(4):170–176, December 1986. Conference Name: IEEE Transactions on Medical Imaging.

[98] Bishakha Ray, Saurabh Parmar, and Suwarna Datar. Advanced Materials for Electromagnetic Shielding: Fundamentals, Properties, and Applications. In *Advanced Materials for Electromagnetic Shielding: Fundamentals, Properties, and Applications*, pages 167–175. John Wiley & Sons, November 2018. Google-Books-ID: Rlt0DwAAQBAJ.

[99] Justin Romberg. Image Projections and the Radon Transform.

[100] Olaf Ronneberger, Philipp Fischer, and Thomas Brox. U-Net: Convolutional Networks for Biomedical Image Segmentation, May 2015. arXiv:1505.04597 [cs].

[101] Thomas Sannicolo, Woo Hyun Chae, Jeremiah Mwaura, Vladimir Bulovic, and Jeffrey Grossman. Silver Nanowire Back Electrode Stabilized with Graphene Oxide Encapsulation for Inverted Semitransparent Organic Solar Cells with Longer Lifetime. *ACS Applied Energy Materials*, 4, January 2021.

[102] Thomas Sannicolo, Nicolas Charvin, Lionel Flandin, Silas Kraus, Dorina T. Papanastasiou, Caroline Celle, Jean-Pierre Simonato, David Muñoz-Rojas, Carmen Jiménez, and Daniel Bellet. Electrical Mapping of Silver Nanowire Networks: A Versatile Tool for Imaging Network Homogeneity and Degradation Dynamics during Failure. *ACS Nano*, 12(5):4648–4659, May 2018.

[103] Thomas Schirmer, Wilfried Ließmann, Chandra Macauley, and Peter Felfer. Indium and Antimony Distribution in a Sphalerite from the "Burgstaetter Gangzug" of the Upper Harz Mountains Pb-Zn Mineralization. *Minerals*, 10(9):791, September 2020. Number: 9 Publisher: Multidisciplinary Digital Publishing Institute.

[104] Erich Schubert, Jörg Sander, Martin Ester, Hans Peter Kriegel, and Xiaowei Xu. DBSCAN Revisited, Revisited: Why and How You Should (Still) Use DBSCAN. *ACM Transactions on Database Systems*, 42(3):1–21, August 2017.

[105] Baekhoon Seong, Ilkyeong Chae, Hyungdong Lee, Vu Dat Nguyen, and Doyoung Byun. Spontaneous self-welding of silver nanowire networks. *Physical Chemistry Chemical Physics*, 17(12):7629–7633, March 2015. Publisher: The Royal Society of Chemistry.

[106] Sergio B. Sepulveda-Mora and Sylvain G. Cloutier. Figures of Merit for High-Performance Transparent Electrodes Using Dip-Coated Silver Nanowire Networks. *Journal of Nanomaterials*, 2012:e286104, September 2012. Publisher: Hindawi.

[107] M. Sezgin, Bu Sankur, and Bebek I. Survey Over Image Thresholding Techniques. *J Electronic Imaging*, 13, July 2004.

[108] David Silver, Thomas Hubert, Julian Schrittwieser, Ioannis Antonoglou, Matthew Lai, Arthur Guez, Marc Lanctot, Laurent Sifre, Dharshan Kumaran, Thore Graepel, Timothy Lillicrap, Karen Simonyan, and Demis Hassabis. Mastering Chess and Shogi by Self-Play with a General Reinforcement Learning Algorithm. *arXiv.org*, December 2017.

[109] Myungkwan Song, Dae Sung You, Kyounga Lim, Sujin Park, Sunghoon Jung, Chang Su Kim, Dong-Ho Kim, Do-Geun Kim, Jongk-Kuk Kim, Juyun Park, Yong-Cheol Kang, Jinhee Heo, Sung-Ho Jin, Jong Hyun Park, and Jae-Wook Kang. Organic Solar Cells: Highly Efficient and Bendable Organic Solar Cells with Solution-Processed Silver Nanowire Electrodes (Adv. Funct. Mater. 34/2013). *Advanced Functional Materials*, 23(34):4272–4272, 2013.

[110] Sophie Sorel, Philip E Lyons, Sukanta De, Janet C Dickerson, and Jonathan N Coleman. The dependence of the optoelectrical properties of silver nanowire networks on nanowire length and diameter. *Nanotechnology*, 23(18):185201, May 2012.

[111] Yugang Sun, Brian Mayers, Thurston Herricks, and Younan Xia. Polyol Synthesis of Uniform Silver Nanowires: A Plausible Growth Mechanism and the Supporting Evidence. *Nano Letters*, 3(7):955–960, July 2003.

[112] United States Geological Survey. Mineral Commodity Summaries 2000. 2000.

[113] United States Geological Survey. Mineral Commodity Summaries 2022. 2022.

[114] U.S. Geological Survey. Mineral Commodity Summaries. Technical report, United States Geological Survey, 2019.

[115] G. N. Tiwari, Arvind Tiwari, and Shyam. Solar Radiation. In *Handbook of Solar Energy*, pages 1–49. Springer Singapore, Singapore, 2016. Series Title: Energy Systems in Electrical Engineering.

[116] Adam Trebach, Evan Toth, Woo Hyun Chae, Jatin Patil, Ki-Jana Carter, Thomas Sannicolo, and Jeffrey C. Grossman. De-densifying metallic nanowire networks using betweenness centrality. *Computational Materials Science*, 214:111683, November 2022.

[117] Kaoru Tsuchiya, Yuan Li, and Masumi Saka. Consistent melting behavior induced by Joule heating between Ag microwire and nanowire meshes. *Nanoscale Research Letters*, 9(1):239, 2014.

[118] Jago Txintxurreta, Eva G-Berasategui, Rocío Ortiz, Oihane Hernández, Lucía Mendizábal, and Javier Barriga. Indium Tin Oxide Thin Film Deposition by Magnetron Sputtering at Room Temperature for the Manufacturing of Efficient Transparent Heaters. *Coatings (2079-6412)*, 11(1):92, January 2021.

[119] Simon Vigonski, Ville Jansson, Sergei Vlassov, Boris Polyakov, Ekaterina Baibuz, Sven Oras, Alvo Aabloo, Flyura Djurabekova, and Vahur Zadin. Au nanowire junction breakup through surface atom diffusion. *Nanotechnology*, 29(1):015704, January 2018.

[120] Morkiaki Wakaki, Takehisa Shibuya, and Keiei Kudo. Physical Properties and Data of Optical Materials. In *Physical Properties and Data of Optical Materials*, page 419. CRC Press, Boca Raton, 2007.

[121] Stéfan van der Walt, Johannes L. Schönberger, Juan Nunez-Iglesias, François Boulogne, Joshua D. Warner, Neil Yager, Emmanuelle Gouillart, and Tony Yu. scikit-image: image processing in Python. *PeerJ*, 2:e453, June 2014. Publisher: PeerJ Inc.

[122] Jinlong Wang, Muhammad Hassan, Jian-Wei Liu, and Shu-Hong Yu. Nanowire Assemblies for Flexible Electronic Devices: Recent Advances and Perspectives. *Advanced Materials*, 30, October 2018.

[123] Liming Wang, Jianbo Shi, Gang Song, and I-fan Shen. Object Detection Combining Recognition and Segmentation. In Yasushi Yagi, Sing Bing Kang, In So Kweon, and Hongbin Zha, editors, *Computer Vision – ACCV 2007*, volume 4843, pages 189–199. Springer Berlin Heidelberg, Berlin, Heidelberg, 2007. Series Title: Lecture Notes in Computer Science.

[124] Shiyu Wei, Zhe Li, Krishnan Murugappan, Ziyuan Li, Fanlu Zhang, Aswani Gopakumar Saraswathyvilasam, Mykhaylo Lysevych, Hark Hoe Tan, Chennupati Jagadish, Antonio Tricoli, and Lan Fu. A Self-Powered Portable Nanowire Array Gas Sensor for Dynamic NO2 Monitoring at Room Temperature. *Advanced Materials*, 35(12):2207199, 2023. _eprint: https://onlinelibrary.wiley.com/doi/pdf/10.1002/adma.202207199.

[125] B. L. Welch. The Generalization of 'Student's' Problem when Several Different Population Variances are Involved. *Biometrika*, 34(1/2):28–35, 1947. Publisher: [Oxford University Press, Biometrika Trust].

[126] Sadie I. White, Rose M. Mutiso, Patrick M. Vora, David Jahnke, Sam Hsu, James M. Kikkawa, Ju Li, John E. Fischer, and Karen I. Winey. Electrical Percolation Behavior in Silver Nanowire–Polystyrene Composites: Simulation and Experiment. *Advanced Functional Materials*, 20(16):2709–2716, August 2010.

[127] Anky Fitrian Wibowo, Joo Won Han, Jung Ha Kim, Ajeng Prameswati, Siti Aisyah Nurmaulia Entifar, Jihyun Park, Jonghee Lee, Soyeon Kim, Dong Chan Lim, Myoung-Woon Moon, Min-Seok Kim, and Yong Hyun Kim. Highly stretchable and robust transparent conductive polymer composites for multifunctional healthcare monitoring. *Science and Technology of Advanced Materials*, 23(1):332–340, December 2022. Publisher: Taylor & Francis _eprint: https://doi.org/10.1080/14686996.2022.2070864.

[128] Xiao Xiong, Chang-Ling Zou, Xi-Feng Ren, Ai-Ping Liu, Yan-Xia Ye, Fang-Wen Sun, and Guang-Can Guo. Silver nanowires for photonics applications. *Laser & Photonics Reviews*, 7(6):901–919, 2013.

[129] Shengrong Ye, Aaron R. Rathmell, Ian E. Stewart, Yoon-Cheol Ha, Adria R. Wilson, Zuofeng Chen, and Benjamin J. Wiley. A rapid synthesis of high aspect ratio copper nanowires for high-performance transparent conducting films. *Chemical Communications*, 50(20):2562–2564, February 2014. Publisher: The Royal Society of Chemistry.

[130] Kan Zhan, Rui Su, Sihang Bai, Zhenhua Yu, Nian Cheng, Changlei Wang, Sheng Xu, Wei Liu, Shishang Guo, and Xing-Zhong Zhao. One-pot stirring-free synthesis of silver nanowires with tunable lengths and diameters via a Fe3+ & Cl- co-mediated polyol method and their application as transparent conductive films. *Nanoscale*, 8(42):18121–18133, October 2016. Publisher: The Royal Society of Chemistry.

[131] Kui Zhang, Jia Li, Yunsheng Fang, Beibei Luo, Yanli Zhang, Yanqiu Li, Jun Zhou, and Bin Hu. Unraveling the solvent induced welding of silver nanowires for high performance flexible transparent electrodes. *Nanoscale*, 10(27):12981–12990, July 2018. Publisher: The Royal Society of Chemistry.

[132] Jiong Zhao, Hongyu Sun, Sheng Dai, Yan Wang, and Jing Zhu. Electrical Breakdown of Nanowires. *Nano Letters*, 11(11):4647–4651, November 2011.

[133] Zhaozhao Zhu, Trent Mankowski, Kaushik Balakrishnan, Ali Sehpar Shikoh, Farid Touati, Mohieddine A. Benammar, Masud Mansuripur, and Charles M. Falco. Hybrid transparent conductive electrodes with copper nanowires embedded in a zinc oxide matrix and protected by reduced graphene oxide platelets. *Journal of Applied Physics*, 119(8):085303, February 2016.